

**Permanent Prostate Brachytherapy Dosimetry:
Critical Assessments and Advancements**

By

Derek Man Chun Liu

A thesis submitted in partial fulfillment of the requirements for the degree of

Doctor of Philosophy

in

Medical Physics

Department of Oncology

University of Alberta

© Derek Man Chun Liu, 2014

Abstract

The dissertation explores some of the limitations and assumptions in the current approach to permanent prostate brachytherapy (PPB) dosimetry. Where possible, novel insights and practical improvements are proposed, which aim to enhance the accuracy of radiation dose delivery during treatment. The thesis assesses prostate delineation accuracy during treatment planning, seeks to improve dose calculation by accounting for edema, and investigates previously unstudied effects due to probe-induced prostate deformation.

Prostate delineation during treatment planning directly impacts dose delivery accuracy and conformity. Prostate contouring, commonly performed on transrectal ultrasound (TRUS) images, is compared to that on magnetic resonance (MR) images, which provide superior soft tissue contrast. Patients are imaged on both modalities and the delineated prostates are compared in terms of volume, shape, and observer contouring variability. The prostate volume and inter- and intra- observer variability, quantified by the volume and overlap, were similar between the imaging modalities. MR offered the potential for improved delineation at the prostate base and apex, regions known to be difficult to contour on ultrasound. However, more delineation experience on MR is likely necessary before the benefits can be realized.

Systematic prostate volume differences attributable to the choice of reconstruction algorithm could be mistaken for contouring bias between the imaging modalities. The accuracy of the commonly used planimetry and frustum algorithms is evaluated in the context of TRUS image acquisition, using simulated contours representing geometrical

objects with known volumes. For TRUS imaging characterized by a large inter-slice gap and non-random positioning of the first imaged slice, the planimetry algorithm slightly overestimated the prostate volume (by roughly 4 %) while the frustum algorithm underestimated the volume (by 3 %).

Prostatic edema gives rise to a dynamic, correlated movement of the prostate and implanted seeds, resulting in deviations in the doses calculated at a single time point. The edema-related effects on planning and post-implant dosimetry are investigated using a clinically-informed edema model previously developed. For patient-average edema parameters, incorporating edema resulted in roughly 2 % lower dose and a small (3 Gy) reduction in prostate D_{90} . The dosimetric differences were similar between patients and between planning and post-implant distributions. The effect of prostatic edema was therefore largely determined by the patient-specific edema response.

The general solution to the problem of dose calculation incorporating edema is computationally intensive. A fast calculation method was previously reported based on dose kernel convolution using the Fourier transform. However, limitations on the seed placement resulted in unacceptable dose calculation errors. A novel method is proposed using Fourier-compatible kernel interpolation, expanding upon the original method and enabling unrestricted seed placement. The method substantially improved the clinically relevant dose accuracy with negligible additional computation cost.

Prostate deformation due to the TRUS probe is generally not accounted for during treatment. Although the deformation is small, the expected impact on dosimetry has not been investigated and is usually assumed to be negligible. A novel investigation is performed to characterize and quantify the probe-induced seed movement and its impact on dosimetry. Implant movement patterns are observed, providing insight into modeling the underlying prostate deformation. Although the observed movements were generally small (mostly < 2 mm), the overall contraction of the implant distribution resulted in a non-negligible prostate D_{90} average increase of 4 Gy (range 0 to 8 Gy). The movement (up to 5 mm) of extra-prostatic seeds in the lateral peripheral regions had potential consequence for local target coverage. The study demonstrated that probe-induced deformation of the prostate is not always negligible as commonly assumed.

In summary, the dissertation assesses the current approach to PPB dosimetry and introduces improvements pertaining to target delineation, volume calculation, dose calculation, and implant delivery. With further research and development these refinements could be implemented in the clinic, where they have the potential to improve patient treatment outcomes.

Preface

A version of chapter 3 has been published:

D. Liu, N. Usmani, S. Ghosh, W. Kamal, J. Pedersen, N. Pervez, D. Yee, B. Danielson, A. Murtha, J. Amanie, R.S. Sloboda, "Comparison of prostate volume, shape, and contouring variability determined from preimplant magnetic resonance and transrectal ultrasound images." *Brachytherapy* 2012; 11: 284-291

Initial study design was by Dr. N. Usmani and Dr. R. Sloboda. Data collection was performed by Dr. N. Usmani, Dr. J. Pedersen, Dr. N. Pervez, Dr. D. Yee, Dr. B. Danielson, Dr. A. Murtha, Dr. J. Amanie, and W. Kamal. I was responsible for the design of the analysis, generation and analysis of the results, and composition of the manuscript. The statistical analysis was performed in collaboration with Dr. S. Ghosh. The research received ethics approval from Alberta Health Services (IGAR-2005-I11) titled 'Improving Assessment (and ultimately outcomes) of Permanent Prostate Implant Therapy'.

A version of chapter 4 has been published:

D. Liu, N. Usmani, R.S. Sloboda, "Transrectal Ultrasound Based Prostate Volume Determination: Is the Frustum Algorithm More Accurate than Planimetry?" *Med Phys* 2013; 40: 031705-1

I was the primary investigator with supervision from Dr. N. Usmani and Dr. R. Sloboda.

A version of chapter 5 has been presented at the European Society for Radiotherapy and Oncology 2012 annual meeting:

D. Liu, T. Monajemi, R. Sloboda, "Incorporating Edema in I-125 Prostate Seed Implant Dosimetry using a Clinically-Informed Edema Model" *Radiother Oncol* 2012; 103: S91

I was the primary investigator with supervision from Dr. R. Sloboda. The edema model used in the study was based on a previous publication by Dr. T. Monajemi.

A version of chapter 6 has been published:

D. Liu, R.S. Sloboda, "Fast dose kernel interpolation using Fourier transform with application to permanent prostate brachytherapy dosimetry" *Med Phys* 2014; 41: 051701

I was the primary investigator with supervision from Dr. R. Sloboda.

The study presented in chapter 7 is under consideration for publication:

D. Liu, T Meyer, N Usmani, I Kay, S Husain, S Angyalfi, R Sloboda “Implanted Brachytherapy Seed Movement due to Transrectal Ultrasound Probe-Induced Prostate Deformation” Med Phys

The study was based on a separate but related research work by Dr. I. Kay, Dr. T. Meyer, Dr. S Husain, and Dr. S Angyalfi at the Tom Baker Cancer Centre, Calgary. I was responsible for the design of the analysis, generation and analysis of the results, and composition of the manuscript with supervision from Dr. R. Sloboda. Dr. N. Usmani assisted in data collection. The research received ethics approval from the University of Calgary (Ethics ID: E-20210) titled ‘Organ deformation and seed migration during low dose rate brachytherapy for early stage cancer of the prostate’. The approval was subsequently modified to include D. Liu, Dr. R. Sloboda, and Dr. N. Usmani from the Cross Cancer Institute, Edmonton.

*To my loving fiancée Kathleen,
to whom I will say 'I do' very soon.*

*And to my parents Eric and Ellen,
to whom I will always be indebted to.*

Acknowledgments

I would like to first acknowledge my better half, Kathleen, for the loving encouragement and selfless support over the past six years. The time spent has been the happiest in my life and, looking back, I believe I have become a better person because of her. Equally important are my parents Eric and Ellen who, although they live far away, continue to support me in whatever way they can, as if they are here with me. I can never thank them enough and I hope I can make them proud.

I would like to thank Dr. Ron Sloboda and Dr. Nawaid Usmani for their invaluable mentoring during my doctorate studies. In particular, both of them encouraged me to learn a comprehensive view of permanent prostate brachytherapy. I appreciate their open door policy and their willingness to take time out of their busy schedule. I would also like to acknowledge Dr. Gino Fallone for his career guidance and his tireless effort in securing funding, the additional members of my supervisory committee (Dr. Satyapal Rathee, Dr. Marc Mackenzie) for their expert advice and contribution to the dissertation, and additional members of the examination committee (Dr. Sharon Morsink, Dr. Ingrid Spadinger) for their efforts in ensuring the dissertation is of the highest quality possible.

I would like to thank all the staff and students at the Cross Cancer Institute for the positive experience over the years. I would like to acknowledge in particular: Colin Fields and Heather Warkentin for their professional and personal advice; Cathy Walsh, Jen Freund, Debbi Howorko, and Jocelyn Martin who went above and beyond to help me navigate the rules and regulations of Alberta Health Services and the University of Alberta; Dr. Stephen Steciw, Dr. Don Robinson, Dr. Rufus Scrimger, Dr. Amira Shakam, Dr. Duc Le, and Dr. Ian Kay and Dr. Tyler Meyer from the Tom Baker Cancer Centre all of whom I had the pleasure of collaborating with; Eugene Yip, Andrei Ghila, Dan Michael Santos, and Dr. Amr Heikal for their contributions to the wide ranging discussions in the office.

To this day, I continue to draw inspiration from Dr. Ervin Podgorsak whose feedback and advice I will never forget. Sheila Lindsey taught me the meaning of pain and how to push through it. This I wish I could forget. Finally, although we are separated by distance, I will always remember my good friends Stephen, David, Patrick, and Jai.

Table of Contents

Chapter 1 Introduction	1
1.1 Prostate Cancer	1
1.1.1 Overview	1
1.1.2 Screening and diagnosis.....	1
1.1.3 Cancer stages and risk categories	2
1.1.4 Treatment options	4
1.1.5 Treatment outcome endpoints.....	6
1.2 Permanent Prostate Brachytherapy.....	7
1.2.1 Overview.....	7
1.2.2 Patient eligibility	7
1.2.3 Treatment procedure	9
1.2.4 Treatment outcome	9
1.2.5 Treatment toxicity.....	10
1.3 Research Motivation	10
1.3.1 Importance of Dosimetry.....	10
1.3.2 Overview of dissertation	11
1.4 References.....	13
Chapter 2 Permanent Prostate Brachytherapy	19
2.1 Overview.....	19
2.2 Anatomy.....	19
2.3 Treatment Planning.....	21
2.3.1 Ultrasound volume study	21
2.3.2 Contouring and volume definitions	23
2.3.3 Radioactive isotopes	24
2.3.4 Planning criteria.....	24
2.3.5 Planning the implant	25
2.3.6 Intra-operative planning.....	28
2.3.7 Pubic arch interference	29

2.4	Implantation	30
2.4.1	Preparation and setup	30
2.4.2	Implantation	32
2.5	Post-Implant Evaluation.....	33
2.5.1	CT volume study.....	33
2.5.2	Evaluation of delivered dose.....	33
2.5.3	Timing of post-implant evaluation.....	34
2.5.4	Implant migration.....	35
2.5.5	Contouring uncertainty	35
2.5.6	Alternative imaging modalities.....	36
2.6	TG-43 Dose Calculation	36
2.6.1	Two-dimensional formalism.....	37
2.6.2	One-dimensional formalism.....	39
2.6.3	Dose-rate integral.....	40
2.6.4	Formalism limitations	40
2.7	Factors affecting brachytherapy dosimetry.....	41
2.7.1	Treatment planning	42
2.7.2	Implant delivery.....	42
2.7.3	Post-implant evaluation	44
2.8	References.....	47
Chapter 3	Comparison of pre-implant prostate contoured from magnetic resonance and transrectal ultrasound imaging.....	57
3.1	Introduction.....	57
3.2	Methods and materials	60
3.2.1	Patients and Imaging.....	60
3.2.2	Contouring	61
3.2.3	Volume and shape.....	61
3.2.4	Contour variability.....	62
3.2.5	Statistical analysis.....	63
3.3	Results.....	64

3.3.1 Volume and shape.....	64
3.3.2 Inter-observer contour variability	65
3.3.3 Intra-observer contour variability	66
3.4 Discussion	66
3.4.1 Volume and shape.....	66
3.4.2 TRUS-induced deformation.....	68
3.4.3 Contour variability.....	69
3.4.4 Implications of contour variability.....	71
3.5 Conclusion	72
3.6 References.....	72
 Chapter 4 Volume determination using frustum and planimetry algorithms in context of ultrasound imaging.....	 77
4.1 Introduction.....	77
4.2 Materials and methods	78
4.3 Results and discussion	80
4.3.1 Clinical prostate contours	80
4.3.2 Simulated object contours.....	81
4.3.3 Algorithm bias and volume estimation error	82
4.3.4 Literature comparison	84
4.4 Conclusion	84
4.5 References.....	84
 Chapter 5 Incorporating a clinically-informed anisotropic edema model in dose calculations	 87
5.1 Introduction.....	87
5.2 Materials and methods	89
5.2.1 Edema model	89
5.2.2 Dose calculation.....	89
5.2.3 Patient data and implementation.....	90
5.3 Results and discussion	91

5.4 Conclusion	92
5.5 References.....	92
Chapter 6 Fast dose kernel interpolation using Fourier transform with application to permanent prostate brachytherapy dosimetry incorporating prostate edema	
6.1 Introduction.....	94
6.2 Materials and methods	95
6.2.1 Snap-to-grid method	95
6.2.2 FT-interpolation method	96
6.2.3 FT-rotation method	98
6.2.4 Implementation	99
6.3 Results.....	99
6.3.1 Dose distribution accuracy.....	99
6.3.2 Kernel interpolation accuracy	100
6.3.3 Treatment dosimetry accuracy	101
6.3.4 FT-based rotation.....	102
6.3.5 Computation time.....	103
6.4 Discussion.....	103
6.4.1 Calculation accuracy	103
6.4.2 Computational efficiency.....	105
6.4.3 Implementation	106
6.4.4 Application to edema dose calculation	107
6.5 Conclusion	108
6.6 References.....	108
Chapter 7 Implanted brachytherapy seed movement due to transrectal ultrasound probe-induced prostate deformation.....	
7.1 Introduction.....	112
7.2 Materials and Methods.....	113
7.2.1 Implant technique.....	113
7.2.2 Fluoroscopy imaging and seed localization.....	113

7.2.3 Ultrasound imaging and prostate delineation	114
7.2.4 Seed movement model	115
7.2.5 Simulation of prostate contour upon probe removal.....	115
7.2.6 Dosimetric effects	116
7.3 Results.....	117
7.3.1 Seed movement.....	117
7.3.2 Dosimetric effects	121
7.4 Discussion.....	123
7.4.1 Image registration	123
7.4.2 Seed movement.....	124
7.4.3 Seed movement model.....	125
7.4.4 Dosimetric effects	126
7.4.5 Other uncertainties	128
7.5 Conclusion	128
7.6 References.....	129
Chapter 8 Summary and future directions	133
8.1 Summary.....	133
8.2 Future directions	137
8.3 Conclusion	139
8.4 References.....	139

List of Tables

Table 2.1: Planning dosimetry criteria for permanent prostate brachytherapy performed at the Cross Cancer Institute. Note that PTV = CTV.	25
Table 3.1: Baseline characteristics of patient population.	60
Table 3.2: Mean prostate volume and dimensions calculated from magnetic resonance (MR) and ultrasound (US) images.	64
Table 3.3: Mean prostate rectal indentation height and volume from magnetic resonance (MR) and ultrasound (US) images.	64
Table 3.4: Comparison of published inter- and intra-observer variability in terms of absolute and percentage prostate volume differences.	70
Table 5.1: Mean and range of dose metric values for dose calculations incorporating edema and their differences (static minus edema) from conventional calculations for static implants.	91
Table 6.1: Maximum dose-volume histogram metric errors over 10 cases.	102
Table 7.1: Regression values (mean and range) for the correlation tensor reflecting fractional expansion (diagonal) or shearing (off-diagonal) over 10 patients.	119
Table 7.2: Effect on dose-volume metrics (mean and range) of US probe removal, calculated using post-implant and preplan prostate contours.	122

List of Figures

Figure 1.1: Implantation during permanent or low dose-rate prostate brachytherapy. ¹⁴	4
Figure 1.2: External beam radiation therapy for prostate cancer. ¹⁶	5
Figure 2.1: The male pelvic region, showing the prostate and adjacent structures. ¹	19
Figure 2.2: Illustration of the internal prostate anatomy, divided into the peripheral zone (1), central zone (2), transition zone (3) and the anterior region. ¹	20
Figure 2.3: (left) Transrectal ultrasound probe with console system in background. ⁵ (right) Endocavity balloon filled with water solution. ⁶	21
Figure 2.4: (left) Manual stepper for probe positioning. (right) The imaging system ultrasound transducer and support assembly: probe attached to stepper mounted on a stabilizer. ⁶ Template grid located above the probe is used only during implantation.	22
Figure 2.5: Transverse and sagittal views of the prostate under transrectal ultrasound imaging.	22
Figure 2.6: Nuclear decay scheme for Iodine-125.....	24
Figure 2.7: Transverse ultrasound image from a treatment plan showing the prostate contour (red line), PTV (cyan line), 145 Gy isodose (thin red line), urethra (green line), rectum (blue line), pubic arch (purple line), virtual template grid (+), planned needle insertions (both open and solid circles), planned seed positions at that image slice (solid circles).....	26
Figure 2.8: Physical template grid corresponding to the virtual grid displayed on the ultrasound image used in treatment planning. ⁶	26
Figure 2.9: Pubic arch interference, determined and reconstructed from computed tomography imaging, as observed from the transperineal approach. The prostate (red)	

periphery is partially obscured by the left (yellow) and right (green) pubis bony structure.	29
Figure 2.10: A sample of the treatment plan sent to the vendor when ordering the implant, illustrating the needle loading.	30
Figure 2.11: Implantation procedure in PPB. ¹	31
Figure 2.12: (left) Needle insertion during implantation. (right) The needle as detected on ultrasound imaging.....	32
Figure 2.13: TG-43 coordinate system. ⁵⁰	37
Figure 3.1: Ultrasound imaging of the prostate. ² (A) Axial view showing the transition zone (TZ) and the peripheral zone (PZ). The interface between the zones is marked (*). (B) Sagittal view.	57
Figure 3.2: T2-weighted magnetic resonance image of the prostate. ² (A) Axial and (B) coronal views showing the zonal anatomy.	58
Figure 3.3: A prostate contour (grey) generated from contour points (x). The indentation (closed lines) was identified by the concave posterior edge, where the sides (circles) were lower than the center (square).....	62
Figure 3.4: Inter-observer contouring variability between 5 observers at the base (left), mid-gland (middle), and apex (right) slices for magnetic resonance (top row) and ultrasound (bottom row) images.	65
Figure 3.5: Inter- (solid) and intra- (diagonal) observer contour variability for prostate volume and dimensions between magnetic resonance (dark gray) and ultrasound (light gray) contours.	65
Figure 4.1: Sagittal view of identical prostate slices of zero thickness (dotted line) and the interpolated prostate volume boundaries (solid lines) as interpreted from planimetry (left) and frustum (right) algorithms.....	78

Figure 4.2: Prostate pair-wise volume difference between planimetry (reference volume) and frustum algorithms. Contours with 3 (N=6) and 4 (N=34) mm inter-slice distances were from magnetic resonance images while 5 mm contours (N=40) were from ultrasound images. Results are presented as average, maximum, and minimum differences.....	80
Figure 4.3: Ellipsoid (dark gray) and truncated cone (light gray) volume reconstruction accuracy using planimetry (solid) and frustum (diagonal) algorithms for various inter-slice distances. Simulations reflected MR and CT imaging. Results are presented as average, maximum, and minimum errors over all offsets.	81
Figure 4.4: Ellipsoid (dark gray) and truncated cone (light gray) volume reconstruction accuracy using planimetry (solid) and frustum (diagonal) algorithms. Simulations reflected US imaging. The first slice was placed at the superior end of the volume.....	82
Figure 5.1: Relative dose percentage error (defined in equation 5.1) from neglecting edema for a simulated prostate phantom. Figure reproduced from Monajemi <i>et al.</i> ⁶	88
Figure 5.2: Post-implant CT image (left) of prostate (blue) and urethra (red) and the Corresponding color map (right) of the relative error (%) in conventional vs. edema-incorporated dosimetry.	91
Figure 6.1: Example of the seed distribution function in 1-D.	97
Figure 6.2: 2-D cross section of the dose kernel grid (blue, open circle) and modified kernel values (red, solid circles) with the physical projection of the seed.	97
Figure 6.3: Right-cumulative volume histogram of the treatment plan dose error for point (light) and line (dark) sources calculated using the FT interpolation (left) and snap-to-grid (right) methods. Voxels with dose greater than 300 Gy were ignored. Values represent mean and range over 10 cases. Note the difference in the vertical scale.....	99
Figure 6.4: Single seed dose kernel interpolation error for the Iodine-125 model 6711 seed represented in the TG-43 formalism as a point (left) and line (right) source. The 2 % error isoline is shown (solid) with the physical projection of the seed (shaded).....	100

Figure 6.5: Post-implant 100, 150, 200 % isodose contours (100 % = 145 Gy) calculated in the TG-43 line source formalism using the snap-to-grid method (dash) and direct calculation (solid). FT interpolation contours were indistinguishable from direct calculation.	101
Figure 6.6: Dose-volume histogram for (from right to left) the prostate, urethra, and rectum calculated in the TG-43 line source formalism using the snap-to-grid method (dash) and direct calculation (solid). FT interpolation plots were indistinguishable from direct calculation.	101
Figure 6.7: Lateral dose profile (solid) 1 cm away from the line source along the seed orientation axis. The 1 mm kernel (point) was under-sampled, resulting in interpolation error (dotted line).	104
Figure 7.1: Optimized registration of ultrasound-based seed locations and needle track segments (red) to fluoroscopy-based seed locations (blue).	114
Figure 7.2: Relationship between seed distribution and prostate contour data.....	116
Figure 7.3: Implanted seed positions for the prostate under ultrasound probe pressure (points) and subsequent movements upon probe removal (arrows). Three movement patterns are shown along with the approximate location of the probe (shaded): elastic decompression in axial view (top), lateral shearing in axial view (middle), and rectal bending in sagittal view (bottom).	117
Figure 7.4: (left) Correlation plot between seed movement and position for a patient without lateral shearing movement. (right) Residual seed movement after tensor regression. Regression line is superimposed.	119
Figure 7.5: (left) Correlation plot exhibiting lateral shearing movement for intra-prostatic (blue) and extra-prostatic (red) seeds. (center) Residual movement after tensor regression. (right) Residual after additional lateral shearing regression for intra-prostatic seeds. ...	120

Figure 7.6: Mid-gland prostate, rectum, and urethra probe-in contours (solid) and estimated contours upon probe removal (dotted). Movement of seeds near mid-gland is superimposed. 121

Figure 7.7: Relationship between whole prostate D_{90} and the trace of the correlation tensor. Red triangles represent patients with strong lateral shearing seed movements. The regression line for patients with minimal lateral shearing seed movements, represented by blue points, is shown for reference purposes. 123

Figure 7.8: Post-implant sagittal CT slice showing the prostate (red) and the bending path of the rectum (blue). The patient superior direction is towards the right. 125

List of Abbreviations

AAPM	American Association of Physicists in Medicine
ABS	American Brachytherapy Society
ADT	Androgen deprivation therapy
AJCC	American Joint Committee on Cancer
AP	Anterior-posterior
AT	Ataxia telangiectasia
CBCT	Cone beam computed tomography
CCI	Cross Cancer Institute
CoM	Center of mass
CT	Computed tomography
CTV	Clinical target volume
DFS	Disease free survival
DRE	Digital rectal examination
DVH	Dose-volume histogram
D _x	Dose that covers x % of the volume
D _{xcc}	Dose that covers of x cc of the volume
EBRT	External beam radiation therapy
EC	Electron capture
EPE	Extra-prostatic extension
ETV	Evaluation target volume
FT	Fourier transform
FIR	Finite impulse response
GTV	Gross tumour volume
GUD	Genitourinary diaphragm
HDR	High dose-rate
I-125	Iodine-125
IIR	Infinite impulse response
IMRT	Intensity modulated radiation therapy
IPSS	International Prostate Symptom Score

LDR	Low dose-rate
LINAC	Linear accelerator
MC	Monte Carlo
MR	Magnetic resonance
MV	Mega-voltage
OAR	Organ at risk
Pd-103	Palladium-103
PPB	Permanent prostate brachytherapy
PSA	Prostate-specific antigen
PTV	Planning target volume
Rh-103	Rhodium-103
SI	Superior-inferior
Te-125	Tellurium-125
TG-43	Task group 43
TPS	Treatment planning system
TRUS	Transrectal ultrasound
TURP	Transurethral resection of the prostate
US	Ultrasound
V _x	Volume receiving at least x % of the prescription dose

List of Symbols

a_L	Correlation coefficient (left side)
a_R	Correlation coefficient (right side)
b_L	Intercept coefficient (left side)
b_R	Intercept coefficient (right side)
\bar{b}_{CoM}	Implant center of mass (3-vector)
β	Angle subtended by the seed
\tilde{C}	Correlation tensor (matrix)
D	Dose from single seed
\dot{D}	Dose-rate from single seed
$D_{implant}$	Dose from entire implant
$D_{implant}^{edema}$	Dose from entire implant accounting for edema
D_{opt}	Modified single seed dose kernel
δ	Delta function
Δ_{edema}	Edema magnitude
Δ_z	Inter-slice distance
Λ	Dose-rate constant
$\bar{\epsilon}$	Fractional shift (3-vector)
$F(r, \theta)$	Anisotropy function (line source)
\mathcal{F}	Fourier transform operator
θ	Angle
$g_L(r)$	Radial dose function (line source)
$g_P(r)$	Radial dose function (point source)
$G_L(r, \theta)$	Geometry function (line source)
h	Lagrange Interpolating Filter
I	Implant distribution function
\dot{K}	Air-kerma rate
n	Number of seeds in implant
N_{grid}	Number of grid points

$\vec{\eta}$	Integer shift (3-vector)
$P(r_0, \theta_0)$	Reference point
$\varphi_{\text{an}}(r)$	Anisotropy function (point source)
r	Radial distance
$RE\%$	Relative dose percentage error for neglecting edema
\mathfrak{R}	Rotation operator
S_K	Air-kerma strength
t	Time
$T_{1/2}$	Radioactive half-life
T_{edema}	Edema resolution time
\vec{u}	Seed position (3-vector)
$(\vec{u})_{\text{Lat}}$	Lat component of the seed position
\vec{v}	Seed movement (3-vector)
$(\vec{v})_{\text{AP}}$	Anterior-posterior component of the seed movement
\vec{x}	Cartesian position (3-vector)
x	Lateral axis
y	Anterior-posterior axis
z	Superior-inferior axis
\otimes	Convolution operator

Chapter 1 Introduction

1.1 Prostate Cancer

1.1.1 Overview

Prostate cancer is the leading malignancy for men, affecting one in seven males during their lifetime. In 2013, an estimated 23,600 cases of prostate cancer are expected to be diagnosed, accounting for one in four of all new cancer cases in Canadian men.¹ The disease has a long natural history and generally progresses slowly but has a high mortality rate if left untreated.

In the 1990s, prostate cancer was one of the leading contributing causes of cancer mortality. The last 3 decades witnessed the introduction of prostate-specific antigen (PSA) testing, advances in ultrasound (US), computed tomography (CT), and magnetic resonance (MR) imaging, and evolution of various forms of radiotherapy treatments. Advances in screening and diagnosis led to early detection of the disease. In combination with modern treatment methods, the mortality rate of prostate cancer has greatly decreased.² Nevertheless, the number of deaths remains substantial due to the high prevalence, estimated to be 3,940 in 2013. Currently, prostate cancer is the 3rd largest contributing cause of cancer deaths in Canadian men at 10 %, after lung (27 %) and colorectal (13 %). Therefore, even a small improvement in prostate cancer care would benefit a significant portion of the population.

1.1.2 Screening and diagnosis

Initial screening for prostate cancer is performed by digital rectal examination (DRE) and PSA testing.³ Both procedures are non-invasive, cost-effective, and widely available. DRE is performed by a physician inserting a gloved finger via the rectum. The posterior surface of the prostate is scanned for palpable signs of cancer, such as lumps or abnormally stiff regions. However, the test is limited to certain regions of the prostate and small early stage diseases often go unnoticed.

Prostate-specific antigen is a protein naturally produced by the prostate and its concentration is measured by a blood test. A high or increased PSA level is a possible indicator for prostate cancer.⁴⁻⁶ The introduction of PSA testing coupled with increased public awareness resulted in a large increase in the number of diagnosed cases in the late 1980's. PSA is also credited with the ability to detect cancers in the early stages, which have more favorable treatment outcome. However, the relationship between PSA and pretreatment prostate cancer is statistically weak.⁷ Over the years, the overall effectiveness of PSA testing alone has been called into question, especially as false-positive results can lead to unnecessary invasive diagnosis procedures. Nevertheless, testing remains widespread and the reported PSA value remains a criterion in prostate cancer diagnosis. Furthermore, PSA testing remains invaluable for prognosis and monitoring after treatment, as described in a later section.⁸

Definitive diagnosis of cancer is performed by prostatic biopsy and quantified by the Gleason score.³ Prostate tissue samples are extracted using biopsy needles inserted under transrectal ultrasound image guidance. The biopsy procedure samples all regions of the prostate. The two most cancerous samples are each graded based on glandular architecture (i.e. how well tissue cells are differentiated) visible under microscopic examination. Each Gleason grade ranges from well differentiated (grade 1) to poorly differentiated (grade 5). The Gleason score is the sum of the two sample grades combined, with a higher score suggesting more advanced disease. Note that biopsy does not show the true spatial extent of the disease. Samples from surgical prostatectomy show that prostate cancer, even at early stages, commonly exhibits multiple microscopic disease foci and extra-capsular penetration.^{9,10}

1.1.3 Cancer stages and risk categories

Cancer progression is described by the clinical stage, incorporating results from PSA testing, DRE, ultrasound imaging, and the Gleason score from biopsy.¹¹ The cancer stage is used to predict the prognosis, determine treatment options, and establish a common framework for disease reporting. The current staging classification is the American Joint Committee on Cancer (AJCC) TNM system.¹² The staging system assesses three

quantities: the primary tumour (T), the involvement of nearby lymph nodes (N), and the presence of distant metastasis (M). Of particular relevance is the T2 stage category for the primary tumour, in which the clinically discernable disease remains confined within the prostate, although there is the possibility of undetected microscopic disease outside. The tumour stage can be further subdivided (i.e. T2a, T2b, T2c). The T3 stage is of greater severity as it is associated with clinical indications that the tumor has penetrated outside the prostate capsule.

Prostate cancer patients are further classified into low, intermediate and high risk groups based on the PSA value, biopsy Gleason score and clinical stage.⁸ The stratification largely reflects the likelihood of proximal seminal vesicle invasion and the extent of extra-prostatic extension (EPE), which strongly influences treatment prognosis and available treatment options.¹⁰ The American Brachytherapy Society (ABS) recommends the following risk group definition:¹³

Low risk – Patients with all of:

- PSA of 10 ng/mL or less
- Gleason score of 6 or less
- Clinical stage of T2a or less

Intermediate risk – Patients with one or more of:

- PSA between 10 and 20 ng/mL
- Gleason score of 7
- Clinical stage T2b or T2c

High risk – Patients with one or more of:

- PSA greater than 20
- Gleason score of 8 to 10
- Clinical stage of T3a

1.1.4 Treatment options

The conventional curative treatment options for localized prostate cancer include brachytherapy, external beam radiation therapy (EBRT) and prostatectomy. Other common options include active surveillance and androgen deprivation therapy (ADT).

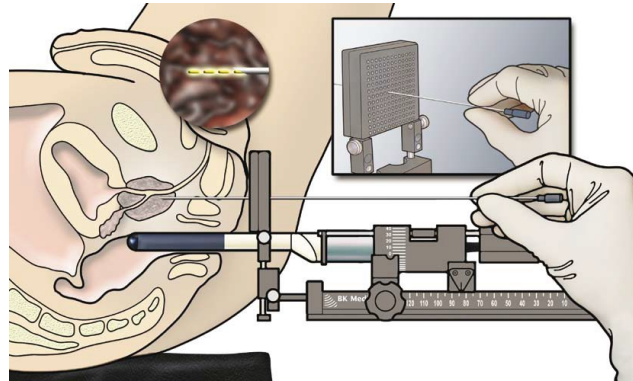


Figure 1.1: Implantation during permanent or low dose-rate prostate brachytherapy.¹⁴

Brachytherapy is a radiation therapy modality involving the placement of radiation source(s) a short distance from the tumor, either inside the target (interstitial) or in a nearby cavity (intra-cavitary).¹⁵ In addition to the prostate, treatment sites include breast, cervix, esophagus, and eye. Brachytherapy treatments can be broadly divided into fractionated high dose-rate (HDR) and continuous low dose-rate (LDR). HDR treatment involves a single high strength source placed sequentially at the planned positions using a remote afterloader and subsequently retracted from the patient. The irradiation at each position lasts no more than several minutes per fraction. A third form of treatment, pulsed dose-rate (PDR), involves a single session of micro-fractionated irradiation that delivers a time-averaged dose rate similar to that in LDR. The LDR procedure (Figure 1.1) involves temporary or permanent implantation of low strength sources to the target in the form of capsules or seeds. Both HDR and LDR sources emit radiation in the kilo-electron volt (keV) range that is attenuated in tissue to varying degrees depending on the photon energy. Cobalt-60, with mean energy of 1.25 MeV, is also used in HDR. The resulting dose distribution is often characterized by a high dose to the target and a steep fall-off away from the target. Consequently, brachytherapy can provide highly localized and conformal dose coverage for organ confined diseases but is of limited use for large treatment volumes.

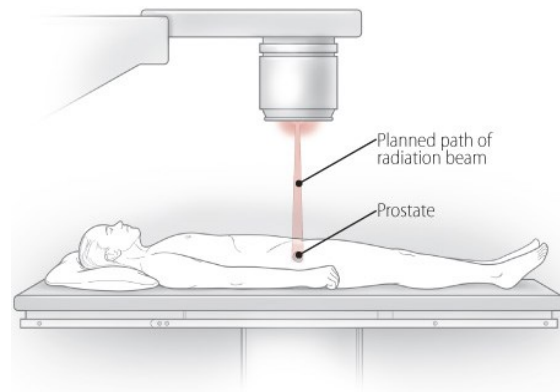


Figure 1.2: External beam radiation therapy for prostate cancer.¹⁶

EBRT is the most prevalent modality of radiation therapy (Figure 1.2). High energy radiation (either photons or electrons) in the mega-electron volt (MeV) range is generated by a linear accelerator (LINAC) and the radiation beam directed to the anatomical target. Photons are used to treat diseases inside the patient, such as prostate cancer, while electrons treat malignancies near the surface. Mega-voltage (MV) photon beams are highly penetrating, irradiating all tissue along the path of the beam. To deliver high dose to the target while preventing high dose concentration in surrounding normal tissue, beams are delivered from different directions, resulting in focused dose to the intersecting region. Treatment is completely non-invasive and consists of daily series of fractions, typically 5 days a week, for 7 weeks. Current LINAC-based treatment delivery such as intensity modulated radiation therapy (IMRT) greatly improves dose conformity to the target. The use of advanced image guidance such as cone beam computed tomography (CBCT) significantly improves targeting accuracy.

Prostatectomy involves the surgical removal of the prostate gland and the adjacent seminal vesicles. After removal of the prostate, the urethra is reattached to the bladder. A nerve-sparing procedure can be performed to preserve erectile function. The invasive procedure is limited to healthy patients and to disease confined to the prostate. Prostatectomy is frequently combined with EBRT to treat potential microscopic EPE.

Prostate cancer is generally a slow growing disease. For patients with limited life expectancy, the cancer may not be life threatening and curative treatment may constitute

unnecessary harm to the patient. In such cases, a physician may instead recommend active surveillance, regularly monitoring the disease using a combination of PSA testing, DRE, and biopsy. However, there is a risk that the disease will progress to a more advanced stage, negatively affecting treatment prognosis.

Patients unsuitable for any of the preceding treatment options may be treated with ADT. Testosterone is an androgen hormone that stimulates prostate cancer cell growth. Reducing the patient's testosterone level would slow the disease progression and can be achieved by pharmaceutical drugs. Orchiectomy, the surgical removal of the testicles, also prevents testosterone production but is less commonly performed. However, the effectiveness of ADT decreases over time and the disease will eventually continue to spread.

1.1.5 Treatment outcome endpoints

After treatment, patients are monitored for possible recurrence of the cancer. Various clinical endpoints are used to describe the outcome of prostate cancer treatment: biochemical recurrence-free survival, disease free survival (DFS), overall survival. Biochemical recurrence-free survival describes the absence of biochemical failure based on PSA levels. Following successful treatment, the PSA value decreases significantly to its lowest or nadir value, often below 1 ng/mL. A subsequent increase in PSA is an indicator for possible recurrence. The Phoenix definition of biochemical failure is a PSA value of "nadir + 2 ng/mL".^{13,17} Disease free survival describes the absence of clinical evidence of cancer, based on tests such as DRE and ultrasound imaging. Overall survival describes whether a patient is alive or has died due to the cancer. The efficacy of a particular treatment for a cohort of patients is often presented as a survival curve, which plots the survival rate as a function of time after start of treatment, with particular emphasis at the 5 and 10 year time points.

1.2 Permanent Prostate Brachytherapy

1.2.1 Overview

Permanent prostate brachytherapy (PPB) is an LDR brachytherapy treatment for prostate cancer, delivering radiation dose via implantation of radioactive sources in the prostate and surrounding target volume. The treatment aims to deliver a dose distribution tailored to the patient, maximizing dose to the target while minimizing dose to healthy normal tissue. The earliest documented transperineal brachytherapy procedure dates back to the 1930's, where needles were guided by a finger in the rectum.¹⁸ The contemporary method of transrectal ultrasound (TRUS) -guided transperineal PPB was introduced in 1983 by Holm *et al.* and further developed by Ragde, Blasko, and Grimm.¹⁹

1.2.2 Patient eligibility

Patient selection criteria are outlined in the American Brachytherapy Society recommended guidelines.^{13,20} Patients in the low risk cohort (as defined in section 1.1.3) have a high likelihood of organ-confined disease and can be treated with brachytherapy alone (i.e. brachytherapy as monotherapy). The distance of EPE is limited and an extension of the treatment margin beyond the prostate is sufficient for dose coverage. Patients in the intermediate group have increased risks of EPE, proximal seminal vesicle invasion, and proximal lymph node involvement. Due to the limited effective treatment range of a PPB implant, additional supplementary EBRT is recommended for adequate dosimetric coverage outside the prostate. However, the extent of extra-prostatic disease varies and brachytherapy alone can be considered on a case-by-case basis. High risk patients have a substantial risk of extra-prostatic disease and ABS recommends a combined treatment using brachytherapy and EBRT.

Patients with any of the below absolute contraindications are poor candidates for PPB:

^{13,20}

- Limited life expectancy
- Unacceptable operative risks
- Distant metastases

- Absence of rectum
- Large transurethral resection of the prostate (TURP) defects
- Ataxia telangiectasia (defined below)

Patients with limited life expectancy (roughly less than 10 years) are unlikely to benefit from PPB treatment, as disease progression is generally slow. Parts of the procedure (i.e. needle insertion, anesthesia) may pose an unacceptable risk for some patients. Metastatic disease, if present, is aggressive and is the dominant consideration in outcome prognosis. PPB alone is ineffective for treating distant disease, although it can be used in combination with other treatment options. Patients without a rectum preclude the use of the TRUS probe for image guidance. Patients previously treated with TURP have a greater chance of seed loss and increased sensitivity to high urethra dose, limiting the region for implantation. For large defects, the limitations may compromise the target dose coverage. Ataxia telangiectasia (AT) is a rare genetic defect affecting DNA replication and repair. Patients with AT are extremely sensitive to ionizing radiation and are not considered for any form of radiation therapy, including brachytherapy.

Patients with the following relative contraindications have an increased risk of toxicity and are not ideal candidates for PPB, although they can be successfully implanted: ^{13,20}

- Small TURP defects
- High International Prostate Symptom Score (IPSS)
- Inflammatory bowel disease
- Large prostate volume
- Previous radiation therapy

The IPSS questionnaire tracks the patient's quality of life concerning urinary function. Patients with a high IPSS or inflammatory bowel disease have preexisting urinary or bowel symptoms which may be exacerbated by PPB treatment. Prostate volumes are generally between 30 and 50 cc. Volumes greater than 60 cc may be difficult to implant. The increased number of needle insertions and resulting bleeding and swelling from trauma due to needle insertions may result in unacceptable interference with US imaging

and movement of the prostate. In addition, large prostates have an increased likelihood of pubic arch interference (see section 2.3.7). For such cases, short term ADT is commonly used before treatment to shrink the prostate volume. Small volumes, although not a contraindication, are difficult to implant due to the increased sensitivity of dosimetry to implantation errors.

1.2.3 Treatment procedure

The PPB procedure consists of 3 stages: treatment planning, implantation, and post-implant evaluation. During treatment planning, the pelvic region is surveyed on US and the prostate and relevant structures are defined. An implant source distribution is generated that meets the planning dose criteria. The implantation procedure, performed in the operating room, is minimally invasive and aims to deliver a dose distribution closely matching that on the treatment plan. Sources, also known as seeds, of roughly 1 mm diameter and 5 mm length are implanted using surgical needles inserted via a transperineal approach, mechanically guided using a template grid and visually guided by TRUS probe imaging (see Figure 1.1). Post-implant evaluation assesses the completed implant dosimetry, ensuring adequate dose delivery to the target. The PPB procedure is presented in detail in Chapter 2.

1.2.4 Treatment outcome

The current approach to brachytherapy is highly successful in the treatment of low and intermediate risk prostate cancer. Morris *et al.* reported a 10-year DFS rate of 94 % for 1006 consecutive patients.²¹ Crook *et al.* reported a 7-year DFS rate of 95 % for a cohort of 1111 patients.²²

Direct comparison between treatment options is complicated by the non-uniform reporting of results and clinical end-points.²³ The continuous evolution of each treatment modality also makes long-term outcome comparisons difficult. In a multi-institutional analysis of low and intermediate risk patients, Grimm *et al.* reported competitive biochemical outcome for brachytherapy compared to other treatment options.²³ However, it is important to note that prostate brachytherapy practice varies widely between

institutions and is highly dependent on the skill and experience of individual practitioners.²⁴⁻²⁶

1.2.5 Treatment toxicity

Complications from PPB treatment develop 2 weeks after implantation and are generally temporary and well tolerated.¹¹ Minor urinary side effects include increased frequency and urgency to void. Painful voiding and ejaculation has also been reported. Rectal symptoms include general discomfort, loose stool, or diarrhea. Approximately 10 % of patients experience urinary obstruction requiring temporary intervention. Late developing (up to 5 years) obstructive urinary symptoms may also develop in 5 % of patients. Severe rectal injury is reported in less than 1 % of cases. Although accurate data collection is difficult, a majority of patients report retention of their sexual function after PPB treatment.

1.3 Research Motivation

1.3.1 Importance of Dosimetry

Dosimetry, the calculation and assessment of the energy deposited by ionizing radiation, is a crucial aspect in PPB, and radiation therapy in general. The prescription dose of 145 Gy is recommended by the American Association of Physicists in Medicine (AAPM) and is generally considered to be the minimum effective dose for cancer treatment.²⁷

Insufficient dose to the target volume (i.e. under-dosing) has a negative impact on cancer control. Although the temptation might be to treat with as high a dose as possible, the dose to target is commonly limited by nearby critical structures, referred to as organs at risk (OARs). The likelihood and severity of treatment toxicity increase with increasing dose to OARs.^{28,29} The dosimetric goal of PPB treatment is therefore to plan and deliver a dose distribution tailored to the patient, providing adequate dose coverage (i.e. at minimum the prescription dose) to the target volume while minimizing dose to critical structures.

Current advances in PPB dosimetry focus on improving the spatial accuracy and conformity of the delivered dose distribution and the numerical accuracy of clinical

brachytherapy dose calculation.^{27,30-32} Delivery accuracy influences the planning criteria necessary to account for potential delivery errors. A dose distribution conformal to the target volume minimizes radiation to the surrounding normal tissue. The improvements aim to minimize dose to normal tissue, potentially reducing treatment toxicity.

Alternatively, they allow for escalation of the target dose while maintaining the same level of toxicity, potentially improving treatment efficacy for higher risk diseases. Dose calculation error during planning results in a sub-optimal treatment plan while the calculation accuracy during post-implant dosimetry affects the predictive power of outcome evaluation and clinical trials.

1.3.2 Overview of dissertation

The current dissertation attempts to critically assess some of the limitations and assumptions inherent in PPB dosimetry, covering all 3 stages of the treatment procedure. Where possible, the thesis provides novel insights and practical improvements with the goal of improving PPB dosimetry. The research assesses prostate delineation accuracy for treatment planning, seeks to improve PPB dose calculation for planning and evaluation, and investigates perturbations in treatment due to the US probe. The thesis is outlined as follows.

Chapter 2 provides a comprehensive description of the PPB monotherapy procedure, providing the technical background for the dissertation. The pelvic anatomy relevant to PPB is presented. The treatment is outlined according to the three aforementioned stages: treatment planning, implantation, and post-implant evaluation. The current methodology for clinical dose calculation is described. Finally, the impact of various uncertainties and factors in the PPB procedure on treatment dosimetry is discussed, providing the context for the research topics presented in the subsequent chapters.

The planned dose distribution is tailored to the target volume, which is derived from the prostate delineated on US imaging. Over-estimation of the target would result in higher dose to the surrounding normal tissue, potentially increasing treatment toxicity. Under-estimating the target would negatively impact the dose coverage, with potential

implications for cancer control. Chapter 3 investigates whether MRI, which provides superior soft tissue contrast, can provide superior prostate delineation compared to US during treatment planning.³³ MR and US imaging was performed separately for each patient. Prostate contours from the two imaging modalities were compared in terms of volume, shape, and observer contouring variability. Chapter 4 is a supplementary study, investigating the discrepancy between prostate volumes calculated using two reconstruction algorithms, one commonly employed for MR and another for US imaging.³⁴ Systematic volume differences due to the algorithms could be mistaken for contouring bias between the imaging modalities. Therefore, the accuracy of the two volume calculation algorithms was evaluated within the context of MR and US image acquisition. The results from simulated acquisition and reconstruction of geometries with known volumes were used to estimate the systematic algorithm-associated error in clinical prostate volume determination.

Post-implant dosimetry results correlate with clinical outcome and are used to anticipate possible treatment failure and toxicity, allowing for the physician to respond accordingly. Currently, evaluation assumes the implanted prostate at the time of imaging is static over the radioactive lifetime of the sources. However, the resolution of prostatic edema (i.e. swelling of the prostate) due to needle insertion trauma causes movement of the implanted seeds relative to the prostate, resulting in deviations from reported dosimetry. Chapter 5 investigates the dosimetric impact using a clinically-informed edema model combined with edema parameters derived from prostates contoured on MR.^{35,36} The edema model, describing the dynamic movement of the implanted seeds and internal prostate volume, was incorporated into clinical patient dose calculations. Results were compared to conventional calculations for a static seed distribution and prostate. Chapter 6 outlines a novel dose kernel interpolation method for PPB dose calculations that mitigates the significant increase in computation time associated with calculations incorporating prostatic edema.³⁷ The proposed method expands upon a previously reported method for fast PPB dose calculation, using the Fourier transform (FT).³⁸ Limitations relating to seed placement in the original method resulted in unacceptable dose calculation errors. The proposed FT-based interpolation method applies an

additional offset filter, interpolating the dose kernel for each seed. The novel method substantially improved PPB dose calculation accuracy while preserving the computation efficiency of the original method.

Changes to the prostate after implantation result in implanted seed movement, potentially resulting in further deviation from the planned implant distribution. Such movement would be a contributing factor to the discrepancy between the planned and delivered dosimetry. The effects of prostate deformation due to transrectal US probe pressure are discussed in the literature but the dosimetric impact has not been investigated, due to the contouring uncertainty relative to the small magnitude of this movement. Chapter 7 presents an investigation using a novel approach that infers the internal prostate deformation from the implanted seed movements, which can be determined with higher accuracy compared to the prostate contour. Implanted seed positions were localized first for the prostate under probe compression and then with the probe removed. A heuristic deformation model was developed to capture the spatial correlation between seed movement and position. The model was used to infer the underlying prostate deformation and to estimate the change in prostate dosimetry upon probe removal.

Chapter 8 concludes the dissertation with a summary of research results and presents a discussion on potential directions for future research.

1.4 References

- 1 Canadian Cancer Society's Advisory Committee on Cancer Statistics, *Canadian Cancer Statistics* (Canadian Cancer Society, Toronto, 2013).
- 2 P.A. Kupelian, J.C. Buchsbaum, M.A. Elshaikh, C.A. Reddy, E.A. Klein, "Improvement in relapse-free survival throughout the PSA era in patients with localized prostate cancer treated with definitive radiotherapy: year of treatment an independent predictor of outcome." *Int. J. Radiat. Oncol. Biol. Phys.* **57**, 629-634 (2003).

- 3 B. Thomadsen, M. Rivard, W. Butler, *Brachytherapy Physics*, 2nd ed. (Medical Physics Publishing, Madison, WI, 2005).
- 4 T.A. Stamey, N. Yang, A.R. Hay, J.E. McNeal, F.S. Freiha, E. Redwine, "Prostate-specific antigen as a serum marker for adenocarcinoma of the prostate." *N. Engl. J. Med.* **317**, 909-916 (1987).
- 5 T.A. Stamey, J.N. Kabalin, J.E. McNeal, I.M. Johnstone, F. Freiha, E.A. Redwine, N. Yang, "Prostate specific antigen in the diagnosis and treatment of adenocarcinoma of the prostate. II. Radical prostatectomy treated patients." *J. Urol.* **141**, 1076-1083 (1989).
- 6 T.A. Stamey, J.N. Kabalin, M. Ferrari, "Prostate specific antigen in the diagnosis and treatment of adenocarcinoma of the prostate. III. Radiation treated patients." *J. Urol.* **141**, 1084-1087 (1989).
- 7 T.A. Stamey, M. Caldwell, J.E. McNeal, R. Nolley, M. Hemenez, J. Downs, "The prostate specific antigen era in the United States is over for prostate cancer: what happened in the last 20 years?" *J. Urol.* **172**, 1297-1301 (2004).
- 8 A.V. D'Amico, R. Whittington, S.B. Malkowicz, D. Schultz, K. Blank, G.A. Broderick, J.E. Tomaszewski, A.A. Renshaw, I. Kaplan, C.J. Beard, A. Wein, "Biochemical outcome after radical prostatectomy, external beam radiation therapy, or interstitial radiation therapy for clinically localized prostate cancer." *JAMA* **280**, 969-974 (1998).
- 9 C. Salembier, P. Lavagnini, P. Nickers, P. Mangili, A. Rijnders, A. Polo, J. Venselaar, P. Hoskin, G.E.C.E.P. Group, "Tumour and target volumes in permanent prostate brachytherapy: a supplement to the ESTRO/EAU/EORTC recommendations on prostate brachytherapy." *Radiother. Oncol.* **83**, 3-10 (2007).
- 10 B.J. Davis, T.M. Pisansky, T.M. Wilson, H.J. Rothenberg, A. Pacelli, D.W. Hillman, D.J. Sargent, D.G. Bostwick, "The radial distance of extraprostatic extension of

- prostate carcinoma: implications for prostate brachytherapy." *Cancer* **85**, 2630-2637 (1999).
- 11 A. Tewari, *Prostate Cancer: A Comprehensive Perspective*, 1st ed. (Springer, London, 2013).
- 12 S.B. Edge, D.R. Byrd, C.C. Compton, A.G. Fritz, F.L. Greene, A. Trotti, *American Joint Committee on Cancer Cancer Staging Manual*, 7th ed. (Springer, New York, 2010).
- 13 B.J. Davis, E.M. Horwitz, W.R. Lee, J.M. Crook, R.G. Stock, G.S. Merrick, W.M. Butler, P.D. Grimm, N.N. Stone, L. Potters, A.L. Zietman, M.J. Zelefsky, A.B. Society, "American Brachytherapy Society consensus guidelines for transrectal ultrasound-guided permanent prostate brachytherapy." *Brachytherapy* **11**, 6-19 (2012).
- 14 Image from B&K Medical, <http://www.analogicultrasound.com/>, retrieved May 14, 2014.
- 15 E.B. Podgorsak, *Radiation Oncology Physics: A Handbook for Teachers and Students*, 1st ed. (International Atomic Energy Agency, Vienna, 2005).
- 16 S. Leighton, <http://www.harvardprostateknowledge.org/>, retrieved Jun 10, 2014.
- 17 M. Roach, G. Hanks, H. Thames, P. Schellhammer, W.U. Shipley, G.H. Sokol, H. Sandler, "Defining biochemical failure following radiotherapy with or without hormonal therapy in men with clinically localized prostate cancer: recommendations of the RTOG-ASTRO Phoenix Consensus Conference." *Int. J. Radiat. Oncol. Biol. Phys.* **65**, 965-974 (2006).
- 18 J.N. Aronowitz, "Dawn of prostate brachytherapy: 1915-1930." *Int. J. Radiat. Oncol. Biol. Phys.* **54**, 712-718 (2002).
- 19 J.N. Aronowitz and M.J. Rivard, "The phylogeny of permanent prostate brachytherapy." *J Contemp Brachytherapy* **5**, 89-92 (2013).

- 20 S. Nag, D. Beyer, J. Friedland, P. Grimm, R. Nath, "American Brachytherapy Society (ABS) recommendations for transperineal permanent brachytherapy of prostate cancer." *Int. J. Radiat. Oncol. Biol. Phys.* **44**, 789-799 (1999).
- 21 W.J. Morris, M. Keyes, I. Spadinger, W. Kwan, M. Liu, M. McKenzie, H. Pai, T. Pickles, S. Tyldesley, "Population-based 10-year oncologic outcomes after low-dose-rate brachytherapy for low-risk and intermediate-risk prostate cancer." *Cancer* **119**, 1537-1546 (2013).
- 22 J. Crook, J. Borg, A. Evans, A. Toi, E.P. Saibishkumar, S. Fung, C. Ma, "10-year experience with I-125 prostate brachytherapy at the Princess Margaret Hospital: results for 1,100 patients." *Int. J. Radiat. Oncol. Biol. Phys.* **80**, 1323-1329 (2011).
- 23 P. Grimm, I. Billiet, D. Bostwick, A.P. Dicker, S. Frank, J. Immerzeel, M. Keyes, P. Kupelian, W.R. Lee, S. Machtens, J. Mayadev, B.J. Moran, G. Merrick, J. Millar, M. Roach, R. Stock, K. Shinohara, M. Scholz, E. Weber, A. Zietman, M. Zelefsky, J. Wong, S. Wentworth, R. Vera, S. Langley, "Comparative analysis of prostate-specific antigen free survival outcomes for patients with low, intermediate and high risk prostate cancer treatment by radical therapy. Results from the Prostate Cancer Results Study Group." *BJU Int.* **109 Suppl 1**, 22-29 (2012).
- 24 M. Keyes, J. Crook, W.J. Morris, G. Morton, T. Pickles, N. Usmani, E. Vigneault, "Canadian prostate brachytherapy in 2012." *Can Urol Assoc J* **7**, 51-58 (2013).
- 25 G.S. Merrick, W.M. Butler, K.E. Wallner, J.C. Blasko, J. Michalski, J. Aronowitz, P. Grimm, B.J. Moran, P.W. McLaughlin, J. Usher, J.H. Lief, Z.A. Allen, "Variability of prostate brachytherapy pre-implant dosimetry: a multi-institutional analysis." *Brachytherapy* **4**, 241-251 (2005).
- 26 L. Beaulieu, D.R. Evans, S. Aubin, S. Angyalfi, S. Husain, I. Kay, A. Martin, N. Varfalvy, E. Vigneault, P. Dunscombe, "Bypassing the learning curve in permanent seed implants using state-of-the-art technology." *Int. J. Radiat. Oncol. Biol. Phys.* **67**, 71-77 (2007).

- 27 R. Nath, W.S. Bice, W.M. Butler, Z. Chen, A.S. Meigooni, V. Narayana, M.J. Rivard, Y. Yu, American Association of Physicists in Medicine, "AAPM recommendations on dose prescription and reporting methods for permanent interstitial brachytherapy for prostate cancer: report of Task Group 137." *Med. Phys.* **36**, 5310-5322 (2009).
- 28 M.J. Zelefsky, T. Hollister, A. Raben, S. Matthews, K.E. Wallner, "Five-year biochemical outcome and toxicity with transperineal CT-planned permanent I-125 prostate implantation for patients with localized prostate cancer." *Int. J. Radiat. Oncol. Biol. Phys.* **47**, 1261-1266 (2000).
- 29 S.H. Stokes, J.D. Real, P.W. Adams, J.C. Clements, S. Wuertzer, W. Kan, "Transperineal ultrasound-guided radioactive seed implantation for organ-confined carcinoma of the prostate." *Int. J. Radiat. Oncol. Biol. Phys.* **37**, 337-341 (1997).
- 30 M.J. Rivard, J.L.M. Venselaar, L. Beaulieu, "The evolution of brachytherapy treatment planning." *Med. Phys.* **36**, 2136-2153 (2009).
- 31 M.J. Rivard, B.M. Coursey, L.A. DeWerd, W.F. Hanson, M.S. Huq, G.S. Ibbott, M.G. Mitch, R. Nath, J.F. Williamson, "Update of AAPM Task Group No. 43 Report: A revised AAPM protocol for brachytherapy dose calculations." *Med. Phys.* **31**, 633-674 (2004).
- 32 Y. Yu, L.L. Anderson, Z. Li, D.E. Mellenberg, R. Nath, M.C. Schell, F.M. Waterman, A. Wu, J.C. Blasko, "Permanent prostate seed implant brachytherapy: report of the American Association of Physicists in Medicine Task Group No. 64." *Med. Phys.* **26**, 2054-2076 (1999).
- 33 D. Liu, N. Usmani, S. Ghosh, W. Kamal, J. Pedersen, N. Pervez, D. Yee, B. Danielson, A. Murtha, J. Amanie, R.S. Sloboda, "Comparison of prostate volume, shape, and contouring variability determined from preimplant magnetic resonance and transrectal ultrasound images." *Brachytherapy* **11**, 284-291 (2012).

- 34 D. Liu, N. Usmani, R.S. Sloboda, "Transrectal ultrasound based prostate volume determination: is the frustum algorithm more accurate than planimetry?" *Med. Phys.* **40** (2013).
- 35 T.T. Monajemi, C.M. Clements, R.S. Sloboda, "Dose calculation for permanent prostate implants incorporating spatially anisotropic linearly time-resolving edema." *Med. Phys.* **38**, 2289-2298 (2011).
- 36 R.S. Sloboda, N. Usmani, J. Pedersen, A. Murtha, N. Pervez, D. Yee, "Time course of prostatic edema post permanent seed implant determined by magnetic resonance imaging." *Brachytherapy* **9**, 354-361 (2010).
- 37 D. Liu and R.S. Sloboda, "Fast dose kernel interpolation using Fourier transform with application to permanent prostate brachytherapy dosimetry." *Med. Phys.* **41** (2014).
- 38 A.L. Boyer and E.C. Mok, "Brachytherapy seed dose distribution calculation employing the fast Fourier transform." *Med. Phys.* **13**, 525-529 (1986).

Chapter 2 Permanent Prostate Brachytherapy

2.1 Overview

This chapter provides a detailed description of the PPB procedure implemented at the Cross Cancer Institute (CCI), providing the technical background to the research topics presented in later chapters. The first section highlights information on the pelvic anatomy relevant to PPB. The treatment planning, implantation, and post-implant evaluation procedures are presented, followed by the current AAPM recommended Task Group No. 43 (TG-43) methodology for clinical brachytherapy dose calculations. The final section discusses how various factors that come into play during the PPB procedure influence treatment dosimetry, providing the dosimetric context for the dissertation.

2.2 Anatomy

This section describes the prostate and the surrounding pelvic anatomy as relevant to PPB treatment. Anatomical structures are delineated and can be designated as either target or OAR. The proximity of OARs may limit implant placement in order to avoid dose to critical structures. Adjacent structures can introduce additional uncertainties in contouring, directly affecting the planned dose distribution. PPB also involves additional anatomical considerations unique to the treatment, such as interference of needle insertion by the pubic arch and the risk of seed migration depending on the implanted seed location.

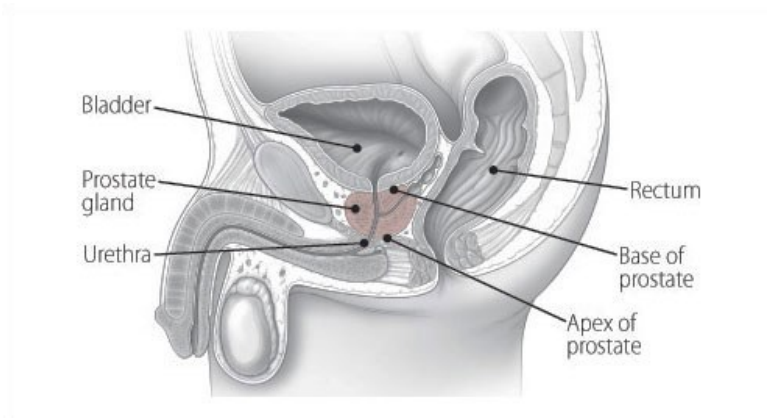


Figure 2.1: The male pelvic region, showing the prostate and adjacent structures.¹

The prostate gland is part of the male reproductive system, contributing to the production of seminal fluid. The prostate is located in the pelvis region (Figure 2.1), positioned inferior to the bladder and anterior to the rectum. The gland, roughly the size of a walnut, has a shape often described as an inverted pyramid, with the larger superior end referred to as the base while the narrow inferior end is called the apex. The urethra runs centrally through the prostate. Additional structures include the seminal vesicles located superior-posterior to the prostate and the genitourinary diaphragm (GUD) located directly anterior. The remaining surface of the prostate, particularly the lateral region, is attached to various connective tissues as part of the pelvic musculature. Nerve bundles controlling bladder and erectile functions are also located on the lateral surfaces of the prostate. The pubic bone, part of the pelvis structure, forms an arch anterior-inferior to the prostate.

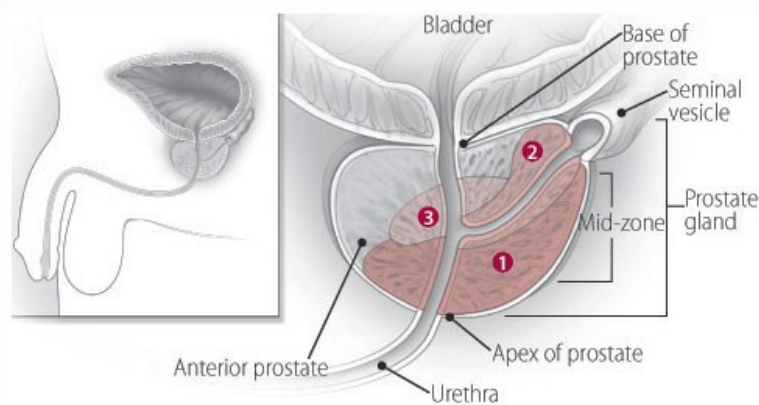


Figure 2.2: Illustration of the internal prostate anatomy, divided into the peripheral zone (1), central zone (2), transition zone (3) and the anterior region.¹

The prostate is divided into four regions: central zone, transition zone, peripheral zone, and anterior region (Figure 2.2).^{2,3} The central zone encloses the duct connecting to the seminal vesicle. The transition zone is situated in the prostate center. The peripheral zone, occupying the largest region, encapsulates the central and transition zones towards the posterior and lateral aspects. The anterior fibromuscular stroma region consists of non-glandular tissue.

Zonal considerations can sometimes play a role in disease progression and detection. The peripheral zone contains the majority of secretory glandular elements and is the region

most susceptible to cancer of the prostate. DRE is limited to detecting prostate abnormalities in the peripheral zone due to its proximity to the rectum. Abnormalities in the central zone, furthest away from the rectum, cannot be detected by DRE. Nevertheless, it is important to note that prostate cancer is a multifocal disease and multiple biopsy insertions are performed to sample all regions of the prostate. Currently, zonal considerations play a limited role in PPB treatment.

2.3 Treatment Planning

A pre-operative planning study is performed several weeks before the scheduled implantation date.⁴ The treatment planning procedure strives to generate an implant distribution that meets the dosimetric criteria, providing adequate dose to the target while minimizing urethral and rectal dose. The steps involved include delineating the prostate and relevant nearby structures, defining the treatment volume, and determining the implant (i.e. number, activity, and position of implanted seeds) required for target coverage. Pre-operative planning should also ensure a smooth and expedient implantation, with the planned needle insertions technically simple to implement and potential complications from pubic arch interference identified.

2.3.1 Ultrasound volume study



Figure 2.3: (left) Transrectal ultrasound probe with console system in background.⁵ (right) Endocavity balloon filled with water solution.⁶



Figure 2.4: (left) Manual stepper for probe positioning. (right) The imaging system ultrasound transducer and support assembly: probe attached to stepper mounted on a stabilizer.⁶ Template grid located above the probe is used only during implantation.

Imaging of the prostate is performed using a B&K model 8848 TRUS probe in combination with the Pro-Focus 2002 system console (Analogic Ultrasound, Peabody, MA), as shown in Figure 2.3. The probe is attached to a manual stepper device for precise longitudinal movement and mounted on an adjustable stabilizer (Civco Medical Solutions, Orange City, IA) (Figure 2.4). The patient is set up in the lithotomy position and the probe, covered in a water balloon, is inserted into the rectum. The combination of a water solution in the balloon and applied probe pressure ensure adequate probe contact for good US image quality. For urethra visualization, an aerated gel is injected into the urethra via a catheter.



Figure 2.5: Transverse and sagittal views of the prostate under transrectal ultrasound imaging.

The TRUS probe is bi-planar, with two sets of transducer arrays, and is capable of obtaining two-dimensional (2-D) transverse or sagittal images as shown in Figure 2.5. Sagittal imaging is used to determine the superior-inferior (SI) extent of the prostate. The

transverse imaging plane is then positioned such that the prostate base is just visible. A three-dimensional (3-D) volume study is created from sequential transverse images acquired from the base to the apex at 5 mm retractions using the stepper. Acquired serial US images are stored in the VariSeed (version 8.0, Varian Medical Systems Inc., Palo Alto, CA) treatment planning system (TPS).

2.3.2 Contouring and volume definitions

The prostate and nearby OARs (bladder, rectum, and urethra) are delineated by manual contouring by a radiation oncologist. The treatment volume is generated by adding a margin to the prostate contour. The prostatic urethra is defined as the urethra segment located inside the prostate. Volume definitions vary between brachytherapy centers, resulting in potentially substantial variation in treatment plans.⁷ The recommended common approach for volume definition is outlined in the AAPM TG-137 report.⁸

The gross tumour volume (GTV) is defined as the gross palpable, visible, or demonstrable extent and location of the malignant growth. Based on the clinical stage definition, the GTV can only be defined for T2 stage diseases and above.

The clinical target volume (CTV) is defined to be the GTV plus a margin to account for potential sub-clinical disease. Prostate cancer exhibits multiple disease foci and EPE, even in the early stages and regardless of the number of positive biopsy samples.⁹ The posterior-lateral regions of the prostate are noticeably susceptible to EPE but the distance is limited to 5 mm for disease clinically confined to the prostate.¹⁰ Therefore, the CTV includes the whole prostate plus a non-uniform margin 2 to 3 mm anteriorly and laterally and 5 mm superiorly and inferiorly. The posterior margin is 0 mm.¹¹

The planning target volume (PTV) contains the CTV plus an additional margin to account for uncertainties during treatment delivery such as patient setup error, target movement, and target volume and shape changes.⁸ The definition of a PTV is primarily intended for EBRT and it is common in PPB for the PTV to be identical to the CTV. Setup error is minimal in PPB as the implant is delivered under image guidance.

Uncertainties in implant delivery are instead compensated for by more stringent planning criteria (presented in section 2.3.4), also referred to as over-planning.

2.3.3 Radioactive isotopes

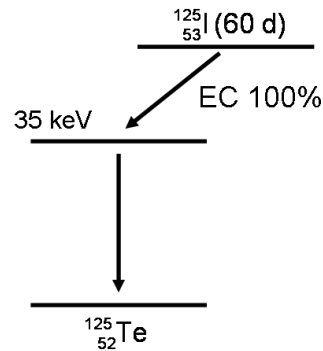


Figure 2.6: Nuclear decay scheme for Iodine-125.

PPB implants are commonly performed using Iodine-125 (I-125) or Palladium-103 (Pd-103) sources; both are similar in radiation quality.^{4,12} The I-125 emission spectrum has photon peaks at 27.4, 31.4, and 35.5 keV (mean energy 28 keV) and I-125 has a radioactive half-life of 59.4 days. Figure 2.6 illustrates the decay scheme for I-125, which undergoes electron capture (EC) decay to an excited state of Tellurium-125 (Te-125) followed by de-excitation predominately by internal conversion (93 %) and gamma emission (7 %). Additional fluorescent x-rays are emitted as a result of vacancies from the electron capture and internal conversion interactions. Pd-103 has slightly lower photon energies at 20.1 and 23.0 keV (mean energy 21 keV) and a significantly shorter radioactive half-life of 17 days. Pd-103 undergoes electron capture to an excited state of Rhodium-103 (Rh-103) followed by internal conversion and gamma emission. Currently, there is no recommendation of using one radionuclide over another.^{10,13}

2.3.4 Planning criteria

The commonly used prescription dose, as calculated using the TG-43 formalism, is 145 Gy for I-125 monotherapy and 125 Gy for Pd-103.⁸ Dose recommendations are based on retrospective dose-response analysis of post-implant data. Specifically, the dose to 90 % of the prostate volume, D_{90} , is determined to be a statistically significant predictor of biochemical outcome.¹⁴⁻¹⁶ It is important to note that literature prior to publication of the

TG-43 formalism in 1995 uses a prescription dose of 160 Gy, which is equivalent to 144 Gy under the current formalism (see section 2.6.1 for more detail).¹⁰

Uncertainties in implant delivery and other factors (presented in section 2.7) result in an overall lower delivered dose to the target compared to the treatment plan. To achieve adequate dose coverage for post-implant dosimetry, AAPM recommends the following planning dosimetric criteria, which are more stringent:⁸

Clinical target volume:

- V_{100} (volume receiving at least 100 % prescription dose) greater than 95 %; D_{90} will be higher than the prescription dose (close to 180 Gy)¹⁰
- V_{150} equal to or less than 50 %

Rectum:

- D_{2cc} less than the prescription dose
- $D_{0.1cc}$ less than 150 % the prescription dose

Prostatic urethra:

- D_{10} less than 150 % the prescription dose
- D_{30} less than 130 % the prescription dose

2.3.5 Planning the implant

<i>Dose parameter</i>	<i>Objective (%)</i>
PTV V100	>98
PTV V150	≤65
PTV V200	≤25
PTV D90	120– 130
Urethra D5	<215 Gy
Rectum D1cc	<145 Gy

Table 2.1: Planning dosimetry criteria for permanent prostate brachytherapy performed at the Cross Cancer Institute. Note that PTV = CTV.

The implant distribution, reflecting the activity, number, and position of seeds, is determined in order to satisfy the pre-implant dosimetric criteria presented in Table 2.1. The seed activity is quantified by the air kerma strength, with unit of U, representing the rate of kinetic energy imparted from ionizing photons to electrons (kerma) in an air

medium (see section 2.6.1 for more details). The CCI currently employs seeds of intermediate source strength (uniform strength of 0.5 U) and uses approximately 100 seeds per implant on average, but the exact number can vary from about 75 to 125 depending on prostate volume.¹⁷ The possible discrete positions for seed placement lie on a 3-D lattice grid of uniform 5 mm spacing. After the treatment plan is finalized, the required set of seeds for the implant is ordered from the vendor.

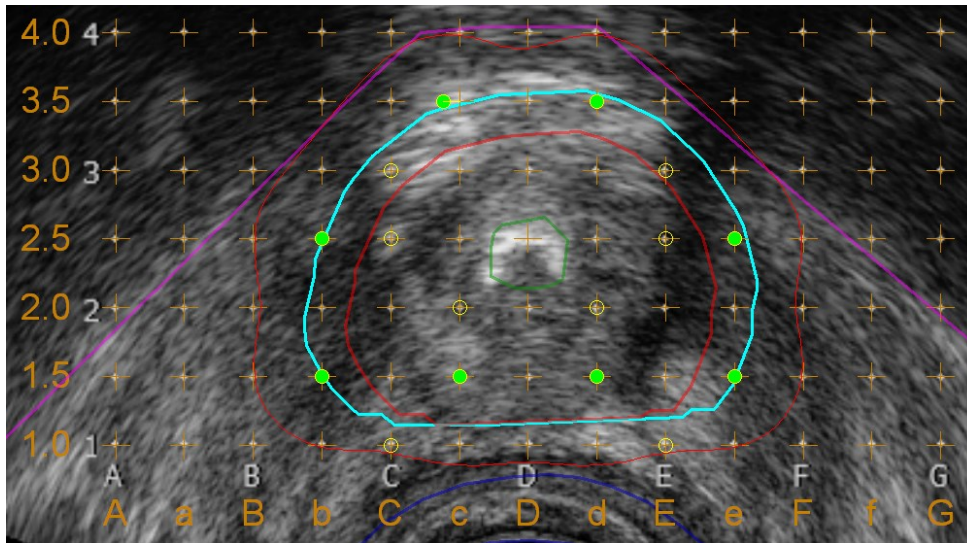


Figure 2.7: Transverse ultrasound image from a treatment plan showing the prostate contour (red line), PTV (cyan line), 145 Gy isodose (thin red line), urethra (green line), rectum (blue line), pubic arch (purple line), virtual template grid (+), planned needle insertions (both open and solid circles), planned seed positions at that image slice (solid circles).

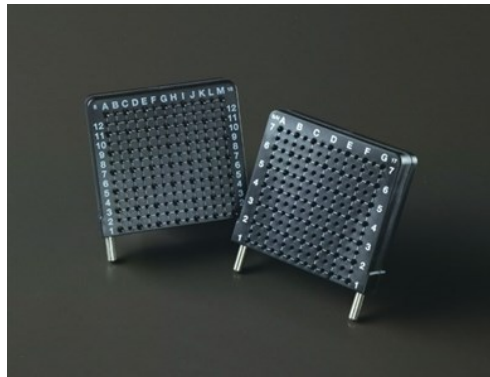


Figure 2.8: Physical template grid corresponding to the virtual grid displayed on the ultrasound image used in treatment planning.⁶

Figure 2.7 shows a transverse slice at the prostate mid-gland from a representative treatment plan. A virtual template grid is superimposed, identifying the lateral and anterior-posterior grid coordinates in terms of columns (A through G) and rows (1 to 4).

The virtual grid corresponds and is calibrated to a physical template used during implantation to guide needle insertion, shown in Figure 2.8. The superior-inferior position of each US slice in the 3-D volume study is given by the retraction, defined as the distance inferior from the base slice. Marked grid points show each planned needle insertion, and seeds are positioned away from the urethra. The 145 Gy prescription isodose line is shown to encompass the PTV. The projection of the pubic arch shows the prostate is clear from interference.

Implant distributions are commonly determined by a loading pattern, based on a set of rules or nomogram.¹⁸ The majority of patterns currently employed fall within a spectrum between two extremes originating from early PPB experiences: uniform loading and peripheral loading.⁸ The uniform loading approach uses a large number of low strength seeds (~ 0.4 U), uniformly placed on the implant grid, both inside and outside of the prostate, with 1 cm spacing. The pattern reflects an ‘outside-in’ approach, where dose coverage at the target periphery is achieved by placing some seeds outside of the prostate and projecting the dose inwards. However, the cumulative dose in the central prostate resulted in extremely high urethral doses and unacceptably high urinary morbidity. In contrast, peripheral loading places high strength seeds (~ 0.7 U) exclusively within the prostate, reflecting an ‘inside-out’ approach where coverage at the target periphery is achieved by projecting the dose outwards. The latter dose distribution is characterized by high dose gradients sparing the rectum and urethra. However, there is significant risk of under-dosing the central prostate.

Contemporary loading patterns evolved from either historic approach and were modified to address the respective weaknesses. The CCI approach to source strength selection and source placement falls between the modified uniform and peripheral loading schemes.⁸ Needle locations are limited to within 2 mm outside the prostate contour at the mid-gland. There are no strict limitations on needle and seed spacing, although the attempt is made to ensure these are as uniform as the planning objectives will allow.

With technological advances in computing, implant distributions can alternatively be determined using an automated inverse planning algorithm, based on optimization methods such as simulated annealing.^{19,20} Dosimetric criteria for optimization include dose-volume metrics for the target and OARs. Additional criteria such as dose uniformity and needle density can also be defined reflecting the user's planning philosophy. Each criterion is associated with a user-defined weighting factor, indicating its importance relative to other criteria. The inverse planning algorithm returns the optimized implant distribution reflecting the criteria and their weighting. Inverse planning is not done at the CCI as the quality and practicality (e.g. number of needles used is minimized) of plans produced by commercially available algorithms has been found to be inferior to that of plans created by experienced planners.

2.3.6 Intra-operative planning

Conventional treatment planning is performed after a separate patient visit to acquire TRUS images well ahead of the implantation date, and is referred to as pre-planning. In contrast, some brachytherapy centers employ intra-operative planning, performing the pre-operative planning procedures in real-time immediately prior to implantation.²¹ Intra-operative planning aims to overcome potential disadvantages of pre-operative planning that does not consider factors such as prostate volume and shape changes.²² Volume change is primarily due to ADT while application of anesthesia during implantation results in muscle relaxation and potential prostate shape change. Additionally, intra-operative planning avoids the need to replicate the patient setup and TRUS planning images. Wilkinson *et al.* reported significantly improved post-implant dosimetry results for patients who have undergone intra-operative planning compared with pre-planning.²³

The procedure for intra-operative planning is similar to pre-planning, but involves greater time constraints for both physician and physicist with potentially less time for quality assurance. Also, the additional time spent in the operating room results in increased monetary cost. Technological advances have been introduced to facilitate efficient and timely treatment planning. An automated segmentation algorithm can be used to generate the prostate, urethra, and rectum contours. The physician would modify the contours,

greatly reducing the contouring time compared to completely manual delineation. The addition of margins can also be generated automatically. An inverse planning algorithm is commonly used to determine the optimized treatment plan.

Intra-operative planning is not performed at the CCI. The merits of pre-planning versus intra-operative planning remain a topic of discussion.^{24,25} The dependence on experience and planning philosophy and the continuous improvements in technique and equipment makes direct comparison difficult. Nevertheless, experienced brachytherapy centers report excellent and comparable dose coverage and patient outcomes, regardless of planning approach.

2.3.7 Pubic arch interference

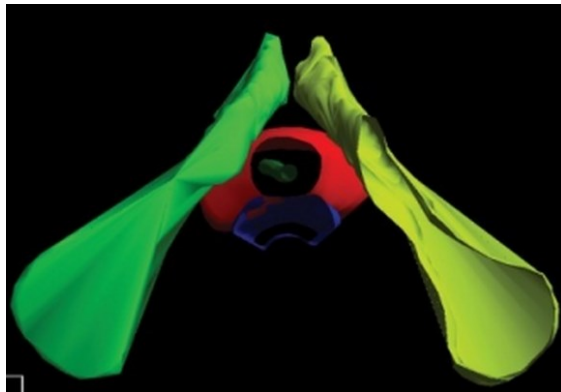


Figure 2.9: Pubic arch interference, determined and reconstructed from computed tomography imaging, as observed from the transperineal approach. The prostate (red) periphery is partially obscured by the left (yellow) and right (green) pubis bony structure.

Patients with prostate volumes greater than 60 cc have an increased likelihood of pubic arch interference, impeding needle insertion to the lateral and anterior regions of the target (as seen in Figure 2.9).⁴ The degree of interference is evaluated from the US study by contouring the pubic arch located inferior to the apex and projecting the contour towards the largest prostate contour at the mid-gland (see Figure 2.7). If potential interference exists, short term ADT can be administered to reduce the prostate volume prior to treatment. Severe interference is a contraindication for PPB implantation.

2.4 Implantation

PPB implantation, performed in the operating room, aims to deliver the planned implant distribution as closely as possible. Implantation is performed by a radiation oncologist trained in brachytherapy technique and lasts approximately an hour. Implantation is an outpatient procedure, not requiring overnight hospital stay.

2.4.1 Preparation and setup

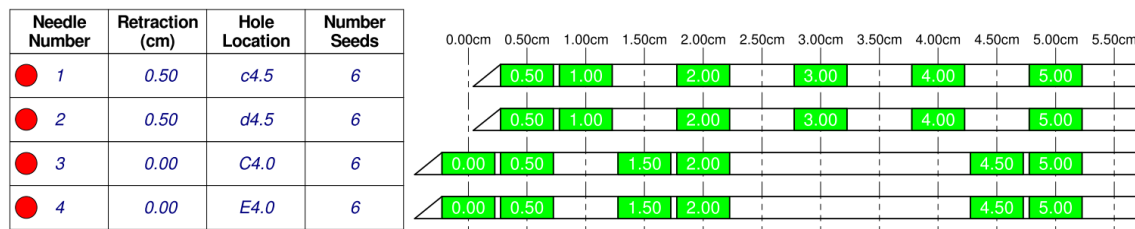


Figure 2.10: A sample of the treatment plan sent to the vendor when ordering the implant, illustrating the needle loading.

For each implant performed at the CCI, a set of vendor-ordered seeds are delivered as an operating-room-ready pack of custom strands pre-loaded into needles. Each strand consists of a train of seeds and spacers arranged according to the patient's treatment plan (Figure 2.10) and encased in absorbable stranding material. Spacers are non-radioactive, variable-length elements placed between the seeds and are used to ensure separation between radioactive seeds along the needle track. The use of a single seed (no spacers) per needle is generally avoided during planning due to increased risk of post-implant seed migration (section 2.5.4).

Five loose seeds from the same manufacturing lot as the seeds used by the vendor to build the strands are assayed locally for dosimetric quality assurance purposes.^{4,26} The assay is performed using a well ionization chamber to independently confirm the manufacturer's reported seed strength. The chamber is calibrated by an accredited dosimetry calibration laboratory and with the calibration traceable to the National Institute of Standards and Technology (USA).

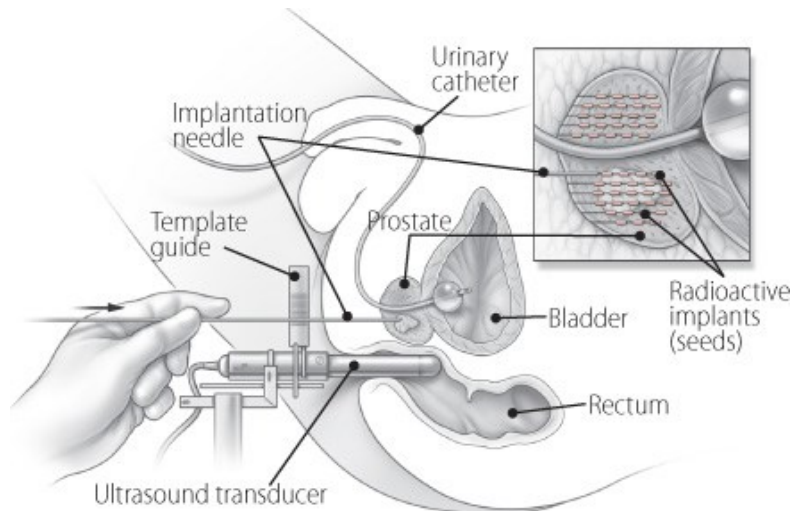


Figure 2.11: Implantation procedure in PPB.¹

The patient is set up in the lithotomy position to replicate the pre-planning study (Figure 2.11). Local or general anesthesia is administered to the patient under the supervision of an anesthesiologist. The perineum is cleaned with an anti-septic agent. A catheter is inserted into the urethra and aerated gel is injected for urethra visualization.

Alternatively, a Foley catheter can be inserted through the urethra into the bladder.

Ultrasound imaging is set up to replicate the pre-planning study. The probe position and angle are adjusted to reproduce the images and prostate position acquired for treatment planning. Some brachytherapy centers insert a pair of stabilizing needles in an attempt to immobilize the prostate and limit prostate lateral and anterior-posterior (AP) movement during needle insertion.²⁷ Radiation oncologists at the CCI have previously investigated the use of stabilizing needles on a trial basis, but found that they offered little or no benefit when incorporated in CCI implant technique.

2.4.2 Implantation

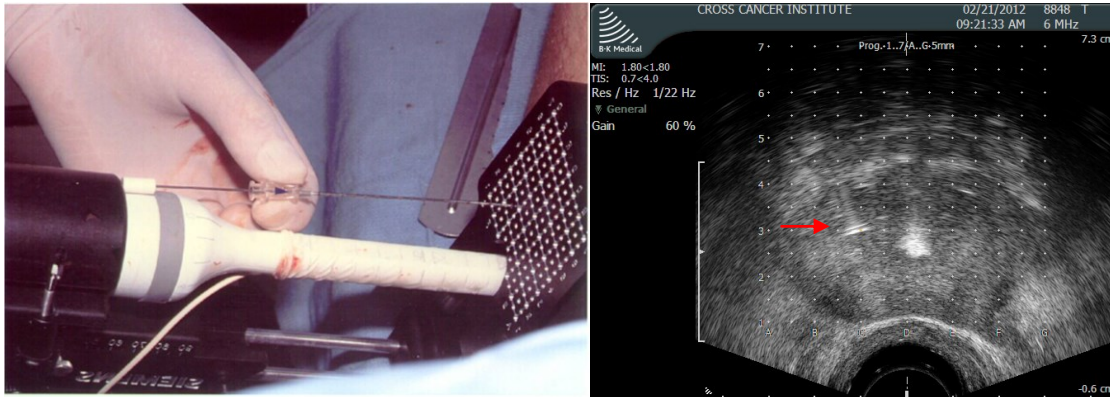


Figure 2.12: (left) Needle insertion during implantation. (right) The needle as detected on ultrasound imaging.

Implantation, consisting of needle insertion followed by seed deposition, is performed one needle at a time. Using a transperineal approach, the bevel-tipped needle is inserted through the template guide at the planned grid position (Figure 2.12 left). The insertion is performed in a single controlled movement, with care taken to avoid the bladder superior of the prostate. The deviation of the inserted needle from the planned position is observed on US and recorded on the TPS. The tip of the needle is moved to the proper retraction depth and verified on US (Figure 2.12 right). With the strand held in place by a stylet supplied with the pre-loaded needle, the needle is retracted, thus depositing the entire strand along the needle track.

An alternative after-loading approach to implantation utilizes the Mick applicator.⁴ The unloaded needle is inserted as previously described. The applicator contains separate cartridges for seeds and spacers and is connected to the proximal end of the inserted needle. The needle is retracted in steps and seeds and spacers are deposited one at a time along the track according to the treatment plan. The Mick applicator technique is commonly employed for intra-operative brachytherapy, where implantation is performed immediately after the planned loading patterns are determined.

Real-time modifications to the planned implant may be necessary during implantation, either to compensate for misplacement of implanted seeds or differences from the

preplan, which might include prostate shape and volume changes or an OAR observed to be too close to the planned position of a seed. The TPS can be used to calculate the delivered dose based on the recorded needle deviation and the dosimetric impact of performing the modification.

Finally, an inspection of the entire implanted prostate is performed on US. The implant is surveyed for potential under-dose areas, or cold spots. Two extra needles, containing 3 and 2 seeds separated by spacers, respectively, are available for additional implantation if required.

2.5 Post-Implant Evaluation

The purpose of post-implant evaluation is to assess the delivered implant dosimetry, ensuring adequate dose delivery to the target.^{4,8} Imaging is usually performed on CT, which can visualize the implanted seeds while providing reasonable soft-tissue contrast for delineation of the prostate and OARs. Factors affecting the accuracy of evaluation include prostatic edema, migration of implanted seeds, and contouring uncertainties.

2.5.1 CT volume study

CT is the recommended imaging modality for post-implant evaluation, due to the ability to visualize both implanted seeds and the prostate boundary.⁸ At CCI the scan is performed the day of implantation but can be acquired up to one month post-implant at some brachytherapy centers. The patient is placed in the supine position on the scanning bed (in contrast to the lithotomy position for US imaging) and is imaged using 3 mm slice thickness. Acquired CT images are transferred to the VariSeed TPS where the prostate (often referred to as the evaluation target volume, or ETV), urethra, and rectum are delineated by the implanting radiation oncologist. Contrast enhancement is required for urethra visualization on CT. Implanted seeds are automatically localized by the TPS and subsequently confirmed by visual inspection.

2.5.2 Evaluation of delivered dose

Dosimetric evaluation is performed on the TPS. The implanted TG-43 dose distribution is calculated using the seed positions localized on CT. The calculated isodose lines are

superimposed on CT images along with structure contours, enabling visual confirmation of the spatial distribution of the dose coverage. Dose-volume histograms (DVHs) of the target and OARs are generated. Dosimetric parameters used in the evaluation process represent selected points on the DVHs. The primary parameters recommended for reporting are outlined in the TG-137 report and consist of the prostate D_{90} , V_{100} , V_{150} , prostatic urethra D_{10} and rectum D_{2cc} .⁸

2.5.3 Timing of post-implant evaluation

Edema, or swelling, of the prostate is caused by surgical trauma from needle insertion during seed implantation.^{28,29} Build-up occurs within the time of implantation and reaches peak edema magnitude within a day of implantation.³⁰ Subsequent resolution of the edema yielding roughly the original prostate volume occurs over the period of about one month. The extent of edema varies between patients and likely also depends on the implantation technique and the density of needle insertions. Edema expansion is anisotropic, present in the AP and SI directions while practically absent in the lateral direction.

Edema resolution over time causes individual seeds to move relative to the prostate and to other seeds. Therefore, the timing of post-implant CT image acquisition, representing a snapshot in time, has an effect on the calculated dosimetry. The reported ETV dose would be lower if imaging was performed immediately after implantation, whereas imaging after complete edema resolution would ignore the swelling and over-estimate the reported dose. As evaluation of an I-125 implant (including evaluation done for dose response studies) is traditionally performed one month following the PPB procedure, the AAPM recommends post-implant imaging 1 month \pm 1 week after the procedure (16 ± 4 days for Pd-103).⁸ Logistics and patient considerations also play a practical role in setting the timing, in which case it is important to establish a consistent time to minimize artificial fluctuations in reported dosimetry due to edema. At the CCI, post-implant evaluation on the day of implantation (i.e. day 0) allows for early treatment quality assurance and corrective intervention if necessary.

2.5.4 Implant migration

Implanted seeds can migrate along the residual needle track. The majority of the movement is small, resulting in minor changes in implant spatial distribution. However, large movements have been reported, resulting in distant migration from the prostate region to the lung, abdomen, and pelvis.³¹ One possible mechanism for distant seed migration involves inferior movement along the residual needle path into the GU diaphragm and subsequent migration via muscle contraction.³² Another mechanism is the superior migration into the bladder, resulting in seed loss via the urethra. For implants in the lateral venous anatomy, pulmonary embolization in the lungs may occur if the seed escapes into the circulatory system.^{33,34}

The frequency of distant migration also depends on seed placement philosophy, with increased risk for extra-prostatic implanted seeds.³⁵ Accurate implantation, either avoiding extra-prostatic placement or specific peri-prostatic venous anatomy, can mitigate distal migration.^{36,37} The introduction of stranded seeds, a train of seeds and spacers encased in stranding material, was designed to further improve seed fixity and minimize migration.^{4,35} Usmani *et al.* reported sub-millimeter migration for stranded implants in which RapidStrand[®] material (Oncura, a division of GE Healthcare, Arlington Heights, IL) was used, significantly decreasing migration of extra-prostatic seeds.³⁸ However, there are reported instances of migration of the entire strand if it is anchored outside the prostate, such as in the GUD.³² Such migration risk reaffirms the importance of careful implant placement, regardless of the use of stranding.

2.5.5 Contouring uncertainty

Large contouring uncertainty, particularly in the delineation of the prostate base and apex, is associated with the limited soft tissue contrast available on CT.^{8,13} Interfaces separating the prostate from surrounding anatomy (i.e. bladder, levator ani muscle, neurovascular bundles, genitourinary diaphragm) are not easily distinguishable.^{39,40} The overall effect is an overestimation of the prostate spatial extent, although local underestimation has also been reported in the posterior region. Reported CT pre-implant prostate volumes are systematically larger compared to volumes determined from US and MR images,

which better display the prostate boundary.⁴¹ Both inter- and intra- observer variability are also larger on CT. McLaughlin *et al.* addresses common contouring errors on CT and suggests methods for improved delineation without the need for additional imaging.³⁹ CT contouring accuracy is further degraded for the post-implant prostate, although US and MR modalities are also negatively affected.^{40,42,43} The metal encapsulation of the seed (commonly titanium) results in CT imaging artifacts that obscure the prostate boundary.⁴⁴

2.5.6 Alternative imaging modalities

Highly accurate post-implant dosimetry can be achieved using a combination of CT and MR imaging (i.e. CT-MR fusion).⁴⁵ MR images have superior soft tissue contrast compared to CT, resulting in accurate delineation of the prostate and surrounding structures.⁴¹ Dosimetry is thus calculated using the seeds localized on CT and contours delineated on MR. Data from the two imaging studies is combined via rigid spatial registration performed on the TPS. The use of MR to supplement post-implant CT evaluation is recommended if resources are available.^{4,8}

An alternative post-implant evaluation method in development is the combined use of C-arm fluoroscopy imaging at two or more projection angles and ultrasound imaging.⁴⁶⁻⁴⁸ The implant is localized using fluoroscopy while the prostate contour is delineated on US. Registration of the US images with the reconstructed seed images obtained from fluoroscopy is performed using a subset of seeds visible on US.⁴⁹ The setup allows for real-time dosimetric evaluation immediately after implantation while the patient remains in the treatment position. The method would be particularly useful for intra-operative brachytherapy, where automated seed detection and dynamic dose calculation would allow for real-time refinement of the treatment plan during implantation.²¹

2.6 TG-43 Dose Calculation

The current AAPM recommended methodology for clinical brachytherapy dose calculation is the TG-43 formalism, originally proposed in 1995 and updated in 2004.^{12,50} The formalism parameterizes the single seed dose-rate distribution from a brachytherapy source. The total PPB implant dose distribution is the superposition of individual seed

dose distributions, integrated over the radioactive decay time. The previous protocol, based on radiation exposure in air, calculates the seed dose-rate distribution based on a point source. In contrast, the TG-43 formalism directly parameterizes the dose-rate in a water medium under full scatter conditions. The transition in methodology enables the parameterization of an anisotropic dose-rate distribution, reflecting the effects of source geometry. In addition, the publication of consensus TG-43 parameters specific to each seed model allows for standardized dose calculation across brachytherapy centers. Two formalisms are outlined in the task group reports: the two dimensional (2-D) formalism representing a cylindrically symmetric line source; and the one-dimensional (1-D) formalism representing a spherically symmetric point source.

2.6.1 Two-dimensional formalism

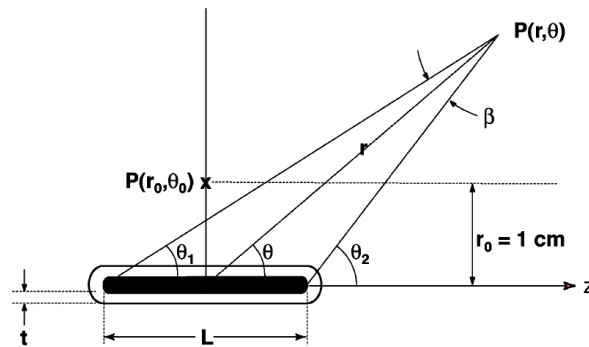


Figure 2.13: TG-43 coordinate system.⁵⁰

Figure 2.13 illustrates the 2-D TG-43 coordinate system specified by the radial distance r and the angle θ , with rotational symmetry about the seed orientation axis. The reference point, $P(r_0, \theta_0)$, is defined to be 1 cm away on the transverse plane of the seed ($\theta_0 = \pi/2$). Eq. 2.1 defines the line source equation for the dose-rate \dot{D} at a point $P(r, \theta)$ located with respect to the center of the active core of the seed.

$$\dot{D}(r, \theta) = S_K \times \Lambda \times \frac{G_L(r, \theta)}{G_L(r_0, \theta_0)} \times g_L(r) \times F(r, \theta) \quad (2.1)$$

The TG-43 parameterization decouples various physical factors in calculating the dose-rate. The absolute dose-rate at the reference point is given by the product of the air-kerma strength S_K and the dose-rate constant Λ . The dose-rate distribution, relative to the

reference point, is calculated from the geometry function $G_L(r,\theta)$, radial dose function $g_L(r)$ and anisotropy function $F(r,\theta)$.

The air-kerma strength S_K reflects the activity of the source.¹² This quantity is defined as the air-kerma rate \dot{K} in vacuum at the reference point and has units of $1 \text{ U} = 1 \mu\text{Gy m}^2 \text{ h}^{-1} = 1 \text{ cGy cm}^2 \text{ h}^{-1}$. In the clinic, the air-kerma strength is measured using a calibrated well ionization chamber as part of the seed strength quality assurance assay performed prior to implantation. The current primary standard uses a Wide-Angle Free-Air Chamber (WAFAC) with an 8 deg aperture positioned 30 cm from the source along the transverse plane. The reading is corrected for attenuation and scattering in air and normalized to the reference distance (Eq. 2.2).

$$S_K = \dot{K}(r) \times r^2 \quad (2.2)$$

The measurement methodology of the air-kerma strength was modified with the introduction of the WAFAC primary standard in 1999.⁵⁰ Low energy photons, specifically the 5 keV Titanium k-shell x-rays from the source capsule, were eliminated using an aluminum filter. The photons contribute to the detector reading in a free-air measurement but would be attenuated within 1 mm of tissue and do not contribute to the clinically relevant dose distribution. The inclusion of the photons in the previous 1985 standard resulted in higher reported dose and the AAPM recommends a correction factor of 0.897. Thus, the previous prescription dose of 160 Gy becomes 144 Gy. The definition of the air-kerma strength was revised in the update of the TG-43 report.⁵⁰

The dose-rate constant Λ is the dose-rate to water at the reference point per unit air-kerma strength and has units of $\text{cGy h}^{-1} \text{ U}^{-1}$. The conversion represents differences in photon attenuation and scattering conditions in the medium, and the ratio of attenuation coefficients at the reference point. The quantity is dependent on the radionuclide and the seed geometry, such as the distribution of radioactivity within the source, and on capsule self-filtration. The dose-rate constant is specific to each seed model.

The geometry function accounts for the relative variation of the dose-rate in the absence of attenuation and scatter in the medium. The function can be interpreted to represent the

relative distribution of an ideal line source in vacuum. Eq. 2.3 defines the line source geometry function $G_L(r, \theta)$. β is the angle subtended by the length L of the radioactive material inside the capsule.

$$G_L(r, \theta) = \begin{cases} \frac{\beta}{Lr \sin \theta} & \text{if } \theta \neq 0 \\ (r^2 - L^2/4)^{-1} & \text{if } \theta = 0 \end{cases} \quad (2.3)$$

The purpose of the geometry function is to isolate the approximate dose-rate behaviour of the source in the absence of attenuation and scattering in the medium (i.e. inverse-square function for the point source). The use of the geometry function serves a practical purpose as the resulting radial dose function and anisotropy function are more smooth and well-behaved. This facilitates accurate calculation of the functions, where linear interpolation is sufficient.

The product of the radial dose function $g_L(r)$ and ratio of geometry functions $G_L(r, \theta)/G_L(r_0, \theta_0)$ gives the dose-rate in the transverse plane relative to the reference point. The 2-D anisotropy function $F(r, \theta)$ accounts for dose-rate anisotropy relative to a point on the transverse plane at the same radial distance. Data for each seed model is supplied either in tabular form or, optionally for the radial dose function, as a fitted polynomial.

Current TPS dose calculations using the 2-D formalism assume the implanted seeds are aligned parallel to the imaging axis. Determination of implant orientation given the limited spatial resolution on CT in the scan direction is problematic, although methods have been proposed to infer the orientation for stranded seeds.⁵¹

2.6.2 One-dimensional formalism

Eq. 2.4 defines the TG-43 formalism for the point source.

$$\dot{D}(r) = S_K \times \Lambda \times \left(\frac{r_0}{r}\right)^2 \times g_P(r) \times \varphi_{an}(r) \quad (2.4)$$

The definitions of air-kerma strength and dose-rate constant remain unchanged from the 2-D formalism. The geometry function is represented by the inverse square function. Although the definition of the radial dose function remains conceptually the same, tabular

values differ between the two formalisms because the point and line source geometry functions are different, especially at small distances near the seed. The 1-D anisotropy function $\phi_{an}(r)$ represents the dose-rate averaged over the entire 4π steradian solid angle.

At large distances, the distribution of radioactive material within a seed can be approximated as a point source and the difference between the point source and line source formalisms is small. Near the seed ($r < 1$ cm), the effects of the source distribution become noticeable and the line source formalism significantly improves dose calculation accuracy.⁵⁰

2.6.3 Dose-rate integral

The TG-43 equation calculates the dose-rate from a seed with a given air-kerma strength, which decays exponentially with time. The total dose is calculated by integrating the dose-rate over the life time of the source. For an implant seed distribution that is static over time, the integration simplifies to a multiplication factor (Eq. 2.5).

$$D = \int_0^{\infty} \dot{D}(t) dt = \dot{D}(0) \times \frac{T_{1/2}}{\ln 2} \quad (2.5)$$

The initial dose rate $\dot{D}(0)$ is calculated for the air-kerma strength at time of implant. $T_{1/2}$ is the half-life of the radioactive isotope.

2.6.4 Formalism limitations

The TG-43 formalism calculates the dose to a small mass of water in a homogenous water medium under full scattering conditions. Dose calculations for a PPB implant result in errors primarily relating to both the elemental composition of prostate tissue and the heterogeneity of the implanted prostate, in particular strong photon attenuation by other seeds and prostate calcifications.⁵² The errors reflect differences in attenuation and scattering conditions, altering the photon fluence at the calculation point. In a published study of these effects, accounting for inter-seed attenuation typically resulted in a prostate D_{90} decrease of 1~3 %, while the difference between water and tissue medium was estimated at 4 %.⁵³ Alternative dose calculation methods are available. Monte Carlo (MC) methods are currently the gold standard for radiotherapy dose calculations.

Afsharpour *et al.* developed ALGEBRA based on the Geant4 MC toolkit.⁵⁴ Taylor *et al.* developed Brachydose based on the EGSnrc code.⁵⁵ Poon *et al.* developed BrachyGui based on the PTran code.⁵⁶ Chibani *et al.* developed MCPI based on the MCNP code.⁵⁷ More recently, a calculation method based on numerically solving the linear Boltzmann transport equation has been introduced.^{58,59}

2.7 Factors affecting brachytherapy dosimetry

The dosimetric goal of PPB treatment is to deliver a dose distribution tailored to the patient, ideally giving the full prescription dose to the entire ETV while minimizing dose to neighbouring critical structures. Three distinct procedures comprising PPB each play a crucial role towards that goal. Treatment planning generates an implant distribution that meets the desired planning dose criteria. The implantation procedure places the seeds as closely as possible to their planned implant positions, delivering the dose as calculated in the treatment plan. Post-implant evaluation is performed to confirm adequate dose to the target, to predict the risk of treatment failure and to allow for additional intervention if deemed necessary.

The patient-specific dosimetric outcome is affected by many factors during the course of PPB treatment. The treatment plan is influenced by the target volume definition and also by the planning philosophy of the practitioner. Implant delivery is affected by the patient setup and the implantation accuracy, both also influenced by the practitioner. Post-implant dosimetry is primarily affected by prostate delineation and the potential movement of the prostate and implant over time. The cumulative impact of selected factors can be significant. In particular, delivery of the treatment plan dose distribution is rarely (if ever) achieved exactly, primarily reflecting limitations in implantation accuracy but also involving selected aspects of post-implant dosimetry. To ensure adequate dose coverage, the AAPM recommends that planning criteria are applied more stringently in practice.⁸ Typically, the planned prostate D_{90} is approximately 190 Gy while the resulting post-implant D_{90} is approximately 150 Gy.^{60,61}

2.7.1 Treatment planning

The treatment plan dose distribution is tailored to conform to the planning target volume, which includes the delineated prostate plus a margin. Thus, the accuracy of US prostate contours and selection of treatment margins directly affect the planned dose distribution. Over-estimation of the target would result in higher dose to the surrounding normal tissue, while under-estimating the target would negatively impact the dose coverage. The accuracy of the prostate contour relates to the imaging quality on US and the physician contouring methodology, while the margin reflects the assessed risk of EPE. Literature on the dosimetric impact due to US contouring variability is limited, although investigations related to delineation on post-implant CT are widely available (section 2.5.5). Note that unlike CT contouring studies, the dosimetric changes are complicated by the fact that the planned dose distribution changes with the planning contour.

Planning an implant distribution is an under-determined problem, with countless solutions satisfying the dosimetric constraints. Treatment plans vary greatly between brachytherapy centers and possibly between physicians, reflecting individual planning philosophies. A physician emphasizing a robust implant would prioritize a plan where the dose distribution is insensitive to seed misplacement error. Avoiding seeds at adjacent grid positions would improve dose homogeneity. Merrick *et al.* reported significant variation in preplan dosimetry between several brachytherapy centers, despite the use of identical prostate contours.⁷ It is important to emphasize that brachytherapy is a highly skill-based procedure and that individual variations in planning and implantation reflect the physician's approach to and philosophy concerning the procedure.

2.7.2 Implant delivery

Prostate volume and shape differences observed on US images obtained for the treatment preplan and during implantation result in displaced implant delivery relative to the prostate.⁴ Prostate changes can reflect anatomical changes over time, the reproducibility of the preplan US study, and the possible impact of hormone therapy. In such cases, strict adherence to the treatment plan during implantation would result in sub-optimal dose delivery. Beaulieu *et al.* reported a 6 % loss in prostate V_{100} coverage, although the

impact on D_{90} was minimal.²² Note, however, that the dosimetric consequences of minor prostate volume and shape changes can be mitigated by adjustments to the plan during implantation.²⁵

Prostatic edema, in addition to influencing post-implant dosimetry, also has an effect during implantation, further contributing to deviations from the treatment plan. Chira *et al.* reported edema build-up during time of implantation, gradually resulting in mismatch between the planning contour and the prostate visible on US.³⁰ Unlike the differences occurring between planning and implantation mentioned above, changes to the prostate due to edema are not accounted for by intra-operative planning.

Implantation accuracy, or the ability to deliver the seed at the intended position, is a dominant source of uncertainty affecting PPB dosimetry.⁴ The two steps involved, needle insertion and seed deposition, respectively determine the implantation accuracy in the axial plane and along the needle axis.^{62,63} The effectiveness of stabilizing needles in improving needle insertion accuracy is questionable.⁶⁴

The PPB implant is planned on a virtual uniform grid corresponding to the physical template. An insertion angle normal to the template should place the needle through the intended grid point. Deviation from the intended needle path is due to splaying and deflection effects, resulting in axial displacement of the needle as a function of depth. Needle splaying is characterized by the deviation of the initial needle angle at the template. Needle deflection describes the bending of the needle inside tissue due to the asymmetric bevel tip. The combined effect is largest at the prostate base, with reported needle displacement of up to 6 mm.⁶³ The displacement due to needle deflection alone is estimated at 3 mm.⁶⁵

Accurate needle placement is further complicated by deformation and movement of the non-rigid prostate in response to needle introduction. Insertion pressure from the needle tip significantly alters the shape of the prostate. The prostate, held in place by the pelvic musculature, is also displaced superiorly towards the base. Once punctured, the prostate

roughly recovers to its original shape and position, but the effects of deformation and movement are visible from the non-straight residual needle track after needle retraction.

Strand placement is commonly characterized by the position of the most superior or initial seed in a strand and by the relative spacing of seeds within the strand.⁶³

Misplacement of the initial seed can occur due to suction forces during seed deposition or dragging of the strand during needle retraction. Relative spacing within the strand can be affected by compression of the strand due to dragging of the prostate during needle retraction followed by the subsequent recovery.

Deviations from the planned implant distribution, reflecting the combined uncertainties of needle insertion and seed deposition, consistently result in a decrease in dose coverage compared to the treatment plan.^{66,67} Nath *et al.* studied the simulated dosimetric impact due to needle splaying. For an unbiased uniform sampling of the insertion angle with 5 degree standard deviation, the minimum target dose decreased by 8 % and the V_{100} dose coverage decreased by 1 %. Meyer *et al.* investigated the seed misplacement immediately after implantation using C-arm fluoroscopy and estimated a mean post-implant D_{90} value of 152 Gy compared to an ideal value of 194 Gy on the intra-operative treatment plan.⁶⁸

PPB implantation is performed manually and delivery accuracy is strongly influenced by the individual practitioner.⁴ Experience, both in brachytherapy and the specific procedure employed, also factors into the ability to deliver the planned dose as closely as possible and is often referred to as a learning curve.⁶¹ The discrepancy between the planned and delivered doses improves with experience, but significant differences remain even for very experienced practitioners.

2.7.3 Post-implant evaluation

The uncertainty in delineating the prostate on CT, due to low soft tissue contrast coupled with seed implant artifacts, has a strong effect on post-implant dosimetry.⁴ Lee *et al.* reported inter-observer variation in D_{90} and V_{100} values sufficient to influence the outcome of clinical evaluation (i.e. acceptable or unacceptable).⁶⁹ In addition, the

tendency to overestimate the prostate spatial extent results in a systematically lower determination of the dose coverage. Crook *et al.* reported prostate D_{90} values 10 to 20 Gy higher for evaluation using MR-CT fusion compared to CT alone.⁷⁰

Localization of the implant is accurate on CT with sub-millimeter accuracy in the axial plane. The uncertainty in the SI direction is larger due to the scanning slice thickness but the influence on post-implant dosimetry is insignificant compared to the contribution of contouring uncertainty.⁷¹ However, determination of the seed orientation is relevant for TG-43 dose calculations using the 2-D formalism. Lindsay *et al.* reported observable differences in the dose distribution due to seed anisotropy, reflecting the high dose gradient of the seed distribution.⁷² The impacts on prostate DVH and dosimetric quantities are much smaller due to the loss of spatial information. Chng *et al.* inferred the seed orientation based on the reconstructed trajectory of stranded implants.⁵¹ The difference in prostate D_{90} was 2 Gy compared to the 1-D formalism.⁷³ On the other hand, OAR dosimetry is sensitive to localization and orientation uncertainties, specifically for nearby implanted seeds.

During US imaging for treatment planning and seed delivery, probe contact pressure displaces and deforms the prostate. Hence seeds are planned for and delivered to the prostate under probe compression. After implantation, the probe is removed and post-implant dosimetry is performed for an uncompressed prostate. Prostate shape differences reflecting probe-induced deformation have been reported.⁴¹ Literature concerning the probe-induced effects on post-implant dosimetry is limited, probably due to the small potential effects that are expected from this phenomenon.

The post-implant study represents the implanted prostate at the time of image acquisition. The current methodology of dose calculation and evaluation assumes that the spatial relationship between the prostate and the implanted seeds is static over time. However, in reality the dose is delivered to the prostate over the radioactive lifetime of the sources, in the order of months. Relative movement of the seeds and prostate due to prostate edema,

seed migration, and natural physiological changes (i.e. rectal filling) can result in deviations from reported post-implant dosimetry.

The prostate volume reaches a maximum after implantation due to edema and gradually decreases monotonically over time.²⁸ The implanted seeds are assumed to move congruently with the internal prostate tissue, affecting the inter-seed distance. The reported ETV dosimetry is lowest at peak edema and gradually increases with edema resolution as the seeds move closer in distance. Based on reported edema from serial CT imaging, Chen *et al.* reported an average dose underestimation by 20 % for post-implant dosimetry performed at peak edema.⁷⁴ Dosimetry performed after edema resolution (i.e. close to one month after implantation) and during treatment planning does not account for swelling and overestimates the dose by roughly 6 %.⁷⁵ However, reported edema parameters vary widely in the literature. Sloboda *et al.* reported smaller edema magnitude and a different resolution dynamic.²⁸ The underestimation at peak edema was calculated to be much smaller at 10 %. Dosimetric effects due to edema are greater for Pd-103, which has a shorter radioactive half-life.

Seed migration results in further deviation from the planned implant and generally degrades the delivered dosimetry. The movement, if significant, can result in large dosimetric effects but is difficult to isolate from other factors (i.e. edema and prostate changes). McLaughlin *et al.* reported significant inferior shift in a number of strands using MR-CT fusion that resulted in 40 Gy reduction of prostate D₉₀ between day 0 and day 14.³² Strong negative consequences for rectal dosimetry are also reported. On the other hand, Usmani *et al.* reported average migrations between day 0 and 30 of only 0.41 mm (95% CI: 0.03 to 0.79 mm) in the SI direction, 0.22 mm (0.08 to 0.37 mm) in the lateral direction, and 0.22 mm (-0.06 to 0.51 mm) in the AP direction.³⁸ Dosimetric results were not reported, but the effects would likely be insignificant within the context of CT contouring uncertainty.

2.8 References

- 1 S. Leighton, <http://www.harvardprostateknowledge.org/>, retrieved Jun 10, 2014.
- 2 A. Tewari, *Prostate Cancer: A Comprehensive Perspective*, 1st ed. (Springer, London, 2013).
- 3 S. Standring, N.R. Borley, P. Collins, A.R. Crossman, M.A. Gatzoulis, J.C. Healy, D. Johnson, V. Mahadevan, R.L. Newell, C.B. Wigley, *Gray's Anatomy*, 40th ed. (Churchill Livingstone/Elsevier, Edinburgh, 2008).
- 4 Y. Yu, L.L. Anderson, Z. Li, D.E. Mellenberg, R. Nath, M.C. Schell, F.M. Waterman, A. Wu, J.C. Blasko, "Permanent prostate seed implant brachytherapy: report of the American Association of Physicists in Medicine Task Group No. 64." *Med. Phys.* **26**, 2054-2076 (1999).
- 5 Image from B&K Medical, <http://www.analogicultrasound.com/>, retrieved May 14, 2014.
- 6 Image from Civco Medical Solutions, <http://www.civco.com/mmi/products/brachytherapy.htm>, retrieved May 14, 2014.
- 7 G.S. Merrick, W.M. Butler, K.E. Wallner, J.C. Blasko, J. Michalski, J. Aronowitz, P. Grimm, B.J. Moran, P.W. McLaughlin, J. Usher, J.H. Lief, Z.A. Allen, "Variability of prostate brachytherapy pre-implant dosimetry: a multi-institutional analysis." *Brachytherapy* **4**, 241-251 (2005).
- 8 R. Nath, W.S. Bice, W.M. Butler, Z. Chen, A.S. Meigooni, V. Narayana, M.J. Rivard, Y. Yu, American Association of Physicists in Medicine, "AAPM recommendations on dose prescription and reporting methods for permanent interstitial brachytherapy for prostate cancer: report of Task Group 137." *Med. Phys.* **36**, 5310-5322 (2009).
- 9 C. Salembier, P. Lavagnini, P. Nickers, P. Mangili, A. Rijnders, A. Polo, J. Venselaar, P. Hoskin, G.E.C.E.P. Group, "Tumour and target volumes in permanent prostate

- brachytherapy: a supplement to the ESTRO/EAU/EORTC recommendations on prostate brachytherapy." *Radiother. Oncol.* **83**, 3-10 (2007).
- 10 B.J. Davis, E.M. Horwitz, W.R. Lee, J.M. Crook, R.G. Stock, G.S. Merrick, W.M. Butler, P.D. Grimm, N.N. Stone, L. Potters, A.L. Zietman, M.J. Zelefsky, A.B. Society, "American Brachytherapy Society consensus guidelines for transrectal ultrasound-guided permanent prostate brachytherapy." *Brachytherapy* **11**, 6-19 (2012).
- 11 R.S. Sloboda, J.E. Pedersen, J. Hanson, R.M. Halperin, "Dosimetric consequences of increased seed strength for I-125 prostate implants." *Radiother. Oncol.* **68**, 295-297 (2003).
- 12 R. Nath, L.L. Anderson, G. Luxton, K.A. Weaver, J.F. Williamson, A.S. Meigooni, "Dosimetry of interstitial brachytherapy sources: recommendations of the AAPM Radiation Therapy Committee Task Group No. 43. American Association of Physicists in Medicine." *Med. Phys.* **22**, 209-234 (1995).
- 13 S. Nag, D. Beyer, J. Friedland, P. Grimm, R. Nath, "American Brachytherapy Society (ABS) recommendations for transperineal permanent brachytherapy of prostate cancer." *Int. J. Radiat. Oncol. Biol. Phys.* **44**, 789-799 (1999).
- 14 R.G. Stock, N.N. Stone, A. Tabert, C. Iannuzzi, J.K. DeWyngaert, "A dose-response study for I-125 prostate implants." *Int. J. Radiat. Oncol. Biol. Phys.* **41**, 101-108 (1998).
- 15 M.J. Zelefsky and W.F. Whitmore, "Long-term results of retropubic permanent 125iodine implantation of the prostate for clinically localized prostatic cancer." *J. Urol.* **158** (1997).
- 16 L. Potters, Y. Cao, E. Calugaru, T. Torre, P. Fearn, X.H. Wang, "A comprehensive review of CT-based dosimetry parameters and biochemical control in patients treated with permanent prostate brachytherapy." *Int. J. Radiat. Oncol. Biol. Phys.* **50**, 605-614 (2001).

- 17 N. Usmani, K. Martell, S. Ghosh, H. Moore, N. Pervez, J. Pedersen, D. Yee, A. Murtha, J. Amanie, R. Sloboda, "Comparison of low and intermediate source strengths for (125)I prostate brachytherapy implants." *Brachytherapy* **12**, 442-448 (2013).
- 18 W.M. Butler, G.S. Merrick, J.H. Lief, A.T. Dorsey, "Comparison of seed loading approaches in prostate brachytherapy." *Med. Phys.* **27**, 381-392 (2000).
- 19 L. Beaulieu, L. Archambault, S. Aubin, E. Oral, R. Taschereau, J. Pouliot, "The robustness of dose distributions to displacement and migration of 125I permanent seed implants over a wide range of seed number, activity, and designs." *Int. J. Radiat. Oncol. Biol. Phys.* **58**, 1298-1308 (2004).
- 20 J. Pouliot, D. Tremblay, J. Roy, S. Filice, "Optimization of permanent 125I prostate implants using fast simulated annealing." *Int. J. Radiat. Oncol. Biol. Phys.* **36**, 711-720 (1996).
- 21 S. Nag, J.P. Ciezki, R. Cormack, S. Doggett, K. DeWynngaert, G.K. Edmundson, R.G. Stock, N.N. Stone, Y. Yu, M.J. Zelefsky, Clinical Research Committee, American Brachytherapy Society, "Intraoperative planning and evaluation of permanent prostate brachytherapy: report of the American Brachytherapy Society." *Int. J. Radiat. Oncol. Biol. Phys.* **51**, 1422-1430 (2001).
- 22 L. Beaulieu, S. Aubin, R. Taschereau, J. Pouliot, E. Vigneault, "Dosimetric impact of the variation of the prostate volume and shape between pretreatment planning and treatment procedure." *Int. J. Radiat. Oncol. Biol. Phys.* **53**, 215-221 (2002).
- 23 D.A. Wilkinson, E.J. Lee, J.P. Ciezki, D.S. Mohan, C. Zippe, K. Angermeier, J. Ulchaker, E.A. Klein, D. Mohan, "Dosimetric comparison of pre-planned and OR-planned prostate seed brachytherapy." *Int. J. Radiat. Oncol. Biol. Phys.* **48**, 1241-1244 (2000).

- 24 M.J. Zelefsky and M. Zaider, "Low-dose-rate brachytherapy for prostate cancer: preplanning vs. intraoperative planning-intraoperative planning is best." *Brachytherapy* **5**, 143-4; discussion 146 (2006).
- 25 J.C. Blasko, "Low-dose-rate brachytherapy for prostate cancer: preplanning vs. intraoperative planning-preplanning is best." *Brachytherapy* **5**, 139-42 (2006).
- 26 R. Nath, L.L. Anderson, J.A. Meli, A.J. Olch, J.A. Stitt, J.F. Williamson, "Code of practice for brachytherapy physics: report of the AAPM Radiation Therapy Committee Task Group No. 56. American Association of Physicists in Medicine." *Med. Phys.* **24**, 1557-1598 (1997).
- 27 D.R. Evans, T. Meyer, S. Angyalfi, S. Husain, I. Kay, P. Dunscombe, "Enhanced efficiency and ergonomics of an intraoperative automated prostate brachytherapy delivery technique." *Brachytherapy* **6**, 254-257 (2007).
- 28 R.S. Sloboda, N. Usmani, J. Pedersen, A. Murtha, N. Pervez, D. Yee, "Time course of prostatic edema post permanent seed implant determined by magnetic resonance imaging." *Brachytherapy* **9**, 354-361 (2010).
- 29 F.M. Waterman, N. Yue, B.W. Corn, A.P. Dicker, "Edema associated with I-125 or Pd-103 prostate brachytherapy and its impact on post-implant dosimetry: an analysis based on serial CT acquisition." *Int. J. Radiat. Oncol. Biol. Phys.* **41**, 1069-1077 (1998).
- 30 C. Chira, G. Delouya, S. Larrivée, J. Carrier, D. Taussky, "Prostate volume changes during permanent seed brachytherapy: an analysis of intra-operative variations, predictive factors and clinical implication." *Radiat Oncol* **8** (2013).
- 31 A. Sugawara, J. Nakashima, E. Kunieda, H. Nagata, R. Mizuno, S. Seki, Y. Shiraishi, R. Kouta, M. Oya, N. Shigematsu, "Incidence of seed migration to the chest, abdomen, and pelvis after transperineal interstitial prostate brachytherapy with loose (125)I seeds." *Radiat Oncol* **6** (2011).

- 32 P. McLaughlin, V. Narayana, C. Pan, S. Berri, S. Troyer, J. Herman, V. Evans, P. Roberson, "Comparison of day 0 and day 14 dosimetry for permanent prostate implants using stranded seeds." *Int. J. Radiat. Oncol. Biol. Phys.* **64**, 144-150 (2006).
- 33 B. Al-Qaisieh, B. Carey, D. Ash, D. Bottomley, "The use of linked seeds eliminates lung embolization following permanent seed implantation for prostate cancer." *Int. J. Radiat. Oncol. Biol. Phys.* **59**, 397-399 (2004).
- 34 G.S. Merrick, W.M. Butler, A.T. Dorsey, J.H. Lief, M.L. Benson, "Seed fixity in the prostate/periprostatic region following brachytherapy." *Int. J. Radiat. Oncol. Biol. Phys.* **46**, 215-220 (2000).
- 35 J. Crook, "Commentary on "a comparison of the precision of seeds deposited as loose seeds vs. suture-embedded seeds: a randomized trial" and "prostate brachytherapy seed migration and dosimetry: analysis of stranded sources and other potential predictive factors": to strand or not to strand--is this really the question?" *Brachytherapy* **3**, 20-21 (2004).
- 36 D. Taussky, C. Moumdjian, R. Larouche, D. Béliveau-Nadeau, C. Boudreau, Y. Hervieux, D. Donath, "Seed migration in prostate brachytherapy depends on experience and technique." *Brachytherapy* **11**, 452-456 (2012).
- 37 N.N. Stone and R.G. Stock, "Reduction of pulmonary migration of permanent interstitial sources in patients undergoing prostate brachytherapy." *Urology* **66**, 119-123 (2005).
- 38 N. Usmani, N. Chng, I. Spadinger, W.J. Morris, "Lack of significant intraprostatic migration of stranded iodine-125 sources in prostate brachytherapy implants." *Brachytherapy* **10**, 275-285 (2011).
- 39 P.W. McLaughlin, C. Evans, M. Feng, V. Narayana, "Radiographic and anatomic basis for prostate contouring errors and methods to improve prostate contouring accuracy." *Int. J. Radiat. Oncol. Biol. Phys.* **76**, 369-378 (2010).

- 40 V. Narayana, P.L. Roberson, R.J. Winfield, P.W. McLaughlin, "Impact of ultrasound and computed tomography prostate volume registration on evaluation of permanent prostate implants." *Int. J. Radiat. Oncol. Biol. Phys.* **39**, 341-346 (1997).
- 41 W.L. Smith, C. Lewis, G. Bauman, G. Rodrigues, D. D'Souza, R. Ash, D. Ho, V. Venkatesan, D. Downey, A. Fenster, "Prostate volume contouring: a 3D analysis of segmentation using 3DTRUS, CT, and MR." *Int. J. Radiat. Oncol. Biol. Phys.* **67**, 1238-1247 (2007).
- 42 M.C. Solhjem, B.J. Davis, T.M. Pisansky, T.M. Wilson, L.A. Mynderse, M.G. Herman, B.F. King, S.M. Geyer, "Prostate volume measurement by transrectal ultrasound and computed tomography before and after permanent prostate brachytherapy." *Int. J. Radiat. Oncol. Biol. Phys.* **60**, 767-776 (2004).
- 43 K. Wachowicz, S.D. Thomas, B.G. Fallone, "Characterization of the susceptibility artifact around a prostate brachytherapy seed in MRI." *Med. Phys.* **33**, 4459-4467 (2006).
- 44 A.K.H. Robertson, P.S. Basran, S.D. Thomas, D. Wells, "CT, MR, and ultrasound image artifacts from prostate brachytherapy seed implants: the impact of seed size." *Med. Phys.* **39**, 2061-2068 (2012).
- 45 M.A. Moerland, H.K. Wijrdeman, R. Beersma, C.J. Bakker, J.J. Battermann, "Evaluation of permanent I-125 prostate implants using radiography and magnetic resonance imaging." *Int. J. Radiat. Oncol. Biol. Phys.* **37**, 927-933 (1997).
- 46 E. Dehghan, J. Lee, P. Fallavollita, N. Kuo, A. Deguet, Y. Le, E.C. Burdette, D.Y. Song, J.L. Prince, G. Fichtinger, "Ultrasound-fluoroscopy registration for prostate brachytherapy dosimetry." *Med. Image Anal.* **16**, 1347-1358 (2012).
- 47 M. Moradi, S.S. Mahdavi, E. Dehghan, J.R. Lobo, S. Deshmukh, W.J. Morris, G. Fichtinger, S.T.E. Salcudean, "Seed localization in ultrasound and registration to C-arm

- fluoroscopy using matched needle tracks for prostate brachytherapy." *IEEE Trans. Biomed. Eng.* **59**, 2558-2567 (2012).
- 48 P. Fallavollita, Z.K. Aghaloo, E.C. Burdette, D.Y. Song, P. Abolmaesumi, G. Fichtinger, "Registration between ultrasound and fluoroscopy or CT in prostate brachytherapy." *Med. Phys.* **37**, 2749-2760 (2010).
- 49 B.H. Han, K. Wallner, G. Merrick, W. Butler, S. Sutlief, J. Sylvester, "Prostate brachytherapy seed identification on post-implant TRUS images." *Med. Phys.* **30**, 898-900 (2003).
- 50 M.J. Rivard, B.M. Coursey, L.A. DeWerd, W.F. Hanson, M.S. Huq, G.S. Ibbott, M.G. Mitch, R. Nath, J.F. Williamson, "Update of AAPM Task Group No. 43 Report: A revised AAPM protocol for brachytherapy dose calculations." *Med. Phys.* **31**, 633-674 (2004).
- 51 N. Chng, I. Spadinger, W.J. Morris, N. Usmani, S. Salcudean, "Prostate brachytherapy postimplant dosimetry: automatic plan reconstruction of stranded implants." *Med. Phys.* **38**, 327-342 (2011).
- 52 M.J. Rivard, J.L.M. Venselaar, L. Beaulieu, "The evolution of brachytherapy treatment planning." *Med. Phys.* **36**, 2136-2153 (2009).
- 53 J. Carrier, L. Beaulieu, F. Therriault-Proulx, R. Roy, "Impact of interseed attenuation and tissue composition for permanent prostate implants." *Med. Phys.* **33**, 595-604 (2006).
- 54 H. Afsharpour, G. Landry, M. D'Amours, S. Enger, B. Reniers, E. Poon, J. Carrier, F. Verhaegen, L. Beaulieu, "ALGEBRA: ALgorithm for the heterogeneous dosimetry based on GEANT4 for BRACHytherapy." *Phys. Med. Biol.* **57**, 3273-3280 (2012).
- 55 R.E.P. Taylor, G. Yegin, D.W.O. Rogers, "Benchmarking brachydose: Voxel based EGSnrc Monte Carlo calculations of TG-43 dosimetry parameters." *Med. Phys.* **34**, 445-457 (2007).

- 56 E. Poon, Y. Le, J.F. Williamson, F. Verhaegen, "BrachyGUI: an adjunct to an accelerated Monte Carlo photon transport code for patient-specific brachytherapy dose calculations and analysis," *J Phys: Conf Ser* **102** (2008).
- 57 O. Chibani and J.F. Williamson, "MCPI: a sub-minute Monte Carlo dose calculation engine for prostate implants." *Med. Phys.* **32**, 3688-3698 (2005).
- 58 K.A. Gifford, J.L. Horton, T.A. Wareing, G. Failla, F. Mourtada, "Comparison of a finite-element multigroup discrete-ordinates code with Monte Carlo for radiotherapy calculations." *Phys. Med. Biol.* **51**, 2253-2265 (2006).
- 59 K.A. Gifford, M.J. Price, J.L. Horton, T.A. Wareing, F. Mourtada, "Optimization of deterministic transport parameters for the calculation of the dose distribution around a high dose-rate ¹⁹²Ir brachytherapy source." *Med. Phys.* **35**, 2279-2285 (2008).
- 60 B. Al-Qaisieh, T. Witteveen, B. Carey, A. Henry, D. Bottomley, J. Smith, K. Franks, P. Bownes, "Correlation between pre- and postimplant dosimetry for iodine-125 seed implants for localized prostate cancer." *Int. J. Radiat. Oncol. Biol. Phys.* **75**, 626-630 (2009).
- 61 L. Beaulieu, D.R. Evans, S. Aubin, S. Angyalfi, S. Husain, I. Kay, A. Martin, N. Varfalvy, E. Vigneault, P. Dunscombe, "Bypassing the learning curve in permanent seed implants using state-of-the-art technology." *Int. J. Radiat. Oncol. Biol. Phys.* **67**, 71-77 (2007).
- 62 N. Abolhassani, R. Patel, M. Moallem, "Needle insertion into soft tissue: a survey." *Med. Eng. Phys.* **29**, 413-431 (2007).
- 63 P.L. Roberson, V. Narayana, D.L. McShan, R.J. Winfield, P.W. McLaughlin, "Source placement error for permanent implant of the prostate." *Med. Phys.* **24**, 251-257 (1997).

- 64 R. Taschereau, J. Pouliot, J. Roy, D. Tremblay, "Seed misplacement and stabilizing needles in transperineal permanent prostate implants." *Radiother. Oncol.* **55**, 59-63 (2000).
- 65 G. Wan, Z. Wei, L. Gardi, D.B. Downey, A. Fenster, "Brachytherapy needle deflection evaluation and correction." *Med. Phys.* **32**, 902-909 (2005).
- 66 J.E. Dawson, T. Wu, T. Roy, J.Y. Gu, H. Kim, "Dose effects of seeds placement deviations from pre-planned positions in ultrasound guided prostate implants." *Radiother. Oncol.* **32**, 268-270 (1994).
- 67 S. Nath, Z. Chen, N. Yue, S. Trumppore, R. Peschel, "Dosimetric effects of needle divergence in prostate seed implant using 125I and 103Pd radioactive seeds." *Med. Phys.* **27**, 1058-1066 (2000).
- 68 T. Meyer, *Dosimetric Impact of Implant Uncertainties in Prostate Brachytherapy* (Doctoral thesis, University of Calgary, 2010).
- 69 W.R. Lee, M. Roach, J. Michalski, B. Moran, D. Beyer, "Interobserver variability leads to significant differences in quantifiers of prostate implant adequacy." *Int. J. Radiat. Oncol. Biol. Phys.* **54**, 457-461 (2002).
- 70 J. Crook, M. Milosevic, P. Catton, I. Yeung, T. Haycocks, T. Tran, C. Catton, M. McLean, T. Panzarella, M.A. Haider, "Interobserver variation in postimplant computed tomography contouring affects quality assessment of prostate brachytherapy." *Brachytherapy* **1**, 66-73 (2002).
- 71 D. Tubic and L. Beaulieu, "Sliding slice: a novel approach for high accuracy and automatic 3D localization of seeds from CT scans." *Med. Phys.* **32**, 163-174 (2005).
- 72 P. Lindsay, J. Battista, J.V. Dyk, "The effect of seed anisotropy on brachytherapy dose distributions using 125I and 103Pd." *Med. Phys.* **28**, 336-345 (2001).

- 73 N. Chng, I. Spadinger, R. Rasoda, W.J. Morris, S. Salcudean, "Prostate brachytherapy postimplant dosimetry: seed orientation and the impact of dosimetric anisotropy in stranded implants." *Med. Phys.* **39**, 721-731 (2012).
- 74 Z. Chen, N. Yue, X. Wang, K.B. Roberts, R. Peschel, R. Nath, "Dosimetric effects of edema in permanent prostate seed implants: a rigorous solution." *Int. J. Radiat. Oncol. Biol. Phys.* **47**, 1405-1419 (2000).
- 75 N. Yue, Z. Chen, R. Peschel, A.P. Dicker, F.M. Waterman, R. Nath, "Optimum timing for image-based dose evaluation of 125I and 103PD prostate seed implants." *Int. J. Radiat. Oncol. Biol. Phys.* **45**, 1063-1072 (1999).

Chapter 3 Comparison of pre-implant prostate contoured from magnetic resonance and transrectal ultrasound imaging

3.1 Introduction

PPB treatment planning aims to tailor a planned dose distribution which is highly localized and conformal to the target volume. The CTV and PTV are derived from the prostate contour by the addition of a non-uniform margin. As such, accurate prostate delineation is essential to ensure proper target coverage and dose sparing of surrounding normal tissue and OARs. The ABS recommends the use of TRUS imaging for the pre-implant planning study.¹

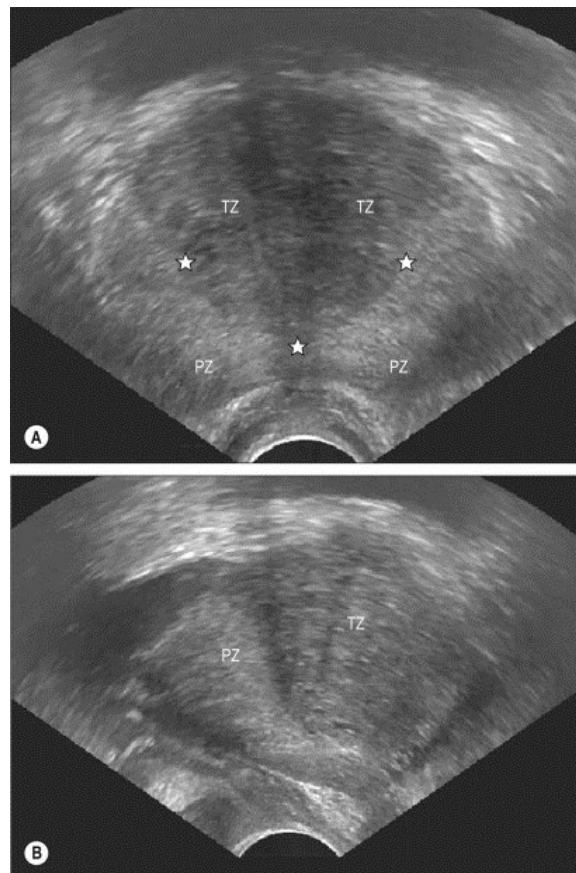


Figure 3.1: Ultrasound imaging of the prostate.² (A) Axial view showing the transition zone (TZ) and the peripheral zone (PZ). The interface between the zones is marked (*). (B) Sagittal view.

Soft-tissue contrast is particularly important during imaging in order to differentiate the prostate from the surrounding anatomy.³ The seminal vesicles are located at the posterior base. The rectum runs roughly parallel along the posterior aspect of the prostate gland. In particular, contouring uncertainty is greater at the prostate-bladder interface in the base and at the genitourinary diaphragm in the apex. Although difficult to interpret to the inexperienced observer, the prostate and its zonal regions are readily discernible on US to the trained physician, as illustrated in Figure 3.1. However, US images contain a noticeable amount of noise which can negatively impact contouring accuracy.

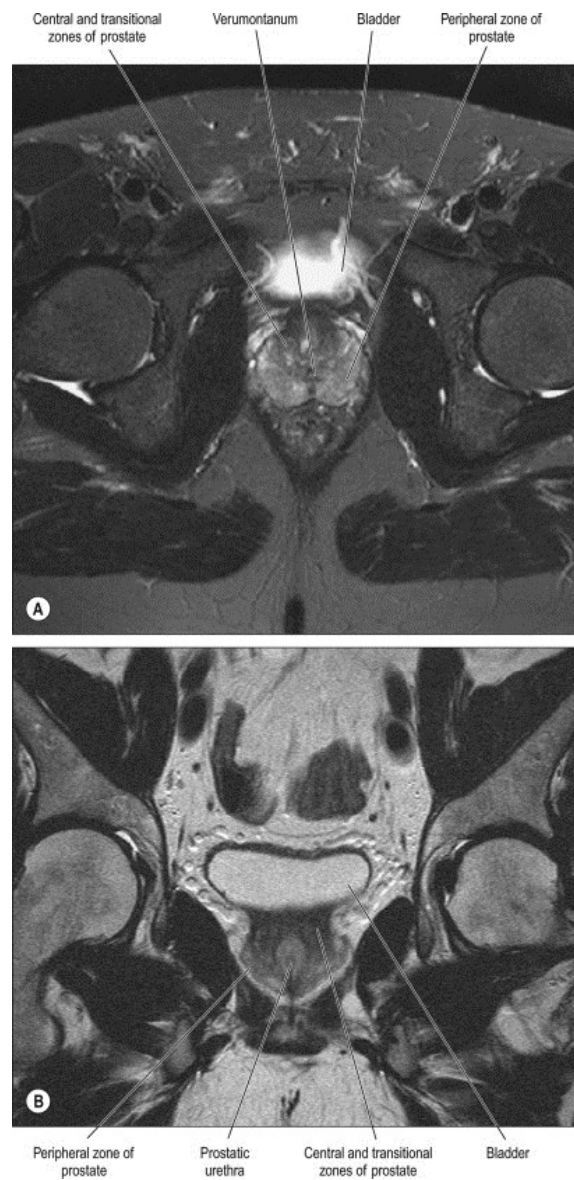


Figure 3.2: T2-weighted magnetic resonance image of the prostate.² (A) Axial and (B) coronal views showing the zonal anatomy.

MR imaging, already an established modality in diagnostic radiology, is emerging as a useful tool in brachytherapy due to its superior soft-tissue contrast, with the internal prostate structure clearly visible (Figure 3.2). There are numerous studies showing the superior prostate delineation of MR compared to CT in terms of accuracy³⁻⁵ and variability^{6,7}. Use of the MR-delineated prostate in MR-CT fusion has significantly improved PPB post-implant dosimetry.⁸⁻¹⁰ The AAPM recommends the supplementary use of MR for post-implant evaluation when available.¹¹ An additional advantage of MR is the ability to perform direct registration of anatomical MR images with functional MR images that are potentially useful in identifying tumors within the prostate¹²⁻¹⁴, thus creating opportunities for targeted prostate therapy.^{15,16}

In the hopes of improving treatment planning and implant delivery, various studies have investigated the feasibility of supplementing or complementing US with MR imaging during the planning and intra-operative stages.¹⁷⁻¹⁹ However, any potential gain from MR imaging depends on the prostate delineation accuracy and variability compared to US. Furthermore, the prostate shapes as imaged on MR and US differ due to patient positioning (supine and lithotomy positions, respectively) and the presence of the TRUS probe. This may lead to discrepancies between the prostate during planning and implantation.

This investigation attempts to ascertain whether prostate delineation accuracy in PPB treatment planning can be improved with the use of MR imaging. In addition, potential differences in prostate shape due to the TRUS probe are explored. The objective of this study is to quantify the differences in pre-implant prostate contours between MR and US imaging with regards to i) volume and shape, ii) inter-observer contouring variability, and iii) intra-observer contouring variability.

3.2 Methods and materials

3.2.1 Patients and Imaging

Number of patients	23	
Median age (yrs)	62	(range: 51 – 76)
Median pretreatment PSA (ng/mL)	5.2	(range: 2.0 – 14.0)
Gleason score:		
≤ 5	1	(4 %)
6	20	(87 %)
7	2	(9 %)
Clinical stage:		
T1c	17	(74 %)
T2a	3	(13 %)
T2b	3	(13 %)
Risk group:		
Low risk	15	(65 %)
Intermediate risk	8	(35 %)

Table 3.1: Baseline characteristics of patient population.

The study, approved by the local research ethics board, enrolled patients who were treated with I-125 brachytherapy for localized prostate cancer. The same patients also participated in a prior study by Usmani *et al.*⁶ Of the 40 patients initially enrolled, 17 were excluded due to the presence of pre-existing contours, drawn by the US operator, which were incorporated into the US image itself and could not be easily removed. The characteristics of the remaining 23 patients are summarized in Table 3.1. Each consenting patient had a pre-treatment planning scan on US, followed by an MR scan 4 to 6 weeks afterwards, just prior to the implant procedure. Patients on ADT were excluded from the study. Patients were instructed to have a comfortably full bladder and empty rectum before each scan.

The MR scans were acquired using a 1.5 T Gyroscan Intera imager (Philips Healthcare, Andover, MA) with a 5-channel cardiac coil. The axial slice thickness was 3 (2 patients) or 4 mm (21 patients) with no inter-slice gap. A T2-weighted fast spin-echo (echo time/repetition time in milliseconds: 90/2500) pulse sequence was used for optimal definition of the prostate boundary.⁹ An under-knee rest was used to maintain consistency in pelvic orientation.

US imaging was performed using a Sonoline Adara scanner with an Endo PII probe (Siemens Medical Solutions USA Inc., Malvern, PA). The superior-most extent of the prostate was first determined on a mid-sagittal image. The probe was extended superior to that point and sub-mm retractions were made until the prostate base was visible on axial imaging. 5 mm axial images of the prostate were subsequently captured starting from the base through the entire length of the prostate.

3.2.2 Contouring

The MR and US images were imported into the VariSeed TPS for contouring. Prior to contours being drawn, a contouring workshop was attended by all of the radiation oncologists participating in this study to facilitate consistent contouring. A radiologist experienced in prostate MR imaging reviewed the prostate anatomy and the oncologists completed the prostate atlas and contouring modules on www.prostadoodle.com.

The collection of images was anonymized and randomized to avoid any contouring bias that could have arisen from complementary information between modalities. The prostate was contoured by five radiation oncologists experienced in prostate brachytherapy (N.U., J.P., N.P., D.Y., B.D.). Images were replicated such that each replica image was only contoured once by each observer. The volume and shape analysis was done using the contours from one physician (N.U.). Contours for all five observers were used for the inter-observer variability analysis. Of the original 40 patients, 11 were selected for intra-observer variability analysis. The pre-existing US contours reduced the intra-observer US sample size to 6 patients (MR sample size was 11 patients). To limit recall bias, patients were contoured at least two weeks apart.

3.2.3 Volume and shape

Pair-wise contouring differences between MR and US were calculated in terms of the prostate volume and dimensions (width, height, length). The planimetry volume was calculated by summing the contoured area on each slice multiplied by the slice thickness.²⁰ The width and height were defined as the largest lateral and AP extents on

any slice. The length or SI extent was defined as the number of contour slices multiplied by the slice thickness.⁷

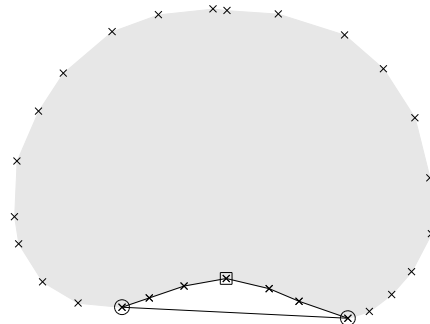


Figure 3.3: A prostate contour (grey) generated from contour points (x). The indentation (closed lines) was identified by the concave posterior edge, where the sides (circles) were lower than the center (square).

During US image acquisition, pressure from the TRUS probe may be sufficient to deform the posterior region of the prostate.⁷ On MR images, the deformation may be due to pressure from rectal filling. To quantify posterior prostate deformation, concave indentations were identified (Figure 3.3) and quantified in terms of their height and volume. The indentation height was defined as the maximum AP extent, over all slices in a set, of a vertical line extending from the central indentation point (square) to the line connecting the side points (circle). The indentation volume was calculated as the sum of the indentation areas over all slices multiplied by the slice thickness. To test whether rectal pressure correlates with MR prostate deformation, the amount of rectal filling on MR images was measured by calculating the anterior-posterior extent of the inner rectal wall at the mid-gland slice.

3.2.4 Contour variability

For each imaging modality, the inter- and intra-observer variability were quantified in terms of the prostate volume, dimensions, and Jaccard index (defined below). The variability in volume and dimensions was defined as the standard deviation obtained from a set of contours for a patient, averaged over the patient population.⁶ For the inter-observer variability, the standard deviation was calculated over the set of contours drawn by the five observers. For the intra-observer variability, the standard deviation was

calculated over the two repeated contours by the same observer, then averaged over the five observers.

The prostate volume is a necessary but not sufficient indicator of similarity.⁶ It is possible for two contours to have same volume and poor spatial overlap. The Jaccard index, a unitless quantifier of spatial overlap, was used to assess the similarity of contours on individual slices and of the whole prostate volume. Local variations in contouring variability were measured at the base, mid-gland, and apex slices. Given two contours on an image slice, the Jaccard index is defined as their intersection area divided by their union area. An index of zero indicates no overlap between the contours, representing large contouring variability. An index of unity indicates the contours are identical (no variability), occupying the same area on the image.

The Jaccard index was calculated for MR and US separately. For inter-observer variability, the Jaccard index was calculated between each observer contour and a reference contour, chosen as the average contour of all observers to minimize any bias from any individual observer. For the intra-observer variability, the reference contour was the average of the two repeated contours. The Jaccard index for the whole prostate volume was calculated by summing the intersection and union areas over all slices. Because the Jaccard index was calculated between contours drawn on duplicated images, no registration between images was necessary.

3.2.5 Statistical analysis

Unless explicitly stated, the paired Student's t-test was used to test for statistical significance. All tests were two-sided and the p-value threshold for significance was 0.05 (95% confidence level).

3.3 Results

3.3.1 Volume and shape

	<i>Volume</i>	<i>Width</i>	<i>Height</i>	<i>Length</i>
MR	40.1 ± 12.9 mL	48.7 ± 6.1 mm	35.3 ± 4.6 mm	34.0 ± 5.1 mm
US	39.6 ± 12.6 mL	47.5 ± 6.8 mm	34.7 ± 5.2 mm	35.4 ± 5.2 mm
US/MR ratio	0.99 ± 0.08	0.98 ± 0.06	0.99 ± 0.08	1.05 ± 0.14
p-value	0.5	0.09	0.4	0.1

Table 3.2: Mean prostate volume and dimensions calculated from magnetic resonance (MR) and ultrasound (US) images.

Table 3.2 compares the mean prostate volume and dimensions calculated from MR and US images. The mean MR prostate volume for all 23 patients was 40.1 ± 12.9 mL (range: 25.3 – 68.4 mL). The mean paired US/MR volume ratio was 0.99 ± 0.08 (range: 0.81 – 1.18), indicating similar volume determination between the two imaging modalities. The mean ratios for the prostate dimensions were 0.98 ± 0.06 (width), 0.99 ± 0.08 (height), and 1.05 ± 0.14 (length). There was no statistically significant difference between MR- and US-delineated volumes and dimensions. Regression analysis showed no correlation between patient age and prostate volume ($p = 0.2$), US-MR volume difference ($p = 0.7$), nor US/MR volume ratio ($p = 0.8$).

	<i>Indentation height</i>	<i>Indentation volume</i>
MR	0.9 mm (range: 0 – 3.6 mm)	0.13 mL (range: 0 – 1.00 mL)
US	1.7 mm (range: 0 – 4.5 mm)	0.31 mL (range: 0 – 1.36 mL)
US-MR difference	0.8 mm (range: -1.2 – 3.5 mm)	0.18 mL (range: -0.20 – 1.30 mL)
p-value	< 0.01	0.01

Table 3.3: Mean prostate rectal indentation height and volume from magnetic resonance (MR) and ultrasound (US) images.

Table 3.3 lists the prostate indentation height and volume. The mean indentation height and volume were larger on US than MR. The differences were small but statistically significant. Regression analysis showed that the indentation height, as a fraction of the prostate height, correlated with the indentation volume both on MR ($R^2 = 0.4$, $p < 0.01$) and US ($R^2 = 0.7$, $p < 0.01$). Furthermore, there was a positive correlation between the indentation volume and total prostate volume ($R^2 = 0.4$, $p < 0.01$), suggesting that larger prostates experienced more deformation. The MR prostate rectal indentations apparently

were not due to pressure from the rectum as there was no correlation between indentation volume and rectal filling ($R^2 = 0.02$, $p = 0.6$).

3.3.2 Inter-observer contour variability

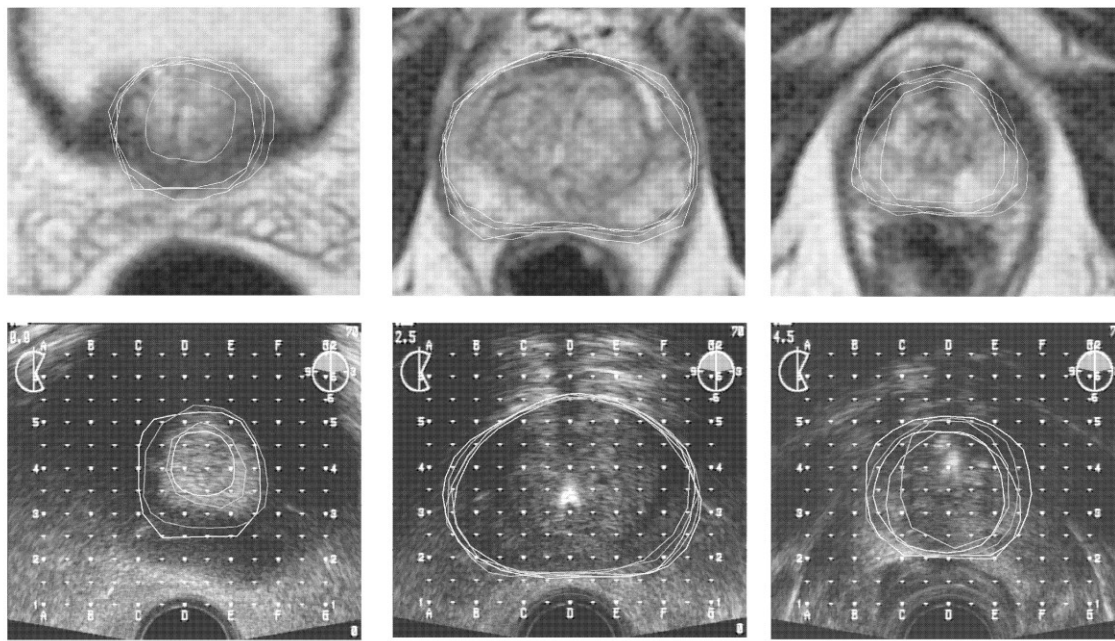


Figure 3.4: Inter-observer contouring variability between 5 observers at the base (left), mid-gland (middle), and apex (right) slices for magnetic resonance (top row) and ultrasound (bottom row) images.

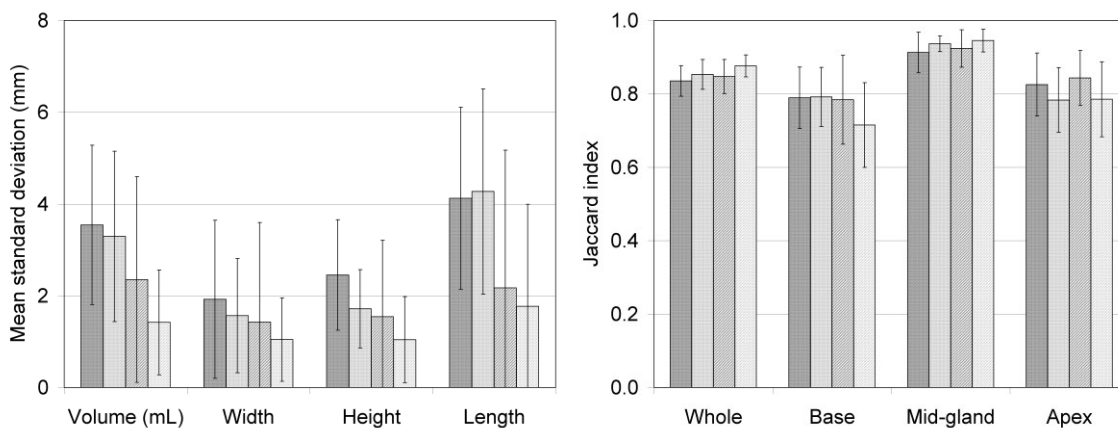


Figure 3.5: Inter- (solid) and intra- (diagonal) observer contour variability for prostate volume and dimensions between magnetic resonance (dark gray) and ultrasound (light gray) contours.

Figure 3.4 illustrates the inter-observer contouring variability at the base, mid-gland, and apex slices for both imaging modalities. Contouring variability is compared separately for

MR and US in terms of volume and dimensions (Figure 3.5 left) and Jaccard indices (Figure 3.5 right). The inter-observer variability in prostate volume was 3.5 ± 1.7 mL on MR and 3.3 ± 1.9 mL on US ($p = 0.6$). The similar volume variability was confirmed by the similar Jaccard index for the prostate volume ($p = 0.2$). Regression analysis showed that the volume variability correlated with prostate volume on US ($R^2 = 0.3$, $p < 0.01$) but not on MR ($p = 0.2$). The variability in prostate height differed at 2.5 ± 1.2 mm on MR and 1.7 ± 0.9 mm on US ($p = 0.02$). The variability in prostate width and length were not significantly different. The Jaccard indices were also similar for the base ($p = 0.9$), mid-gland ($p = 0.08$), and apex slices ($p = 0.1$).

3.3.3 Intra-observer contour variability

The intra-observer variability in prostate volume (Figure 3.5) was smaller on US (1.4 ± 1.1 mL) compared to MR (2.4 ± 2.2 mL). A two-sample t-test indicated the difference was statistically significant ($p = 0.01$). The difference was further confirmed by the Jaccard index for the prostate volume with indices of 0.85 ± 0.05 on MR and 0.88 ± 0.03 on US ($p < 0.01$). The variability in prostate width, height, and length were not significantly different. Although the prostate volume Jaccard index indicated less intra-observer variability on US, individual slices show local differences in contouring variability. MR variability was lower at the base ($p < 0.01$) and apex ($p < 0.01$) slices, while US variability was lower at the mid-gland slice ($p < 0.01$). The larger contributions of the mid-gland areas resulted in higher US Jaccard index values for the whole prostate volume.

The intra-observer variability was generally lower than or comparable to the inter-observer variability. However, the opposite was observed at the base slice. The unpaired two-sample Student's t-test showed the difference to be statistically significant ($p < 0.01$).

3.4 Discussion

3.4.1 Volume and shape

The US/MR prostate volume ratio calculated in this study (0.99 ± 0.08) indicates strong similarity in volume determination between modalities. The result is slightly different

than those previously published. Jeong *et al.* reported a US/MR volume ratio of 1.04 and a similar ratio of 1.05 between US and the actual prostate removed from radical retropubic prostatectomy.²¹ Smith W *et al.* reported a volume ratio of 0.90 ± 0.10 between US and T2-weighted MR imaging of the prostate one month after permanent brachytherapy implantation.⁷ However, the US imaging conditions were somewhat different due to image degradation caused by the implanted seeds partially obscuring the prostate boundary.²²⁻²⁴ Other published comparisons between post-implant MR and pre-implant US volume ratios were potentially confounded by post-implant edema. Moerland *et al.* calculated a ratio of 1.9 ± 0.6 at 3 days post-implant, having obtained the US volume via the ellipsoid volume approximation.²⁵ Using the ellipsoid correction factor reported in the same study, the MR/US volume ratio was estimated at 1.3 ± 0.5 . McLaughlin *et al.* reported a volume ratio of 1.07 ± 0.26 at 2 weeks post-implant, while Taussky *et al.* calculated a median ratio of 1.05 (range: 0.76 – 1.43) at one month post-implant.^{26,27}

During the initial study, the VariSeed TPS reported US volumes 10 % smaller compared to MR. The difference was attributed to the use of different volume reconstruction algorithms depending on imaging modality. Consistent application of the same algorithm resulted in an average volume difference within 1 %. Further study (see Chapter 4) demonstrated that the planimetry algorithm, when applied to contours acquired from TRUS imaging, over-estimates the reported volume. The algorithm was found to be accurate for volume determination from MR contours. Corrected for algorithm bias, the revised US/MR prostate ratio was estimated to be 0.95 (previously 0.99), suggesting a slight under-estimation of the prostate volume on US.

Comparing prostate volumes is a necessary but not sufficient indicator of similarity. However, a spatial overlap comparison between MR and US contours was not undertaken because of differences in patient positioning at the time of imaging. The standard MR bore could not accommodate a patient in the lithotomy position, which was required for TRUS imaging. There were also deformation effects due to the TRUS probe. These differences altered the orientation and shape of the prostate, confounding the use of Jaccard index for quantifying spatial overlap between MR and US prostate pairs.

The US scan was obtained as part of treatment planning for PPB. The MR scan, 4 to 6 weeks afterwards, was scheduled on day 0 prior to implantation and was related to an investigation on prostatic edema time evolution. Although the scans were performed at different times, the prostate volume likely remained constant over time, with the exception of patients undergoing hormone therapy. Hence, patients undergoing ADT to reduce the prostate volume were excluded from the study. Although the prostate shape changed during the time between scans, the volume and contour variability analysis were not affected. It is important to note that even if MR and US scans were performed on the same day, prostate shape differences would remain due to pressure from the US probe.

Prostate volume determination is dependent on imaging slice thickness, which was 5 mm on US and mostly 4 mm on MR. Yang *et al.* reported a systematic decrease in prostate volume with increasing slice thickness on CT.²⁸ For prostates > 30 mL, the discrepancy in volume between 4 mm and 4.8 mm slices was less than 1%. The difference increased to 4% for prostates < 30 mL. These results are consistent with our study where the US volume was 1% smaller than the MR volume (5 of the 23 patients had prostates < 30 mL). In addition, prostate volume can also depend on the slice offset. On US, the starting slice was placed at the base, as determined by the attending oncologist. The slice offset on MR was random. From an ellipsoid model of the prostate, Aarnink *et al.* reported a maximum volume difference of 1% due to varying offset for 4 mm slices.²⁰ Thus, although differences in slice thickness and offset can bias the volume measurement, the effects on the current study are expected to be minimal.

3.4.2 TRUS-induced deformation

The difference in posterior prostate indentation between MR and US served as an estimate of the TRUS probe-induced deformation. The indentation height reflected the deformation at the posterior surface in terms of distance while the indentation volume was related to the amount of tissue displaced. Although the indentation differences were statistically significant, the volume affected was a small fraction of the total prostate volume (maximum of 3%).

Measurements of the probe-induced prostate deformation were likely underestimated. Indentation heights and volumes were calculated assuming the undeformed posterior surface of the prostate was flat. However, Smith W *et al.* showed that the average undeformed prostate, as imaged on MR and CT, is convex.⁷ Moreover, the indentation measurements only accounted for deformations within each axial slice. Ishiyama *et al.* showed how the TRUS probe caused the naturally bending rectum to straighten, which also straightened the prostate along the cranial-caudal direction.²⁹ Probe deformation during pre-planning and implantation may also differ due to application of anesthesia and relaxation of the pelvic muscles.³⁰

3.4.3 Contour variability

Figures 3.5 showed that the intra-observer variability on US was lower in terms of both volume and Jaccard index for the prostate volume and mid-gland slice. On the other hand, local variability was lower on MR at the base and apex slices, suggesting more consistent contouring in regions which are more difficult to delineate. Similar trends were also observed for the inter-observer variability, except at the base slice. However, the differences between MR and US were no longer statistically significant, reflecting variations in contouring style between observers. Thus, any advantage in prostate delineation on MR or US was relatively small compared to inter-observer contouring variability. Nevertheless, given the experience difference in contouring for the two modalities, it is likely that delineation accuracy on MR has significant potential for improvement.

	<i>Volume variability</i>			
	<i>Inter-observer</i>		<i>Intra-observer</i>	
Current study				
MR (pre-implant)	3.5 mL	9.5 %	2.4 mL	6.1 %
US (pre-implant)	3.2 mL	9.3 %	1.4 mL	4.4 %
Smith W (7) *				
MR (1 month post-implant)	4.6 mL		2.7 mL	
US (1 month post-implant)	4.9 mL		3.0 mL	
Smith S (27) **				
US (pre-implant)	1.7 mL	7 %		
US (immediate post-implant)	4.9 mL	13 %		
Xue (29) **				
US (pre-implant)	2.0 mL	8.6 %		
US (immediate post-implant)	4.4 mL	11 %		
Tong (32) *				
US (no implant)	9.6 mL	11.4 %	3.6 mL	5.1 %

Table 3.4: Comparison of published inter- and intra-observer variability in terms of absolute and percentage prostate volume differences.

* variability calculated as the standard error of measurement.

** variability calculated as the median of the standard deviation between contours.

Table 3.4 compares the prostate volume variability with published literature. The current study found similar inter-observer variability in measured pre-implant prostate volumes and smaller US intra-observer variability compared to MR. On the other hand, Smith W *et al.* reported slightly larger variability on post-implant US compared to MR.⁷ The difference could be explained by Smith S *et al.* and Xue *et al.*, who showed that post-implant US images had larger variability compared to pre-implant images.^{22,24} Tong *et al.* observed significantly larger inter- and intra-observer variability in terms of absolute volume.³¹ However, this was likely due to the larger mean prostate volume (69.2 mL) as Smith S *et al.* found the variability to be volume dependent.²² A similar correlation was observed in this study for US but not MR contours.

During US imaging, the position of the prostate base was determined by the attending oncologist. As 5 mm is a significant incremental distance, the US probe was extended superior to the base and retracted in sub-mm increments to ensure that the prostate did not extend beyond the base slice. However, images superior to the base slice were not saved. Thus, the selection of the base slice of the prostate was subsequently fixed for all

observers. This could introduce potential bias in the inter-observer variability values reported for prostate length and, to a lesser extent, volume.

3.4.4 Implications of contour variability

Although the mean US/MR volume ratio was near unity, the ratio for individual patients varied with a standard deviation of 0.08 (range: 0.81 – 1.18), suggesting the possibility of large uncertainty for US contouring accuracy. However, intra-observer variability of the single observer (N.U.) showed that the volume ratios of repeated contours were comparable to US/MR ratios, with standard deviations of 0.12 (range: 0.68 – 1.09) for MR/MR and 0.05 (range: 0.88 – 1.05) for US/US. The equivalent results for all observers were 0.12 (range: 0.66 – 1.29) and 0.07 (range: 0.78 – 1.13), respectively. The two-sample Student's t-test showed no statistical difference between the US/MR and MR/MR ratios ($p = 0.4$) and between the US/MR and US/US ratios ($p = 0.9$). Therefore, volume differences between MR and US, perhaps even in the extreme cases, were most likely due to contouring variability and not to intrinsic differences between the imaging modalities.

Prostate shape change between planning and intra-operative TRUS scans is often cited as justification for intra-operative brachytherapy.^{30,32,33} It is important to note, however, that any potential benefit of intra-operative planning is limited by the reliability of prostate delineation, which is reflected in the contouring variability.³⁴ Furthermore, the existence of non-negligible contouring variability highlights the importance of adding a margin to the prostate to account for this and other inaccuracies that occur during the implant procedure.

The results of the current study suggest that MR and US imaging yield comparable prostate delineated volumes and similar inter-observer contouring variability. Therefore, the use of MR imaging as a substitute for US in prostate brachytherapy is expected to produce similar results. Tanaka *et al.* compared MR and US treatment plans and found no significant differences in prostate dosimetry parameters.¹⁷ The only difference between the plans was the rectum V100, which was attributed to TRUS deformation.

3.5 Conclusion

The study shows that with training and experience, pre-implant prostate delineation on US can be comparable to MR, which has superior imaging quality and soft-tissue contrast. Contours were similar, with no significant difference in volume and dimensions. As shown by the reduced intra-observer variability, MR offers the potential for improved delineation at the prostate base and apex, regions known to be difficult to contour. However, the difference was not observed for the inter-observer variability, which was similar between MR and US. Posterior rectal indentation due to the TRUS probe was observed, though the effects were small. Larger prostates were found to have larger indentations.

3.6 References

- 1 S. Nag, D. Beyer, J. Friedland, P. Grimm, R. Nath, "American Brachytherapy Society (ABS) recommendations for transperineal permanent brachytherapy of prostate cancer." *Int. J. Radiat. Oncol. Biol. Phys.* **44**, 789-799 (1999).
- 2 S. Standring, N.R. Borley, P. Collins, A.R. Crossman, M.A. Gatzoulis, J.C. Healy, D. Johnson, V. Mahadevan, R.L. Newell, C.B. Wigley, *Gray's Anatomy*, 40th ed. (Churchill Livingstone/Elsevier, Edinburgh, 2008).
- 3 P.W. McLaughlin, C. Evans, M. Feng, V. Narayana, "Radiographic and anatomic basis for prostate contouring errors and methods to improve prostate contouring accuracy." *Int. J. Radiat. Oncol. Biol. Phys.* **76**, 369-378 (2010).
- 4 Z. Gao, D. Wilkins, L. Eapen, C. Morash, Y. Wassef, L. Gerig, "A study of prostate delineation referenced against a gold standard created from the visible human data." *Radiother. Oncol.* **85**, 239-246 (2007).
- 5 C. Rasch, I. Barillot, P. Remeijer, A. Touw, M. van Herk, J.V. Lebesque, "Definition of the prostate in CT and MRI: a multi-observer study." *Int. J. Radiat. Oncol. Biol. Phys.* **43**, 57-66 (1999).

- 6 N. Usmani, R. Sloboda, W. Kamal, S. Ghosh, N. Pervez, J. Pedersen, D. Yee, B. Danielson, A. Murtha, J. Amanie, T. Monajemi, "Can images obtained with high field strength magnetic resonance imaging reduce contouring variability of the prostate?" *Int. J. Radiat. Oncol. Biol. Phys.* **80**, 728-734 (2011).
- 7 W.L. Smith, C. Lewis, G. Bauman, G. Rodrigues, D. D'Souza, R. Ash, D. Ho, V. Venkatesan, D. Downey, A. Fenster, "Prostate volume contouring: a 3D analysis of segmentation using 3DTRUS, CT, and MR." *Int. J. Radiat. Oncol. Biol. Phys.* **67**, 1238-1247 (2007).
- 8 A. Polo, F. Cattani, A. Vavassori, D. Origgi, G. Villa, H. Marsiglia, M. Bellomi, G. Tosi, O.D. Cobelli, R. Orecchia, "MR and CT image fusion for postimplant analysis in permanent prostate seed implants." *Int. J. Radiat. Oncol. Biol. Phys.* **60**, 1572-1579 (2004).
- 9 O. Tanaka, S. Hayashi, M. Matsuo, K. Sakurai, M. Nakano, S. Maeda, K. Kajita, T. Deguchi, H. Hoshi, "Comparison of MRI-based and CT/MRI fusion-based postimplant dosimetric analysis of prostate brachytherapy." *Int. J. Radiat. Oncol. Biol. Phys.* **66**, 597-602 (2006).
- 10 J.J. Prete, B.R. Prestidge, W.S. Bice, D.F. Dubois, L.A. Hotchkiss, "Comparison of MRI- and CT-based post-implant dosimetric analysis of transperineal interstitial permanent prostate brachytherapy." *Radiat. Oncol. Investig.* **6**, 90-96 (1998).
- 11 R. Nath, W.S. Bice, W.M. Butler, Z. Chen, A.S. Meigooni, V. Narayana, M.J. Rivard, Y. Yu, American Association of Physicists in Medicine, "AAPM recommendations on dose prescription and reporting methods for permanent interstitial brachytherapy for prostate cancer: report of Task Group 137." *Med. Phys.* **36**, 5310-5322 (2009).
- 12 M. Barkati, S.V. Dyk, F. Foroudi, K. Narayan, "The use of magnetic resonance imaging for image-guided brachytherapy." *J Med Imaging Radiat Oncol* **54**, 137-141 (2010).

- 13 D.M. Somford, J.J. Fütterer, T. Hambroek, J.O. Barentsz, "Diffusion and perfusion MR imaging of the prostate." *Magn. Reson. Imaging Clin. N. Am.* **16**, 685-95 (2008).
- 14 A.P.S. Kirkham, M. Emberton, C. Allen, "How good is MRI at detecting and characterising cancer within the prostate?" *Eur. Urol.* **50**, 1163-74 (2006).
- 15 T.J. Polascik and V. Mouraviev, "Focal therapy for prostate cancer." *Curr. Opin. Urol.* **18**, 269-274 (2008).
- 16 S.E. Eggener, P.T. Scardino, P.R. Carroll, M.J. Zelefsky, O. Sartor, H. Hricak, T.M. Wheeler, S.W. Fine, J. Trachtenberg, M.A. Rubin, M. Ohori, K. Kuroiwa, M. Rossignol, L. Abenham, on Prostate Cancer, International Task Force, the Focal Lesion Paradigm, "Focal therapy for localized prostate cancer: a critical appraisal of rationale and modalities." *J. Urol.* **178**, 2260-2267 (2007).
- 17 O. Tanaka, S. Hayashi, M. Matsuo, M. Nakano, Y. Kubota, S. Maeda, K. Ohtakara, T. Deguchi, H. Hoshi, "MRI-based preplanning in low-dose-rate prostate brachytherapy." *Radiother. Oncol.* **88**, 115-120 (2008).
- 18 M.P.R. Van Gellekom, M.A. Moerland, J.J. Battermann, J.J.W. Lagendijk, "MRI-guided prostate brachytherapy with single needle method--a planning study." *Radiother. Oncol.* **71**, 327-332 (2004).
- 19 A.V. D'Amico, R. Cormack, C.M. Tempany, S. Kumar, G. Topulos, H.M. Kooy, C.N. Coleman, "Real-time magnetic resonance image-guided interstitial brachytherapy in the treatment of select patients with clinically localized prostate cancer." *Int. J. Radiat. Oncol. Biol. Phys.* **42**, 507-515 (1998).
- 20 R.G. Aarnink, R.J. Giesen, de la Rosette, J. J., A.L. Huynen, F.M. Debruyne, H. Wijkstra, "Planimetric volumetry of the prostate: how accurate is it?" *Physiol. Meas.* **16**, 141-150 (1995).

- 21 C.W. Jeong, H.K. Park, S.K. Hong, S. Byun, H.J. Lee, S.E. Lee, "Comparison of prostate volume measured by transrectal ultrasonography and MRI with the actual prostate volume measured after radical prostatectomy." *Urol. Int.* **81**, 179-185 (2008).
- 22 S. Smith, K. Wallner, G. Merrick, W. Butler, S. Sutlief, P. Grimm, "Interpretation of pre- versus postimplant TRUS images." *Med. Phys.* **30**, 920-924 (2003).
- 23 M.C. Solhjem, B.J. Davis, T.M. Pisansky, T.M. Wilson, L.A. Mynderse, M.G. Herman, B.F. King, S.M. Geyer, "Prostate volume measurement by transrectal ultrasound and computed tomography before and after permanent prostate brachytherapy." *Int. J. Radiat. Oncol. Biol. Phys.* **60**, 767-776 (2004).
- 24 J. Xue, F. Waterman, J. Handler, E. Gressen, "The effect of interobserver variability on transrectal ultrasonography-based postimplant dosimetry." *Brachytherapy* **5**, 174-182 (2006).
- 25 M.A. Moerland, H.K. Wijrdeman, R. Beersma, C.J. Bakker, J.J. Battermann, "Evaluation of permanent I-125 prostate implants using radiography and magnetic resonance imaging." *Int. J. Radiat. Oncol. Biol. Phys.* **37**, 927-933 (1997).
- 26 P.W. McLaughlin, V. Narayana, D.G. Drake, B.M. Miller, L. Marsh, J. Chan, R. Gonda, R.J. Winfield, P.L. Roberson, "Comparison of MRI pulse sequences in defining prostate volume after permanent implantation." *Int. J. Radiat. Oncol. Biol. Phys.* **54**, 703-711 (2002).
- 27 D. Taussky, L. Austen, A. Toi, I. Yeung, T. Williams, S. Pearson, M. McLean, G. Pond, J. Crook, "Sequential evaluation of prostate edema after permanent seed prostate brachytherapy using CT-MRI fusion." *Int. J. Radiat. Oncol. Biol. Phys.* **62**, 974-980 (2005).
- 28 C. Yang, S. Wang, A.T. Lin, C. Lin, "Factors affecting prostate volume estimation in computed tomography images." *Med. Dosim.* **36**, 85-90 (2011).

- 29 H. Ishiyama, M. Kitano, T. Satoh, Y. Niibe, M. Uemae, T. Fujita, S. Baba, K. Hayakawa, "Difference in rectal dosimetry between pre-plan and post-implant analysis in transperineal interstitial brachytherapy for prostate cancer." *Radiother. Oncol.* **78**, 194-198 (2006).
- 30 E.M. Messing, J.B. Zhang, D.J. Rubens, R.A. Brasacchio, J.G. Strang, A. Soni, M.C. Schell, P.G. Okunieff, Y. Yu, "Intraoperative optimized inverse planning for prostate brachytherapy: early experience." *Int. J. Radiat. Oncol. Biol. Phys.* **44**, 801-808 (1999).
- 31 S. Tong, H.N. Cardinal, R.F. McLoughlin, D.B. Downey, A. Fenster, "Intra- and inter-observer variability and reliability of prostate volume measurement via two-dimensional and three-dimensional ultrasound imaging." *Ultrasound Med. Biol.* **24**, 673-681 (1998).
- 32 M.J. Zelefsky, Y. Yamada, G.N. Cohen, A. Shippy, H. Chan, D. Fridman, M. Zaider, "Five-year outcome of intraoperative conformal permanent I-125 interstitial implantation for patients with clinically localized prostate cancer." *Int. J. Radiat. Oncol. Biol. Phys.* **67**, 65-70 (2007).
- 33 S. Nag, J.P. Ciezki, R. Cormack, S. Doggett, K. DeWyngaert, G.K. Edmundson, R.G. Stock, N.N. Stone, Y. Yu, M.J. Zelefsky, Clinical Research Committee, American Brachytherapy Society, "Intraoperative planning and evaluation of permanent prostate brachytherapy: report of the American Brachytherapy Society." *Int. J. Radiat. Oncol. Biol. Phys.* **51**, 1422-1430 (2001).
- 34 J.C. Blasko, "Low-dose-rate brachytherapy for prostate cancer: preplanning vs. intraoperative planning-preplanning is best." *Brachytherapy* **5**, 139-42 (2006).

Chapter 4 Volume determination using frustum and planimetry algorithms in context of ultrasound imaging

4.1 Introduction

Accurate prostate volume measurement is important for PPB. The volume is a determining factor in patient selection, as larger prostates have an increased possibility of implant complications, such as pubic arch obstruction and excessive number of needles for target coverage.¹⁻³ More importantly, the volume reflects the spatial extent of the prostate, influencing DVH calculations. The impact on reported dosimetry is prominently reflected in the variations due to CT contouring uncertainty.^{4,5} Prior to computerized treatment planning, prostate volume was calculated using the equation for an ellipsoid volume.^{6,7} The prostate is assumed to be ellipsoidal in shape, with the length, width, and height determined from orthogonal 2-D US imaging. Currently, volume is calculated from a series of transverse contours, most commonly using the planimetry method.

VariSeed is a popular TPS for PPB. The volume calculation algorithm used in VariSeed depends on image modality (VariSeed 8.0 User Guide). Prostate volumes obtained from MR and CT images are calculated via planimetry. Volumes from US images are calculated based on the frustum geometry defined by neighboring contours.

During the investigation comparing MR and US prostate contours (Chapter 3), it was observed that the US-determined volume as calculated by the TPS was underestimated by up to 10 %. It was later determined that a significant part of this difference was attributable to the volume calculation algorithm. Consistent application of the planimetry algorithm results in volumes that agree within 1 % on average. The use of different algorithms raises a potential concern as systematic volume differences could be mistaken for contouring bias between the imaging modalities. The study attempts to estimate the algorithm-related reconstruction error for prostate volumes by comparing the planimetry and frustum volume calculation algorithms in the context of transrectal US imaging.

4.2 Materials and methods

Prostate contours were obtained from 40 patients treated with permanent prostate brachytherapy. Prior to treatment, transrectal US and MR imaging were performed 4-6 weeks apart. US scans were performed with 5 mm inter-slice distance while the MR slice thickness was 3 (N = 6) or 4 mm (N = 34) with no inter-slice gap. The prostate was contoured by a radiation oncologist on anonymized images to minimize bias. Further details on patient characteristics, equipment, and scanning procedures can be found in a previously published study (Chapter 3).⁸

Volumes were calculated from the contour areas using both planimetry and frustum algorithms. The planimetry volume is the summation of slice area over the stack of m slices multiplied by the inter-slice distance Δ_z (Eq. 4.1).

$$volume_{planimetry} = \Delta_z \sum_{j=1}^m area_j \quad (4.1)$$

The frustum volume is the summation of a stack of frustums, each of separation Δ_z with two parallel planes outlined by areas from adjacent slices (Eq. 4.2).⁹

$$volume_{frustum} = \frac{\Delta_z}{3} \sum_{j=1}^{m-1} (area_j + area_{j+1} + \sqrt{area_j area_{j+1}}) \quad (4.2)$$

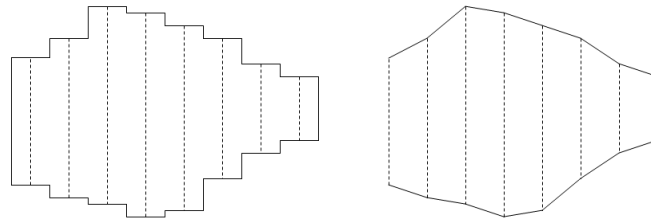


Figure 4.1: Sagittal view of identical prostate slices of zero thickness (dotted line) and the interpolated prostate volume boundaries (solid lines) as interpreted from planimetry (left) and frustum (right) algorithms.

Volume calculation can be interpreted as a continuous integral of the transverse cross-sectional area over the SI or z axis. Figure 4.1 illustrates the algorithm differences in terms of slice interpolation and the end (first and last) slices. The choice of algorithm affects how the sampled cross-sectional boundary is interpolated between slices.

Planimetry applies nearest neighbor shape-interpolation to determine the surface while the frustum algorithm applies linear shape-interpolation. Linear shape-interpolation of a convex object (i.e. prostate, ellipsoid) would systematically underestimate the volume. Kirisits *et al.* reported such a bias for a triangulated surface volume reconstruction method.¹⁰ Furthermore, the algorithms differ regarding the SI ends. For planimetry, the structure volume extends beyond the first and last contours by half the inter-slice distance. The frustum algorithm assumes that the end contours represent the SI surfaces, resulting in a smaller volume compared to planimetry. The difference is half the slice volume from each end.

Simulations of ellipsoid and truncated cone geometrical objects were done to determine algorithm reconstruction accuracy compared to theoretical formulas. Historically, the ellipsoid was used to represent the prostate for volume calculations.¹¹⁻¹³ An ellipsoid was generated with height, width, and length of 35.3, 48.7, and 33.4 mm reflecting average prostate dimensions.⁸ The SI length was aligned to the z-axis. A truncated cone of diameter ranging from 28 to 55 mm represented the bladder.¹⁰ The axis of the cone was parallel to the z-axis. A cone length of 43 mm was chosen to avoid being an integer multiple of the inter-slice distance. The two objects represent opposite situations at the SI ends. The ellipsoid tapers off at the ends while the truncated cone has flat end surfaces.

A voxel representation of these objects was used to simulate the finite resolution of an imaging system in the absence of noise. Each transverse slice was represented by a 2-dimensional grid of voxels with assigned values between 0 and 1, representing the object's volume fraction within the voxel. The object slice area was determined based on the number of voxels above a threshold value, with 0.5 representing unbiased discretization. Transverse slices were sampled at 2 to 5 mm inter-slice distances with offsets ranging from zero to the slice distance.¹⁴ The voxel transverse resolution was 0.2 x 0.2 mm² and the slice thickness varied up to the slice distance (i.e. no inter-slice gap).

Simulation parameters were chosen to mimic different imaging modalities. Simulations reflecting typical MR and CT acquisitions were done with no inter-slice gap. The results

were averaged over all offsets, representing the expectation value for an object placed randomly without deliberate slice positioning. As imaging is generally done only once, it is important to also consider the maximum and minimum values possible. Unlike MR or CT, the offset placement during transrectal US imaging is not random. The US probe is extended beyond the prostate base and retracted by fine adjustment until the base is just visible. Thus, simulations reflecting US imaging placed the superior slice at the superior-most position. Furthermore, US imaging slice thickness is typically 1 mm, resulting in an inter-slice gap.

4.3 Results and discussion

4.3.1 Clinical prostate contours

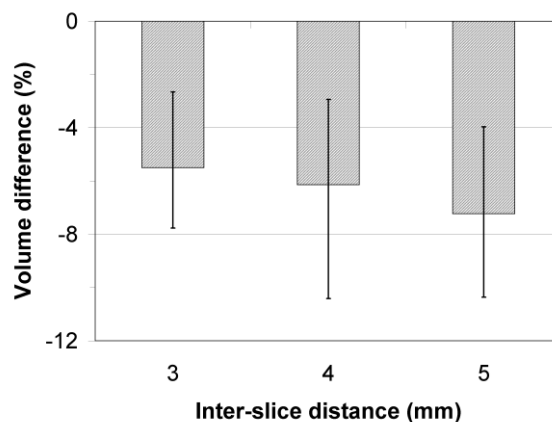


Figure 4.2: Prostate pair-wise volume difference between planimetry (reference volume) and frustum algorithms. Contours with 3 (N=6) and 4 (N=34) mm inter-slice distances were from magnetic resonance images while 5 mm contours (N=40) were from ultrasound images. Results are presented as average, maximum, and minimum differences.

Figure 4.2 plots the pair-wise difference between frustum and planimetry volumes from prostate contours delineated on MR and US images. The frustum volumes were systematically smaller than planimetry with the difference increasing with inter-slice distance (7 % at 5 mm). After accounting for the end slice extensions (see section 4.3.3), the residual volume difference was within 0.5 % for all inter-slice distances. Thus for both US and MR prostate contours, volume differences between algorithms were mostly due to the end slice effect.

4.3.2 Simulated object contours

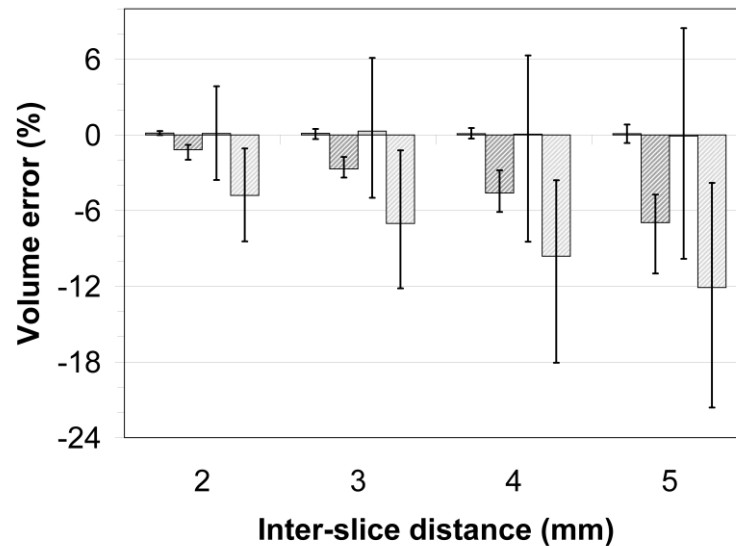


Figure 4.3: Ellipsoid (dark gray) and truncated cone (light gray) volume reconstruction accuracy using planimetry (solid) and frustum (diagonal) algorithms for various inter-slice distances. Simulations reflected MR and CT imaging. Results are presented as average, maximum, and minimum errors over all offsets.

Figure 4.3 compares the volume calculation accuracy for simulations reflecting MR and CT acquisition. On average, the planimetry algorithm was accurate to within 0.3 % for both geometries and all inter-slice distances. The frustum algorithm systematically underestimated both the ellipsoid and truncated cone, with errors of 7 and 12 % at 5 mm. The bias contribution due to linear interpolation was 1 % of the ellipsoid volume. For both algorithms, the sensitivity to the offset increased with inter-slice distance and was larger for the truncated cone.

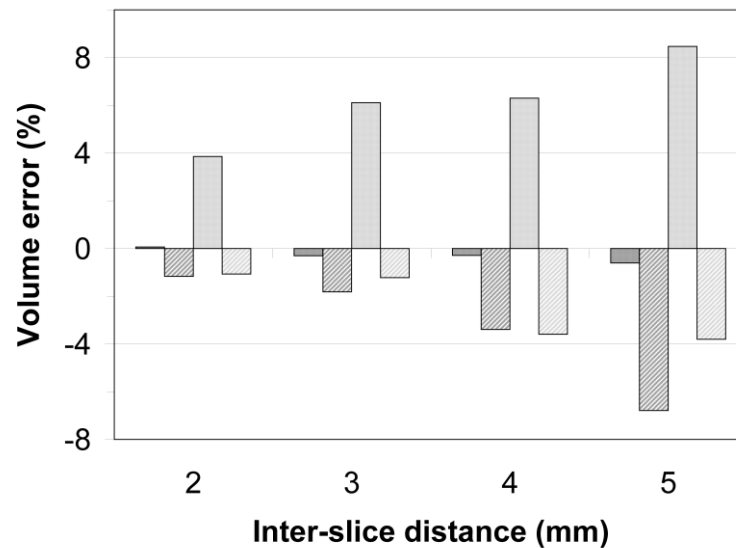


Figure 4.4: Ellipsoid (dark gray) and truncated cone (light gray) volume reconstruction accuracy using planimetry (solid) and frustum (diagonal) algorithms. Simulations reflected US imaging. The first slice was placed at the superior end of the volume.

Figure 4.4 plots the volume accuracy for contours simulating transrectal US image acquisition, reflecting a non-random starting point. The truncated cone results corresponded to the maximum volumes in figure 4.3, reducing the frustum error to -4 % but increasing the planimetry error to 8 % at 5 mm. The ellipsoid results were similar to averaged results in figure 4.3, with the planimetry algorithm accurately calculating the volume.

Deviation from 0.5 threshold introduced rounding bias in voxel discretization. The volume effect was linear with the slope dependent on the voxel size. For 5 mm with no inter-slice gap, the volume was 10 % smaller for a threshold of 0.75. Decreasing the slice thickness mitigated the effect. For 1 mm thickness, the volume decrease was 2 %. The slice thickness had negligible effect on the volume for a threshold of 0.5. Sagittal plane rotation of the ellipsoid up to 20 degrees about the lateral axis resulted in negligible volume difference.

4.3.3 Algorithm bias and volume estimation error

For random offset placement reflecting MR and CT imaging, the planimetry half-slice extension provided unbiased volume determination on both SI ends. The frustum

algorithm systematically ignored the volume beyond the end slices, which resulted in a bias of half the slice volume on each end. The error increased with inter-slice distance due to the increasing volume contribution of the end slices. Offset placement mimicking transrectal US acquisition removed the frustum bias at the superior end. The inferior end volume underestimation remained. Conversely, fixing the offset caused the planimetry algorithm to overestimate by half the superior slice volume. The planimetry bias was not noticeable for the ellipsoid due to its tapered end.

The frustum volume bias due to linear interpolation was small compared to the end slice effects. The maximum effect observed (2 %) was localized at the tapered end of the ellipsoid. The interpolation effect on volumes for the prostate contours was negligible (0.5 %).

The truncated cone results provide insight for deducing the algorithm-associated error made when calculating transrectal US prostate volumes, where the offset is placed at the superior end. Planimetry overestimates by half the superior slice volume. The average error at the inferior end is expected to be zero over the 40 prostate samples. Thus, the planimetry volumes from 5 mm US prostate contours were overestimated on average by 4 %. As the difference between the algorithms was 7 %, the frustum calculated volumes were underestimated by 3 %, mostly due to inferior end bias. The estimate assumed that the US transducer was centered on the prostate superior surface. Volume-averaging uncertainty in deciding when the base is just visible would affect the offset position by up to half the roughly 1 mm imaging plane thickness, corresponding to 0.8 % of the prostate volume.

Planimetry-calculated volumes from MR imaging yield accurate estimates of prostate volumes, compared to excised specimens.^{13,15} If planimetry is taken as the reference standard for MR, then the US prostate volumes, after accounting for algorithm bias, were 5 % smaller than MR on average. As MR and US are different imaging modalities, differences in image quality (i.e. contrast, noise) and contouring variability could also influence the results.

4.3.4 Literature comparison

Kirisits *et al.* investigated the volume reconstruction accuracy of a similar, physical truncated cone phantom imaged on CT and MR.¹⁰ The truncated cone volumes, reconstructed in VariSeed via planimetry, were consistently overestimated by ~10 % regardless of inter-slice distance (2, 4, 5 mm). The current simulations study found that a 10 % planimetry volume error is unlikely at 2 mm. The discrepancy demonstrates the impact of other factors in volume determination apart from the reconstruction algorithm.

4.4 Conclusion

The VariSeed treatment planning system employs either the planimetry or frustum algorithm for volume calculation, depending on image modality. Each algorithm offers a different interpretation for volume reconstruction, with planimetry volumes systematically larger than frustum. The discrepancy was mostly due to the end slice reconstruction. Simulations reflecting MR or CT imaging showed that planimetry volumes were accurate on average. For slice positioning that reflected US acquisition, the planimetry algorithm overestimated by half the superior slice volume while the frustum algorithm underestimated by half the inferior slice volume. Thus both algorithms introduce bias into transrectal US prostate volume determinations that may have clinical implications, planimetry overestimating and frustum underestimating the volume.

4.5 References

- 1 B.J. Davis, E.M. Horwitz, W.R. Lee, J.M. Crook, R.G. Stock, G.S. Merrick, W.M. Butler, P.D. Grimm, N.N. Stone, L. Potters, A.L. Zietman, M.J. Zelefsky, A.B. Society, "American Brachytherapy Society consensus guidelines for transrectal ultrasound-guided permanent prostate brachytherapy." *Brachytherapy* **11**, 6-19 (2012).
- 2 S. Nag, D. Beyer, J. Friedland, P. Grimm, R. Nath, "American Brachytherapy Society (ABS) recommendations for transperineal permanent brachytherapy of prostate cancer." *Int. J. Radiat. Oncol. Biol. Phys.* **44**, 789-799 (1999).

- 3 L. Potters, "Permanent prostate brachytherapy in men with clinically localised prostate cancer." *Clin. Oncol.* **15**, 301-315 (2003).
- 4 W.R. Lee, M. Roach, J. Michalski, B. Moran, D. Beyer, "Interobserver variability leads to significant differences in quantifiers of prostate implant adequacy." *Int. J. Radiat. Oncol. Biol. Phys.* **54**, 457-461 (2002).
- 5 J. Crook, M. Milosevic, P. Catton, I. Yeung, T. Haycocks, T. Tran, C. Catton, M. McLean, T. Panzarella, M.A. Haider, "Interobserver variation in postimplant computed tomography contouring affects quality assessment of prostate brachytherapy." *Brachytherapy* **1**, 66-73 (2002).
- 6 P.J. MacMahon, A. Kennedy, D.T. Murphy, M. Maher, M.M. McNicholas, "Modified prostate volume algorithm improves transrectal US volume estimation in men presenting for prostate brachytherapy." *Radiology* **250**, 273-280 (2009).
- 7 M.S. Nathan, K. Seenivasagam, Q. Mei, J.E. Wickham, R.A. Miller, "Transrectal ultrasonography: why are estimates of prostate volume and dimension so inaccurate?" *Br. J. Urol.* **77**, 401-407 (1996).
- 8 D. Liu, N. Usmani, S. Ghosh, W. Kamal, J. Pedersen, N. Pervez, D. Yee, B. Danielson, A. Murtha, J. Amanie, R.S. Sloboda, "Comparison of prostate volume, shape, and contouring variability determined from preimplant magnetic resonance and transrectal ultrasound images." *Brachytherapy* **11**, 284-291 (2012).
- 9 A.D. Polyanin and A.I. Chernoutsan, *A Concise Handbook of Mathematics, Physics, and Engineering Sciences* (Chapman & Hall/CRC, Boca Raton, FL., 2011).
- 10 C. Kirisits, F. Siebert, D. Baltas, M.D. Brabandere, T.P. Hellebust, D. Berger, J. Venselaar, "Accuracy of volume and DVH parameters determined with different brachytherapy treatment planning systems." *Radiother. Oncol.* **84**, 290-297 (2007).

- 11 P.J. Littrup, C.R. Williams, T.K. Egglin, R.A. Kane, "Determination of prostate volume with transrectal US for cancer screening. Part II. Accuracy of in vitro and in vivo techniques." *Radiology* **179**, 49-53 (1991).
- 12 C.H. Bangma, A.Q. Niemer, D.E. Grobbee, F.H. Schröder, "Transrectal ultrasonic volumetry of the prostate: in vivo comparison of different methods." *Prostate* **28**, 107-110 (1996).
- 13 C.W. Jeong, H.K. Park, S.K. Hong, S. Byun, H.J. Lee, S.E. Lee, "Comparison of prostate volume measured by transrectal ultrasonography and MRI with the actual prostate volume measured after radical prostatectomy." *Urol. Int.* **81**, 179-185 (2008).
- 14 R.G. Aarnink, R.J. Giesen, de la Rosette, J. J., A.L. Huynen, F.M. Debruyne, H. Wijkstra, "Planimetric volumetry of the prostate: how accurate is it?" *Physiol. Meas.* **16**, 141-150 (1995).
- 15 A. Rahmouni, A. Yang, C.M. Tempany, T. Frenkel, J. Epstein, P. Walsh, P.K. Lechner, C. Ricci, E. Zerhouni, "Accuracy of in-vivo assessment of prostatic volume by MRI and transrectal ultrasonography." *J. Comput. Assist. Tomogr.* **16**, 935-940 (1992).

Chapter 5 Incorporating a clinically-informed anisotropic edema model in dose calculations

5.1 Introduction

Prostate edema, or swelling of the prostate, is caused by surgical trauma from needle insertion during the PPB implantation procedure.¹ Edema build-up and subsequent resolution over time causes individual implanted seeds to move relative to the prostate and to other seeds, resulting in deviation from the reported planning and post-implant dosimetry. The treatment plan is based on the prostate absent of edema, which decreases the time-averaged distance between implanted seeds and increases the estimate of delivered dose. Post-implant evaluation assumes the imaged prostate and implant are static over the radioactive lifetime of the sources, and the reported dosimetry varies with the timing of image acquisition.

Incorporation of edema for PPB dose calculations requires modeling the movement of the prostate tissue relative to each implanted seed. The use of time-serial imaging and cumulative dose summation cannot account for the movement of the calculation voxel reflecting internal prostate deformation.² Chen *et al.* proposed a spatially isotropic, spatially-invariant edema model based on inter-seed distances and prostate contours from serial CT images.^{3,4} The prostate volume increased by a factor of 1.52 on average and the edema resolved inverse exponentially with an average half-life of 9.3 days. The model was used to generate a table of estimated edema-related dosimetric effects for both I-125 and Pd-103 implants.¹ For the average edema parameters, post-implant evaluation during peak edema would result in a 20 % underestimation in dose delivered to the PTV. The optimal timing of post-implant dosimetry was determined to be 7 weeks.

More recently, Sloboda *et al.* investigated the time course of prostate edema based on sequential MR imaging, and found widely different edema characterization.⁵ The edema was spatially anisotropic, with expansion present in the AP and SI directions but practically absent in the lateral direction. The mean volume increase was close to 20 %

for a cohort of 40 patients implanted at the Cross Cancer Institute. The edema resolution was linear in time and the prostate roughly returned to its original volume in 28 days on average. Reported edema parameters can vary depending on implant technique (i.e. number of needles, needle gauge, and insertion method) but are also influenced by uncertainties such as seed migration and contouring variability.

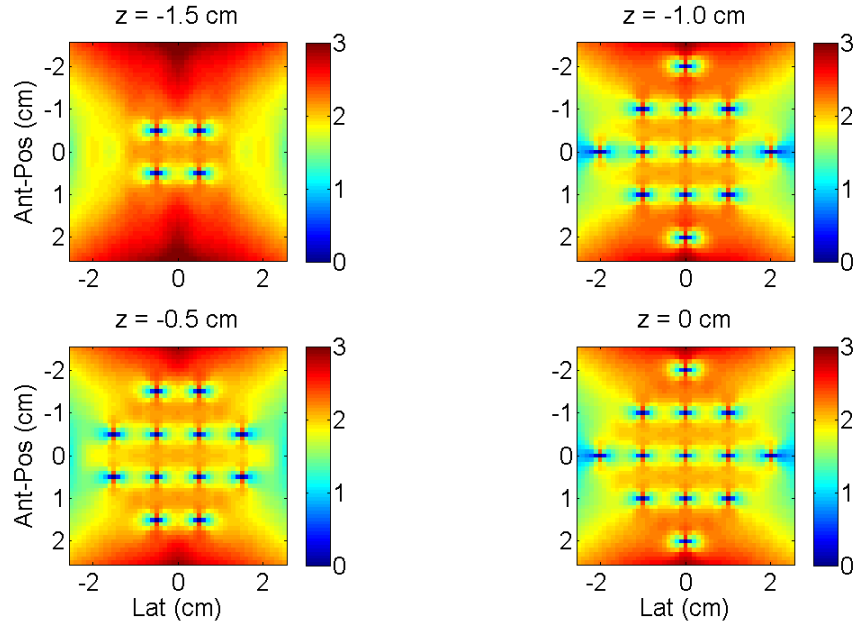


Figure 5.1: Relative dose percentage error (defined in equation 5.1) from neglecting edema for a simulated prostate phantom. Figure reproduced from Monajemi *et al.*⁶

Monajemi *et al.* proposed an anisotropic, linearly time-resolving model of the edema similar to Chen's isotropic, inverse exponentially time-resolving model but modified to incorporate the findings by Sloboda *et al.*^{5,6} The relative dose percentage error $RE\%$ (equation 5.1) was calculated for a Radiological Physics Center phantom for a range of edema parameters, using the TG-43 point source formalism.

$$RE\% = 100 \times \frac{D_{\text{implant}} - D_{\text{implant}}^{\text{edema}}}{D_{\text{implant}}^{\text{edema}}} \quad (5.1)$$

Figure 5.1 illustrates the relative dose error from neglecting edema for reported average edema parameters. The average error was 2 % with maximum error of 3 %. The relative error increased with each of the parameters: edema magnitude and resolution time.

The present study expands upon the results by Monajemi *et al.*, implementing the dose calculation using the TG-43 line source formalism and incorporating the anisotropic edema model for clinical dose calculations. The edema-related effects on planning and post-implant dosimetry are assessed for a cohort of patients, reflecting typical variations observed in clinical treatment plans and implants.

5.2 Materials and methods

5.2.1 Edema model

The anisotropic edema model proposed by Monajemi *et al.* is presented in equation 5.2, describing the movement of the prostate tissue relative to the seeds in Cartesian coordinates, with edema present in the AP and SI directions (y and z respectively), but not in the lateral x direction.⁶

$$\begin{aligned} x(t) &= x_{init} \\ y(t) &= y_{init} \sqrt{(1 + \Delta_{edema} (1 - t / T_{edema}))} \\ z(t) &= z_{init} \sqrt{(1 + \Delta_{edema} (1 - t / T_{edema}))} \\ 0 \leq t &\leq T_{edema} \end{aligned} \tag{5.2}$$

The edema parameters consist of the maximum magnitude Δ_{edema} and resolution period T_{edema} . The vector $(x_{init}, y_{init}, z_{init})$ gives the seed to calculation point distances with no edema present; the onset of maximum edema is presumed to occur instantaneously at $t = 0$. Note that for times beyond the edema resolution period, $y(t)$ and $z(t)$ assume their initial values without edema. The edema is spatially invariant and the equations describe the expansion in distance between any two points in the prostate. The model assumes that implanted seeds move with the surrounding prostate tissue and that the equations also govern the changing distance between a calculation point in tissue and an implanted seed. The model maps the position of a small volume of tissue over time, implicitly accounting for the movement of the prostate contour.

5.2.2 Dose calculation

The implant dose distribution is calculated using the TG-43 line source equation presented in equation 5.3, modified to show the explicit dependence on time.⁷

$$\dot{D}(r, \theta, t) = S_K(t) \times \Lambda \times \frac{G_L(r(t), \theta(t))}{G_L(r_0, \theta_0)} \times g_L(r(t)) \times F(r(t), \theta(t)) \quad (5.3)$$

The spatial relation between seed and calculation point, given by cylindrical coordinates $r(t)$ and $\theta(t)$, is dependent on time t with movement dictated by the edema model presented in equation 5.2. The air-kerma strength S_K decays exponentially with time. Therefore, the time-dependent dose-rate equation couples the radioactive decay with the implant and prostate movement. The remaining TG-43 parameters (dose-rate constant Λ , geometry function G_L , radial dose function g_L , and anisotropy function F) are described in detail in section 2.6.1. The reference point, (r_0, θ_0) , is defined to be 1 cm away on the transverse plane of the seed ($\theta_0 = \pi/2$). The total dose is calculated by integrating the dose-rate over the life time of the source.

5.2.3 Patient data and implementation

Treatment pre-plan and day 30 post-implant dosimetry incorporating edema was calculated for 10 patients (no specific selection criteria) treated with I-125 PPB with prescription dose of 145 Gy. The pre-plan and post-plan seed locations and 2-D prostate contours were exported from the VariSeed TPS to an in-house Matlab code (version R2011b; Mathworks, Natick, MA) for dose calculation and analysis. For each patient plan, dose calculation was performed for a static implant (conventional) and an implant incorporating the anisotropic edema model. The numerical integration of the dose-rate equation (equation 5.3), between time interval 0 and T_{edema} , was performed using the adaptive Simpson's method via the built-in Matlab function, `quadv`. Integration of the dose-rate after edema resolution was performed analytically using the conventional TG-43 equation. Edema parameters, with edema magnitude of 20% and resolution time of 28 days, were taken from clinical observations reported by Sloboda *et al.*⁵ Calculated dose distributions and contour structures were imported into CERR, an open-source treatment planning software, for DVH analysis.⁸

The dependence on radionuclide was investigated for one preplan case. The equivalent Pd-103 and Cs-131 plans were simulated by adjusting the source strength from 0.5 U for

I-125 to 2.0 U (Pd-103) and 2.5 U (Cs-131) in order to satisfy dose coverage criteria for the particular radionuclide.

5.3 Results and discussion

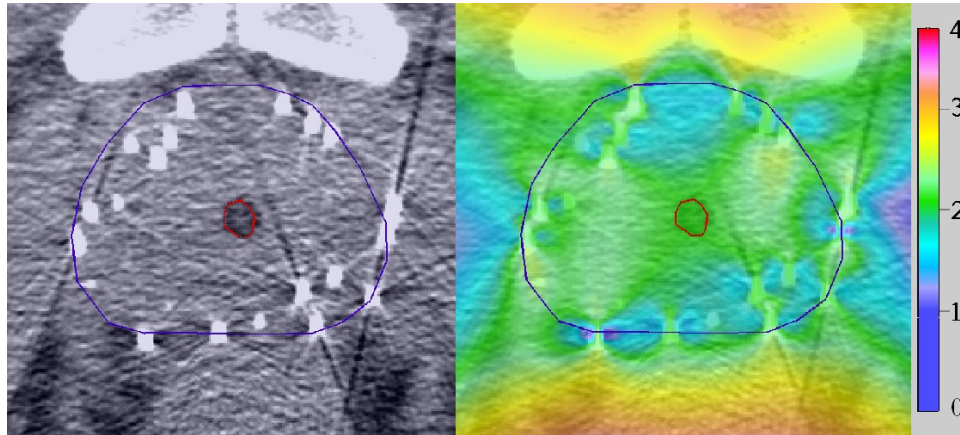


Figure 5.2: Post-implant CT image (left) of prostate (blue) and urethra (red) and the Corresponding color map (right) of the relative error (%) in conventional vs. edema-incorporated dosimetry.

Incorporating edema into the dose calculation led to an overall 2 % dose reduction relative to conventional calculation for a static seed distribution at day 30 (Figure 5.2), with little variation between patients and regions of the prostate (i.e. para-urethral, adjacent to bladder, prostate surface). The edema-related effect increased with distance from the implant. The relatively uniform dose reduction within the prostate reflected the relatively uniform implant distribution.

	Pre-plan		Post-plan	
Metric	Edema	Difference	Edema	Difference
D ₉₀	188 Gy (183 to 193)	4 Gy (3 to 4)	169 Gy (147 to 195)	3 Gy (3 to 4)
V ₁₀₀	99.6 % (99.2 to 100)	0.1 % (0.0 to 0.2)	95.9 % (90.7 to 99.8)	0.7 % (0.1 to 1.7)
V ₁₅₀	69.3 % (66.6 to 71.7)	3.1 % (2.5 to 4.1)	60.0 % (38.3 to 76.9)	2.7 % (1.9 to 3.5)
V ₂₀₀	27.8 % (20.2 to 35.9)	1.9 % (1.2 to 2.4)	23.8 % (12.5 to 37.5)	1.9 % (1.0 to 2.6)

Table 5.1: Mean and range of dose metric values for dose calculations incorporating edema and their differences (static minus edema) from conventional calculations for static implants.

The dose reduction from incorporating edema was similarly reflected in dosimetric values in Table 5.1. The prostate D₉₀ decreased by 3 to 4 Gy for both pre-plan and post-

plan distributions. The effect on V_{100} was less than 1 % but was up to 3 % for V_{150} . The variation of the edema-related effects, based on average edema parameter values, was much smaller than the variation in post-implant dosimetry between patient plans. The effect of prostatic edema for an I-125 implant is therefore largely dependent on the edema parameters (i.e. magnitude and resolution time), which has previously been reported.⁶

Compared to I-125, the effects of edema were substantially greater for the two shorter-lived radionuclides. For the one preplan case, the D_{90} decrease was 3.4 Gy for I-125 compared to 9.4 Gy for Pd-103 and 9.8 Gy for Cs-131. The difference between I-125 (60 days half-life) and Pd-103 (17 days) was greater than that between Pd-103 and Cs-131 (10 days).

5.4 Conclusion

The dosimetric effects of edema were determined using a clinically-informed edema model. For a 20% maximum edema magnitude and 28 day resolution time, the edema-incorporated dose for I-125 was only about 2 % lower than conventional static calculations, with little variation between patients and regions of the prostate. Similar differences were observed for clinical dose-volume metrics used in dosimetry evaluation. The effects of edema were calculated to be three to four times greater for Pd-103 and Cs-131 compared to I-125.

5.5 References

- 1 N. Yue, Z. Chen, R. Peschel, A.P. Dicker, F.M. Waterman, R. Nath, "Optimum timing for image-based dose evaluation of 125I and 103PD prostate seed implants." *Int. J. Radiat. Oncol. Biol. Phys.* **45**, 1063-1072 (1999).
- 2 G. Leclerc, M. Lavallée, R. Roy, E. Vigneault, L. Beaulieu, "Prostatic edema in 125I permanent prostate implants: dynamical dosimetry taking volume changes into account." *Med. Phys.* **33**, 574-583 (2006).

- 3 Z. Chen, N. Yue, X. Wang, K.B. Roberts, R. Peschel, R. Nath, "Dosimetric effects of edema in permanent prostate seed implants: a rigorous solution." *Int. J. Radiat. Oncol. Biol. Phys.* **47**, 1405-1419 (2000).
- 4 F.M. Waterman, N. Yue, B.W. Corn, A.P. Dicker, "Edema associated with I-125 or Pd-103 prostate brachytherapy and its impact on post-implant dosimetry: an analysis based on serial CT acquisition." *Int. J. Radiat. Oncol. Biol. Phys.* **41**, 1069-1077 (1998).
- 5 R.S. Sloboda, N. Usmani, J. Pedersen, A. Murtha, N. Pervez, D. Yee, "Time course of prostatic edema post permanent seed implant determined by magnetic resonance imaging." *Brachytherapy* **9**, 354-361 (2010).
- 6 T.T. Monajemi, C.M. Clements, R.S. Sloboda, "Dose calculation for permanent prostate implants incorporating spatially anisotropic linearly time-resolving edema." *Med. Phys.* **38**, 2289-2298 (2011).
- 7 M.J. Rivard, B.M. Coursey, L.A. DeWerd, W.F. Hanson, M.S. Huq, G.S. Ibbott, M.G. Mitch, R. Nath, J.F. Williamson, "Update of AAPM Task Group No. 43 Report: A revised AAPM protocol for brachytherapy dose calculations." *Med. Phys.* **31**, 633-674 (2004).
- 8 J.O. Deasy, A.I. Blanco, V.H. Clark, "CERR: a computational environment for radiotherapy research." *Med. Phys.* **30**, 979-985 (2003).

Chapter 6 Fast dose kernel interpolation using Fourier transform with application to permanent prostate brachytherapy dosimetry incorporating prostate edema

6.1 Introduction

The currently recommended approach for PPB clinical dose calculation is the AAPM TG-43 formalism.^{1,2} The calculation is based on the superposition of an analytic kernel representing the single seed dose-rate in a water medium of sufficient dimensions to provide full photon scatter conditions.³ The dose-rate distribution can be represented as that associated with either a 1-D spherically symmetric point source (point source formalism) or a 2-D cylindrically symmetric line source (line source formalism).

Clinical dose calculation based on TG-43 can be performed in a timely manner. Current methodology assumes that the spatial distribution of seeds and tissue is fixed and thus the dose-rate can be integrated over time via a multiplication factor. Direct TG-43 calculation for a typical PPB implant can be done within a minute on a dual-core PC. Furthermore, brachytherapy TPS likely uses pre-calculated high resolution kernels, eliminating the need for direct calculations and reducing the calculation time to a few seconds.

However, edema or swelling of the prostate due to needle insertion trauma causes seed movement over time.^{4,5} Analytical solutions to the dose-rate integral do exist, but are limited to specific edema models and to the point source formalism.^{6,7} For dose calculations incorporating prostatic edema, the general solution to the integral involves numerical integration, which becomes computationally intensive with calculation time greater than one hour. In addition, edema behaviour is patient specific, complicating the use of pre-calculated kernels.

Methods employing the FT, such as the one proposed by Boyer and Mok in 1986,⁸ have been proposed to significantly speed up PPB dose calculations, with computation time independent of the number of seeds. However, seed placement is limited to the

calculation grid points, reducing dose accuracy.⁹ As such, Boyer's method is of little benefit for clinical TG-43 dose calculation given the fast calculation times. Nevertheless, the computational efficiency of the method is potentially useful for calculations incorporating edema, although the limited seed placement remains a concern. Enabling unrestricted seed placement within the calculation grid volume requires resampling and interpolating the discrete dose kernel at the same spatial sampling frequency. The problem is commonly known as a fractional delay in the signal processing literature.¹⁰ However, the inverse square fall-off characterizing the long range behaviour of a PPB seed dose distribution presents a unique challenge.

In this work we expand upon Boyer's method and propose a FT-based interpolation method optimized for PPB, enabling unrestricted seed placement with clinically acceptable dose calculation accuracy while preserving the computational efficiency of the original method. The proposed method would enable accurate edema dose calculation within a reasonable amount of time. As the proposed method is not limited to dose calculation including edema and is applicable to any kernel-based PPB calculation, the method is presented and evaluated using the conventional TG-43 equations without edema in the interest of clarity.

For completeness, we also explore the application of FT-based interpolation for dose kernel rotation, which was another limitation mentioned by Boyer.⁸ Rotation is used to accommodate global post-implant seed orientations not congruent with the imaging scanner axis, that arise due to the change in patient body position between treatment (lithotomy position) and post-implant imaging (supine position).

6.2 Materials and methods

6.2.1 Snap-to-grid method

Equation 6.1 states Boyer's snap-to-grid method for calculating the PPB implant dose distribution, $D_{implant}$, at discrete grid positions given by the 3-D Cartesian vector \vec{x} . The dose kernel, D , as defined by the TG-43 equations (Eq. 2.1 and 2.4) is evaluated at the same grid points for a single seed with unity air-kerma strength placed at the origin. The

seed distribution function, I , is the superposition of n delta functions, each representing a seed at grid position \bar{x}_j with source strength $S_{K,j}$.

$$D_{implant}(\bar{x}) = D(\bar{x}) \otimes I(\bar{x}) = D(\bar{x}) \otimes \sum_{j=1}^n S_{K,j} \delta(\bar{x} - \bar{x}_j) \quad (6.1)$$

The convolution operation \otimes is performed in the Fourier domain (Eq. 6.2).

$$D_{implant}(\bar{x}) = \mathcal{F}^{-1}[\mathcal{F}[D(\bar{x})] \times \mathcal{F}[I(\bar{x})]] \quad (6.2)$$

Where \mathcal{F} and \mathcal{F}^{-1} denote the forward and inverse Fourier transforms respectively.

Each delta function convolution places a shifted copy of the kernel at the seed position, \bar{x}_j . However, the placement is limited to integer values corresponding to the calculation grid. The seeds are therefore snapped to the nearest grid point.

6.2.2 FT-interpolation method

The proposed method is an extension of the snap-to-grid method and is based on the addition of an interpolating filter. Equation 6.3 shows the new seed distribution function for the FT interpolation method.

$$I(\bar{x}) = \sum_{j=1}^n (S_{K,j} \delta(\bar{x} - \bar{\eta}_j) \otimes h_{3-D}(\bar{x}; \bar{\varepsilon}_j)) \quad (6.3)$$

Each seed position is separated into integer $\bar{\eta}_j$ and fractional $\bar{\varepsilon}_j$ components with respect to the calculation grid. The integer shift $\bar{\eta}_j$ is applied via the delta function shift as before. However, the unity coefficient of the delta function is replaced (i.e. convolved) with the 3rd order Lagrange interpolating filter $h_{3-D}(\bar{x}; \bar{\varepsilon}_j)$, with filter coefficients for each seed determined from the fraction offset $\bar{\varepsilon}_j$.¹⁰ For simplicity, equation 6.4 shows the 1-D interpolating filter $h_{1-D}(x_l; \varepsilon)$ in the x direction with 4 non-zero coefficients.

$$h_{1-D}(x_l; \varepsilon) = \prod_{\substack{j=0 \\ j \neq l}}^3 \frac{(\varepsilon - j)}{(l - j)}; l = 0, 1, 2, 3 \quad (6.4)$$

Where l is the index and ε is the fraction offset parameter. The 3rd order Lagrange coefficients represents the weights for a cubic interpolating polynomial in the Lagrange form. The application of the coefficients as a finite impulse response (FIR) filter,

generated in the spatial domain, performs the interpolation operation piece-wise for every kernel point, effectively shifting the kernel.

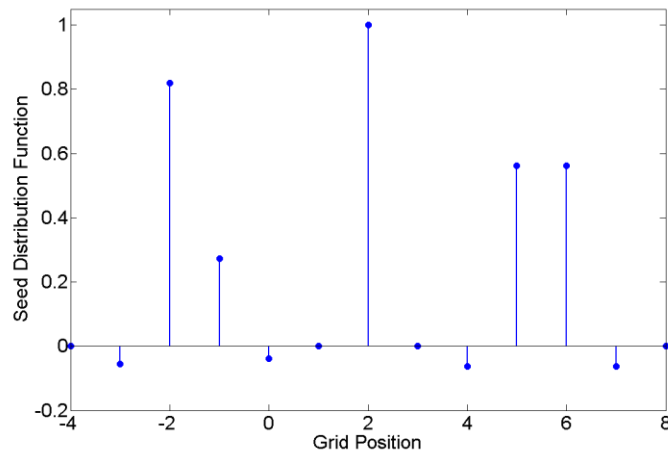


Figure 6.1: Example of the seed distribution function in 1-D.

Figure 6.1 illustrates the 1-D seed distribution function for three seeds placed at grid positions -1.75, 2, and 5.5. Note that for a fractional offset of zero, the Lagrange filter is equivalent to a delta function. For a 3-D scenario, the interpolating filter is the convolution of 1-D filters for each direction, with a total of $4^3 = 64$ non-zero coefficients.

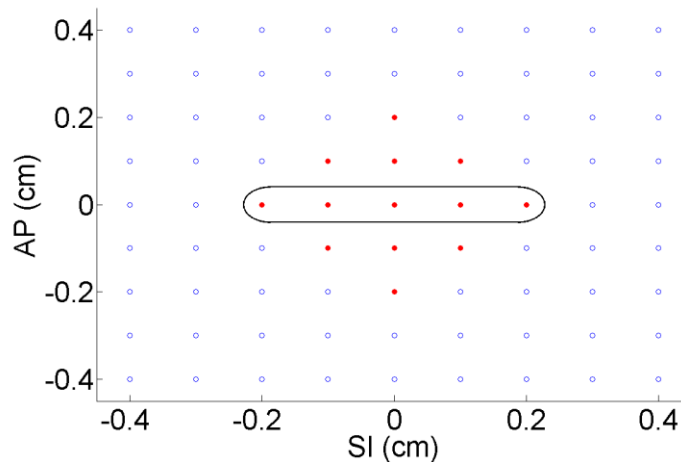


Figure 6.2: 2-D cross section of the dose kernel grid (blue, open circles) and modified kernel values (red, solid circles) with the physical projection of the seed.

For a 1 mm uniformly sampled dose kernel, direct application of the interpolating filter would result in unacceptably high interpolation error within 3 mm from the seed, due to the steep dose fall-off. To improve the interpolation accuracy between 2 and 3 mm,

kernel dose values within 2 mm from the seed were modified (Figure 6.2). Each modified kernel point only affects the interpolation locally.

Optimized values for a 0.5 U strength seed kernel were determined by minimizing the mean square interpolation error for dose values below 300 Gy, improving the interpolation accuracy for clinically relevant doses at the expense of accuracy at higher doses. The interpolation error was evaluated by up-sampling the kernel and comparing the interpolated values to reference TG-43 values from explicit calculation. Although 25 kernel values were modified for a 3-D grid, symmetry of the kernel dose distribution reduced the degrees of freedom during optimization to 4 for the point source and 7 for the line source. The complete FT interpolation method is given by equation 6.5

$$D_{\text{implant}}(\bar{x}) = D_{\text{opt}}(\bar{x}) \otimes \sum_{j=1}^n (S_{K,j} \delta(\bar{x} - \bar{\eta}_j) \otimes h_{3-D}(\bar{x}; \bar{\epsilon}_j)) \quad (6.5)$$

where D_{opt} is the modified single seed dose kernel after optimization.

6.2.3 FT-rotation method

The FT method has also been used for fast image rotation.¹¹ A 2-D rotation transform can be decomposed into a sequence of elementary shear operations, as shown in equation 6.6. In particular, the 3-pass algorithm is volume preserving (i.e. no scaling is required) and the associated shifts of each shear can be performed using the Lagrange interpolating filter.¹² Because the shifts vary with distance along the shearing direction, each slice in a 3-D grid is interpolated separately. For TG-43 line source calculations, two 2-D rotations are required to orient the seed, resulting in a total of 6 shear operations.

$$\mathfrak{R}_{2-D}(\theta) = \begin{bmatrix} \cos \theta & -\sin \theta \\ \sin \theta & \cos \theta \end{bmatrix} = \begin{bmatrix} 1 & -\tan \frac{\theta}{2} \\ 0 & 1 \end{bmatrix} \times \begin{bmatrix} 1 & 0 \\ \sin \theta & 1 \end{bmatrix} \times \begin{bmatrix} 1 & -\tan \frac{\theta}{2} \\ 0 & 1 \end{bmatrix} \quad (6.6)$$

The FT interpolation method was implemented for Iodine-125 seeds (GE Healthcare, Oncoseed, 6711) using both TG-43 point and line source formalisms.^{1,2,13} Post-implant plans were evaluated for 10 PPB patients with seed strength of 0.50 U and prescription dose of 145 Gy. The median prostate volume was 48.2 cc (range: 28.5 – 85.5 cc) and the median number of seeds implanted was 104 (range: 64 – 154). Details of the implant technique have been previously reported.⁴

6.2.4 Implementation

Post-plan contours and seed positions were exported from the VariSeed TPS. Dose distributions were calculated using FT interpolation and FT snap-to-grid methods and their accuracy referenced to explicit TG-43 calculations. Calculations were implemented using an in-house Matlab code (version R2011b; Mathworks, Natick, MA) on a 3 GHz Pentium-4 computer with 3 GB RAM. Both dose distribution and 0.5 U strength seed kernel were calculated on the same $81 \times 81 \times 81$ grid with uniform 1 mm resolution. The actual calculation grids were larger to avoid the discrete FT wrap-around effect. Explicit TG-43 calculation was additionally implemented in C++ to verify efficient coding in Matlab (i.e. vectorization). Contours and dose distributions were imported into CERR 4.0 for DVH calculations.¹⁴

To estimate the FT rotation operation accuracy, dose distributions were calculated assuming an average global seed orientation reported in the literature. Dose kernel rotations of 20 degrees polar (rising anteriorly from apex to base) and 10 degrees azimuthal angles were applied based on the TG-43 coordinate system.^{1,15,16} Dose distribution for the rotated kernel was calculated using the FT interpolation method.

6.3 Results

6.3.1 Dose distribution accuracy

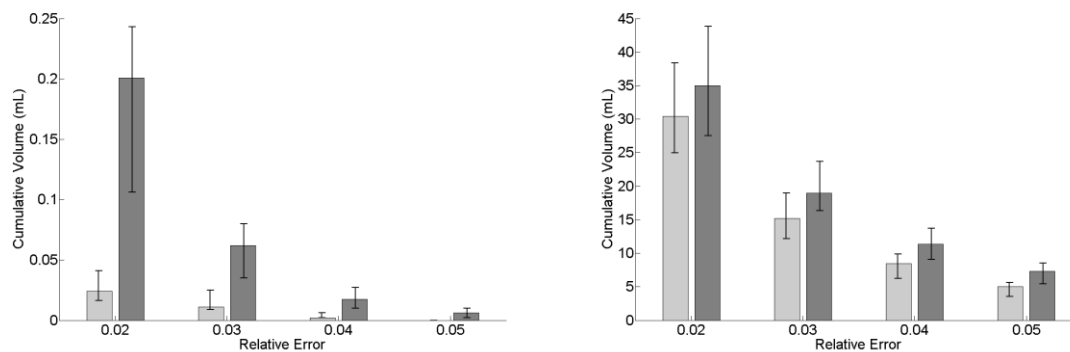


Figure 6.3: Right-cumulative volume histogram of the treatment plan dose error for point (light) and line (dark) sources calculated using the FT interpolation (left) and snap-to-grid (right) methods. Voxels with dose greater than 300 Gy were ignored. Values represent mean and range over 10 cases. Note the difference in the vertical scale.

Implementation of the interpolation method greatly improved FT-based dose distribution accuracy. Figure 6.3 compares the voxel dose accuracy between the two Fourier-based methods for 10 post-implant cases. For the FT interpolation method, voxel dose under 300 Gy was generally accurate to within 2 %, with maximum errors of 4 and 7 % for the point and line sources. Voxels with error above 2 % and dose less than 300 Gy constituted less than 0.1 and 1 % of the target volume for the point and line sources respectively. For the snap-to-grid method, more than 60 % of the calculation volume had dose error greater than 2 %, with 10 % greater than 5 %. The maximum dose error exceeded 20 %.

For the FT interpolation results, voxels with error above 2 % were spatially localized to a volume located within 2 mm from implanted seeds for the point source and 3 mm for the line source. Although the collective volume contribution of these voxels was close to 4 mL or 10 % of the clinical target volume, most had dose values greater than 300 Gy. The mean and maximum distances between voxels having a dose value greater than 300 Gy and the nearest implanted seed were 2 and 6 mm.

6.3.2 Kernel interpolation accuracy

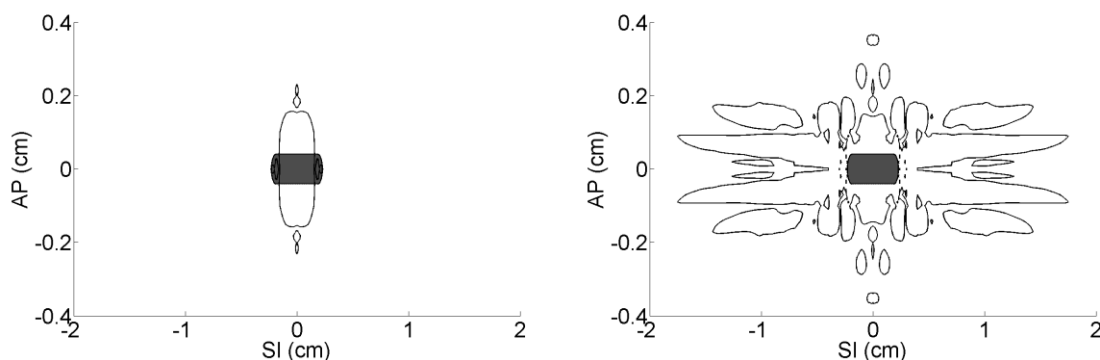


Figure 6.4: Single seed dose kernel interpolation error for the Iodine-125 model 6711 seed represented in the TG-43 formalism as a point (left) and line (right) source. The 2 % error isoline is shown (solid) with the physical projection of the seed (shaded).

Figure 6.4 shows the interpolation error for the single seed dose kernel, representing the optimized solution for the modified seed dose kernel used for subsequent dose distribution calculations. The point source interpolation was accurate to within 2 % at 3 mm, well within the recommended accuracy over the spatial range of interest.¹ The line

source interpolation error extended along the seed axis ($\theta = 0$), with 2 % error up to 1.5 cm beyond the ends of the seed but confined to a cylindrical region of 2 mm radius. The transverse view of the line source error was similar to that for the point source and was mostly within 2 % at 2 mm with small regions extending up to 4 mm. The spatial extent of the kernel interpolation error was not directly observed for each of the clinical seed set dose distributions due to contributions from other seeds.

6.3.3 Treatment dosimetry accuracy

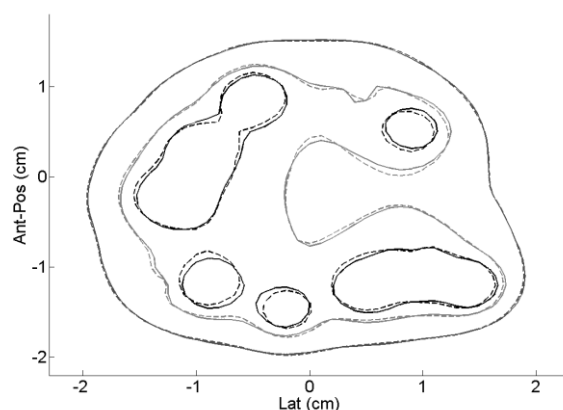


Figure 6.5: Post-implant 100, 150, 200 % isodose contours (100 % = 145 Gy) calculated in the TG-43 line source formalism using the snap-to-grid method (dash) and direct calculation (solid). FT interpolation contours were indistinguishable from direct calculation.

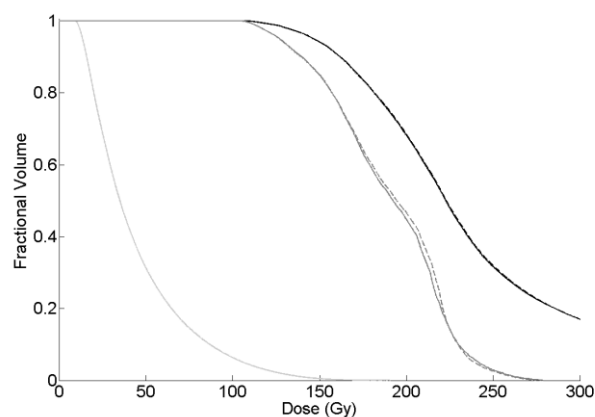


Figure 6.6: Dose-volume histogram for (from right to left) the prostate, urethra, and rectum calculated in the TG-43 line source formalism using the snap-to-grid method (dash) and direct calculation (solid). FT interpolation plots were indistinguishable from direct calculation.

Figure 6.5 compares mid-gland isodose contours for a representative patient calculated by the different methods using the line source formalism. The contours for the FT

interpolation method were indistinguishable from direct calculations. Contour shifts were visible for the snap-to-grid method, with the differences more pronounced in high dose regions closer to the seeds. Results were similar for the point source formalism. Figure 6.6 plots the DVH of the prostate, prostatic urethra, and rectum for a representative patient. FT interpolation plots were indistinguishable from direct calculations. Differences for snap-to-grid histograms were observed for the OARs.

Structure	Metric	Direct Cal	FT Interpolation		Snap-to-grid	
		Median	Abs Err	Rel Err	Abs Err	Rel Err
Prostate	D ₉₀	155.3 Gy	0.0	0.00%	1.2	0.67%
	V ₁₀₀	93.7 %	0.0	0.02%	0.8	1.00%
	V ₁₅₀	53.7 %	0.0	0.12%	1.0	1.56%
	V ₂₀₀	19.5 %	0.1	0.63%	0.5	4.55%
Prostatic Urethra	V ₁₀₀	0.872 cc	0.000	0.00%	0.021	3.10%
	V ₁₅₀	0.075 cc	0.000	0.00%	0.069	65.12%
	D _{1cc}	179.7 Gy	0.0	0.01%	3.2	1.65%
	D _{0.1cc}	229.0 Gy	0.1	0.04%	10.5	4.25%
	D ₁₀	212.8 Gy	0.0	0.00%	6.0	2.77%
	D ₃₀	187.6 Gy	0.0	0.00%	2.0	1.08%
Rectum	D _{2cc}	104.8 Gy	0.0	0.01%	1.9	1.44%
	D _{0.1cc}	147.4 Gy	0.1	0.03%	9.8	4.74%
	V ₁₀₀	0.045 cc	0.000	0.55%	0.037	47.38%

Table 6.1: Maximum dose-volume histogram metric errors over 10 cases.

Table 6.1 lists the maximum DVH metric errors for line source calculations. FT interpolation metrics were mostly accurate to within 0.1 %. The maximum prostate V₂₀₀ and rectum V₁₀₀ relative errors were 0.6 %. The errors were negligible given the precision of metric reporting. Metrics calculated using the snap-to-grid method had substantially larger errors, above 50 % for prostatic urethra V₁₅₀ and rectum V₁₀₀ and up to 5 % for the remaining metrics.

6.3.4 FT-based rotation

The dose calculation error for rotated seeds was slightly larger, due to the additional interpolation error associated with the shear operations. Voxels with error above 2 % were localized to 3.5 mm from implanted seeds. Voxels with error above 2 % and dose less than 300 Gy had a volume of 1.4 mL, constituting 3 % of the target volume. DVH results were fairly consistent for the various rotations and remained indistinguishable

from direct calculations. Errors in dose-volume metrics were mostly within 0.2 % with maximum error of 1 %.

6.3.5 Computation time

The computation time relating to direct calculation increased linearly with the number of seeds, and was approximately 4 minutes for the line source calculation. For a constant size calculation grid, the computation times for FT-based methods were essentially constant. The additional time associated with the interpolating filter was negligible and the FT interpolation method had the same computation time (2 s) as the snap-to-grid method. The overhead times for kernel calculation were 6 s for the point source and 13 s for the line sources. The FT methods were on average 15 and 20 times faster than direct calculations for the point and line sources. The computation time for the FT-rotation operation was one minute.

In practice, FT methods had a slight dependence on the number of seeds. An expanded calculation grid, based on the seed distribution span, was required to avoid the discrete FT wrap-around effect. The span increased with prostate size, which also correlated with the number of seeds required for treatment. The median grid size was 122x151x122, corresponding to an increase in the number of calculation grid points by a factor of 4.2 (range: 3.5 – 5.1). The rotation operation further increased that number by an additional factor of two, also due to wrap-around.

6.4 Discussion

6.4.1 Calculation accuracy

Accurate interpolation of a steep dose kernel was possible by sacrificing accuracy above 300 Gy. PPB dosimetry evaluation generally does not characterize the volume or distribution of points exceeding 200 % of the prescription dose and therefore was not affected.¹⁷ In addition, the spatial regions in which dose exceeded 300 Gy were mostly (99.8 %) within 5 mm of the seeds, where actual seed dosimetry can vary noticeably.¹ The causes of these uncertainties include internal source mobility and capsule geometry

and fabrication tolerances. The assignment of a point dose value to a voxel volume in a region of steep non-linear dose gradient is also problematic.

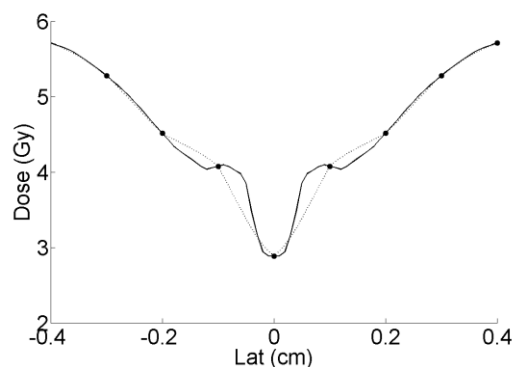


Figure 6.7: Lateral dose profile (solid) 1 cm away from the line source along the seed orientation axis. The 1 mm kernel (point) was under-sampled, resulting in interpolation error (dotted line).

Single seed dose interpolation for the point source was within 2 % error, ensuring accurate treatment plan, DVH, and metric calculations. On the other hand, the line source exhibited 2 % interpolation error up to 1.5 cm away from the seed (Figure 6.4). The error was due to the high frequency behaviour of the anisotropy function near $\theta = 0$, resulting in kernel under-sampling (Figure 6.7). If necessary, a higher resolution kernel could be used at the expense of computation speed. Nevertheless, the dose to the region in a PPB implant was small, less than 10 Gy, compared to the contribution from remaining seeds. Thus, the overall effect on the treatment plan was greatly reduced and the implant dose distribution was accurate beyond 3 mm from each seed.

For treatment plan calculations, the error was localized to high dose regions surrounding the seeds and the effects on clinical dose evaluation such as DVHs (Figure 6.6) and metrics (Table 6.1) were negligible. However, peak dose metrics involving high doses and small volumes could be sensitive to interpolation error, which was observed for one case. A urethral segment outside the prostate was in close proximity to a seed, and therefore was associated with a $D_{0.1cc}$ of 350 Gy. However, at 2 mm from the seed, the TG-43 dose calculation is also subject to significant uncertainty.

Dosimetric differences between the snap-to-grid FT method and direct calculations can be considered from the point of view of seed localization error. The nearest neighbour

snapping of post-implant seeds involves effectively random shifts with a maximum shift of 0.87 mm (0.5 mm in each direction) for a 1 mm grid. CT localization errors are typically larger at 2 to 3 mm.^{18,19} Thus, the dosimetric errors related to CT localization are expected to be greater than those reported for the snap-to-grid method. Of particular concern are the OAR metrics involving high doses and small volumes (i.e. rectum V_{100} and prostatic urethra V_{150} in Table 6.1). Unlike the error associated with FT interpolation, the snap-to-grid error is due to seed placement, bringing a seed either closer to or further away from an OAR. Thus, CT localization uncertainty, being of larger magnitude, can have a substantial effect on OAR dosimetric outcomes.

6.4.2 Computational efficiency

Direct TG-43 calculation time for n seeds and N_{grid} grid points is proportional to $(n \times N_{grid})$. For FT-based methods, the kernel is calculated once, decoupling the seed number from the grid points in terms of computation complexity. However, there is an increase in computation cost associated with the forward and inverse FT transform operations, which at best has a complexity of $(N_{grid} \times \log_2(N_{grid}))$ when the Cooley-Tukey algorithm is used for an array length which is a power of two. The FT interpolation method has an additional 3rd order Lagrange interpolating filter, requiring 64 coefficient assignments for each seed instead of the single delta function assignment. The additional computation time involved is negligible. Techniques are available to further improve the computational performance of FT-based methods, including volume of interest rotation for efficient use of the calculation grid, use of real-valued FT, and sizing the calculation grid to a power of two for optimal fast Fourier transform algorithm performance.⁹

The FT rotation operation is incompatible with FT-based dose calculation in terms of computation efficiency. The operation is applied as a series of 2D-FTs. If individual seed orientations can be determined, the rotation would be applied separately for each seed.^{15,20} Thus, the kernel is no longer spatially invariant and a computation time independent of the number of seeds can no longer be realized. Another limiting factor for FT-based rotation is the additional expansion of the calculation grid necessary to avoid the wrap-around effect, further increasing the computation time and memory usage.

Given the decreased accuracy and increased computation cost, there seems little benefit in performing discrete kernel rotation over direct calculation of a rotated kernel. Only when the kernel calculation is prohibitively time consuming might the FT-based kernel rotation be beneficial.

6.4.3 Implementation

Signal processing techniques generally assume a band-limited signal, which is not the case for a PPB dose distribution. The kernel resolution necessary to strictly satisfy the Nyquist criterion is computationally prohibitive. The modified dose kernel can be partially interpreted as an upper threshold, reducing high frequency components. The kernel remains under-sampled near the seed but the resulting interpolation accuracy is sufficient.

The piece-wise 3rd order Lagrange interpolating filter was chosen for its sufficient accuracy, minimal computation cost, ease of implementation, and intuitive interpolation behaviour. The choice of interpolating filter is practically limitless and more accurate solutions than the one implemented here likely exist.^{10,21,22} Nevertheless, one key consideration is the filter length. A short finite impulse response (FIR) filter is essential for brachytherapy applications. Infinite impulse response (IIR) and long FIR filters are ill-suited due to the large range of doses involved. The IIR response to a unit impulse is infinite in spatial extent. Unless the response decays faster than the dose fall-off, the relative error can increase with distance from the source. IIR filters are also undesirable in terms of computation cost. Each seed placement requires N_{grid} filter coefficient assignments and the computation complexity is therefore $(n \times N_{grid})$, the same as direct calculations. The Lagrange interpolating filter represents the application of polynomial interpolation in signal and image processing.^{10,12} 3rd order cubic interpolation generally offers sufficient accuracy and higher order filters do not necessarily yield better results. Even order filters are rejected because the interpolation is not symmetric for the two sides of the dose distribution. The 1st order filter (i.e. linear interpolation) is not sufficiently accurate for the 1 mm kernel but can be adequate for kernels of sufficiently high resolution.

The FT interpolation method was evaluated here with the dose kernel and the dose grid each having the same resolution of 1 mm. A more realistic implementation may involve a hybrid approach, based on interpolation of a high resolution kernel and down-sampling via table look-up. The 1st order filter (i.e. linear interpolation) would possibly suffice. This approach potentially offers accurate dose look-up without resorting to excessively high kernel resolution and the accompanying memory usage. Another possible implementation is to partition the single seed dose distribution into non-overlapping long and short range regions. The long range dose contributions can be calculated using the proposed FT interpolation method with high accuracy and constant computation time. The short range dose can be calculated directly, avoiding the interpolation error near the seed. The short range region is only a fraction of the entire calculation volume and can be calculated with only modest additional computation cost.

6.4.4 Application to edema dose calculation

The FT interpolation method was applied as before to calculate dose for the 10 clinical implants under study in the presence of edema. A detailed description of the edema model is presented in Chapter 5. The edema-related movement as characterized in equation 5.2 is spatially invariant. The resulting dose kernel incorporating edema in equation 5.3 is also invariant of implant position and is compatible with the proposed FT-based interpolation method. The spatially invariant seed dose kernel was generated by numerical integration of the dose rate, with computation time of 2 minutes (3 GHz Pentium-4, 3 GB RAM). The total computation time, including real time kernel optimization and calculation, was 6 to 10 minutes, equivalent to direct calculations for 3 to 5 seeds. Dose calculation accuracy was similar to that presented here for the conventional TG-43 dosimetry without edema.

In comparison, pre-calculation of high resolution kernels for the range of patient specific edema parameters reported in the literature has excessive memory requirements.^{4,5} Alternatively, calculation of the high resolution kernel in real time has computation cost approaching that for direct calculations. An increase in kernel resolution by a factor of

four (from 1 mm to 0.25 mm) is roughly equivalent to direct calculation for 64 seeds plus the additional time associated with wrap-around. Therefore, FT interpolation is a competitive method for dose calculations incorporating edema, particularly when several scenarios involving different edema parameters are to be explored.

FT-based methods are applicable for any calculation involving convolution and superposition of a spatially invariant kernel. The proposed interpolation method can be extended to other brachytherapy seeds and high dose rate sources. However, the spatially invariant kernel is also a fundamental limitation of the TG-43 formalism. Considerations such as tissue heterogeneity and inter-seed attenuation are motivations for alternative dose calculation methods.³

6.5 Conclusion

A FT interpolation method for PPB TG-43 dose calculation was proposed, expanding upon Boyer's original method and enabling unrestricted seed placement in the calculation grid. The method used a 3rd order Lagrange fractional delay filter, applying piece-wise cubic interpolation via the Fourier transform. The proposed method substantially improved the clinically relevant dose accuracy with negligible additional computation cost, preserving the efficiency of the original method. Importantly, the method is applicable for dose calculations incorporating prostatic edema with similar accuracy results. The application to FT-based rotation was also explored but was found to offer little benefit compared to direct calculations.

6.6 References

- 1 M.J. Rivard, B.M. Coursey, L.A. DeWerd, W.F. Hanson, M.S. Huq, G.S. Ibbott, M.G. Mitch, R. Nath, J.F. Williamson, "Update of AAPM Task Group No. 43 Report: A revised AAPM protocol for brachytherapy dose calculations." *Med. Phys.* **31**, 633-674 (2004).
- 2 R. Nath, L.L. Anderson, G. Luxton, K.A. Weaver, J.F. Williamson, A.S. Meigooni, "Dosimetry of interstitial brachytherapy sources: recommendations of the AAPM

- Radiation Therapy Committee Task Group No. 43. American Association of Physicists in Medicine." *Med. Phys.* **22**, 209-234 (1995).
- 3 M.J. Rivard, J.L.M. Venselaar, L. Beaulieu, "The evolution of brachytherapy treatment planning." *Med. Phys.* **36**, 2136-2153 (2009).
- 4 R.S. Sloboda, N. Usmani, J. Pedersen, A. Murtha, N. Pervez, D. Yee, "Time course of prostatic edema post permanent seed implant determined by magnetic resonance imaging." *Brachytherapy* **9**, 354-361 (2010).
- 5 F.M. Waterman, N. Yue, B.W. Corn, A.P. Dicker, "Edema associated with I-125 or Pd-103 prostate brachytherapy and its impact on post-implant dosimetry: an analysis based on serial CT acquisition." *Int. J. Radiat. Oncol. Biol. Phys.* **41**, 1069-1077 (1998).
- 6 T.T. Monajemi, C.M. Clements, R.S. Sloboda, "Dose calculation for permanent prostate implants incorporating spatially anisotropic linearly time-resolving edema." *Med. Phys.* **38**, 2289-2298 (2011).
- 7 Z. Chen, N. Yue, X. Wang, K.B. Roberts, R. Peschel, R. Nath, "Dosimetric effects of edema in permanent prostate seed implants: a rigorous solution." *Int. J. Radiat. Oncol. Biol. Phys.* **47**, 1405-1419 (2000).
- 8 A.L. Boyer and E.C. Mok, "Brachytherapy seed dose distribution calculation employing the fast Fourier transform." *Med. Phys.* **13**, 525-529 (1986).
- 9 T. Kemmerer, M. Lahanas, D. Baltas, N. Zamboglou, "Dose-volume histograms computation comparisons using conventional methods and optimized fast Fourier transforms algorithms for brachytherapy." *Med. Phys.* **27**, 2343-2356 (2000).
- 10 T.I. Laakso, V. Valimaki, M. Karjalainen, U.K. Laine, "Splitting the unit delay," *IEEE Signal Process. Mag.* **13**, 30-60 (1996).
- 11 W.F. Eddy, M. Fitzgerald, D.C. Noll, "Improved image registration by using Fourier interpolation." *Magn. Reson. Med.* **36**, 923-931 (1996).

- 12 M. Unser, P. Thevenaz, L. Yaroslavsky, "Convolution-based interpolation for fast, high-quality rotation of images," *IEEE Trans. Image Process.* **4**, 1371-1381 (1995).
- 13 R.E.P. Taylor and D.W.O. Rogers, "An EGSnrc Monte Carlo-calculated database of TG-43 parameters." *Med. Phys.* **35**, 4228-4241 (2008).
- 14 J.O. Deasy, A.I. Blanco, V.H. Clark, "CERR: a computational environment for radiotherapy research." *Med. Phys.* **30**, 979-985 (2003).
- 15 N. Chng, I. Spadinger, R. Rasoda, W.J. Morris, S. Salcudean, "Prostate brachytherapy postimplant dosimetry: seed orientation and the impact of dosimetric anisotropy in stranded implants." *Med. Phys.* **39**, 721-731 (2012).
- 16 P. Lindsay, J. Battista, J.V. Dyk, "The effect of seed anisotropy on brachytherapy dose distributions using 125I and 103Pd." *Med. Phys.* **28**, 336-345 (2001).
- 17 R. Nath, W.S. Bice, W.M. Butler, Z. Chen, A.S. Meigooni, V. Narayana, M.J. Rivard, Y. Yu, American Association of Physicists in Medicine, "AAPM recommendations on dose prescription and reporting methods for permanent interstitial brachytherapy for prostate cancer: report of Task Group 137." *Med. Phys.* **36**, 5310-5322 (2009).
- 18 P.E. Lindsay, J.V. Dyk, J.J. Battista, "A systematic study of imaging uncertainties and their impact on 125I prostate brachytherapy dose evaluation." *Med. Phys.* **30**, 1897-1908 (2003).
- 19 H. Liu, G. Cheng, Y. Yu, R. Brasacchio, D. Rubens, J. Strang, L. Liao, E. Messing, "Automatic localization of implanted seeds from post-implant CT images." *Phys. Med. Biol.* **48**, 1191-1203 (2003).
- 20 K. Wachowicz, S.D. Thomas, B.G. Fallone, "Characterization of the susceptibility artifact around a prostate brachytherapy seed in MRI." *Med. Phys.* **33**, 4459-4467 (2006).

- 21 J.T. Olkkonen and H. Olkkonen, "Fractional Time-Shift B-Spline Filter," IEEE Signal Process. Lett. **14**, 688-691 (2007).
- 22 J.T. Olkkonen and H. Olkkonen, "Fractional Delay Filter Based on the B-Spline Transform," IEEE Signal Process. Lett. **14**, 97-100 (2007).

Chapter 7 Implanted brachytherapy seed movement due to transrectal ultrasound probe-induced prostate deformation

7.1 Introduction

The relationship between planned and post-implant dosimetry is complex, with many contributing factors. Significant factors having a strong impact on dosimetry have been identified, such as prostate size and shape change between planning and delivery,¹ needle delivery accuracy,² and source migration.³ Other factors include contouring accuracy on CT⁴ and prostatic edema.⁵ To account for the various uncertainties, planning criteria are typically made more stringent than the desired dosimetric coverage, in order to successfully achieve the desired post-implant dosimetric parameters.^{6,7}

An additional factor that is generally unaccounted for is the seed movement and underlying prostate deformation due to the TRUS probe. During US imaging for treatment planning and seed delivery, probe contact pressure displaces and deforms the prostate. Hence seeds are planned for and delivered to the prostate under probe compression. After implantation, the probe is removed and post-implant dosimetry is performed for an uncompressed prostate. Literature concerning the probe-induced effects on permanent prostate implant movement and dosimetry is limited, probably due to the small potential effects that are expected from this phenomenon. Prostate shape differences reflecting probe-induced deformation have been reported.^{8,9} Moradi *et al.* proposed that such differences could be accounted for by using a warping function for each contour slice based on the prostate shape.¹⁰ A more detailed investigation into the effect would likely be difficult due to the similar magnitude of prostate contouring uncertainty relative to the scale of probe-induced deformation.

In this study, we investigated the effects of transrectal US probe pressure by observing the movement of implanted seeds, providing insight into the underlying prostate

deformation. The objectives are to characterize the seed movements upon probe removal and to estimate the impact on prostate dosimetry.

7.2 Materials and Methods

7.2.1 Implant technique

Ten patients were treated at the Tom Baker Cancer Centre via Iodine-125 permanent prostate brachytherapy with a prescription dose of 145 Gy. The intra-operative treatment was planned on the SPOT-PRO v3.0 system and implantation was performed using the FIRST remote after-loader system (Nucletron, Veenendaal, Netherlands), which deposits loose seeds using a Mick applicator. The average prostate volume was 45 cc (range: 34 – 62 cc) and the average number of implanted seeds (Nucletron, SelectSeed 130.002) was 74 (range: 60 – 94) with initial air kerma strength of 0.555 U. Additional details of the procedure have been previously reported.¹¹

7.2.2 Fluoroscopy imaging and seed localization

Fluoroscopy images of the implanted seed distribution were acquired immediately after delivery using an OEC 9800 C-arm (GE OEC Medical Systems, Salt Lake City, Utah). With the patient remaining in the lithotomy position, imaging was performed at three variable projection angles with maximum angular separation ranging from 39 to 51 degrees. The third projection was used to determine the position of the C-arm source and detector, thereby improving the reconstruction accuracy. Seed correspondence between the three projections was performed manually, with the aid of the treatment plan. The acquired images were corrected for image intensifier distortion, and the three-dimensional seed distribution was reconstructed using a previously reported method with a spatial consistency less than 1 mm.¹² For each patient, two sets of seed distributions were obtained, one with the prostate under probe compression (probe-in) and another with the probe removed (probe-out).

Seed movement analysis was performed using an in-house Matlab code (version R2011b; Mathworks, Natick, MA). The seed movements upon probe removal were quantified as the set of vectors from each probe-in seed to the corresponding probe-out seed. The

reconstruction provided the relative spatial distribution of an implant. For visualization of the movement patterns, seed distributions were registered using the subset of anteriorly implanted seeds, generally consisting of seeds from 4 to 6 needles. The optimal rigid transformation (translation and rotation) was determined by minimizing the least square distance between matched anterior seeds. The average residual displacement was 0.8 mm.

7.2.3 Ultrasound imaging and prostate delineation

Post-implant ultrasound imaging was performed in the time interval between acquisition of the two sets of fluoroscopic images. A three-dimensional volume acquisition was performed using the sagittal array of a bi-planar transrectal ultrasound probe (Aloka 1000, Hitachi Aloka Medical, Wallingford, CT). The prostate and the urethra path were delineated by an oncologist (N.U.) on reconstructed transverse slices with 2.5 mm thickness. The urethra contour on each slice was defined as a 5 mm diameter circle centered on the urethra path.

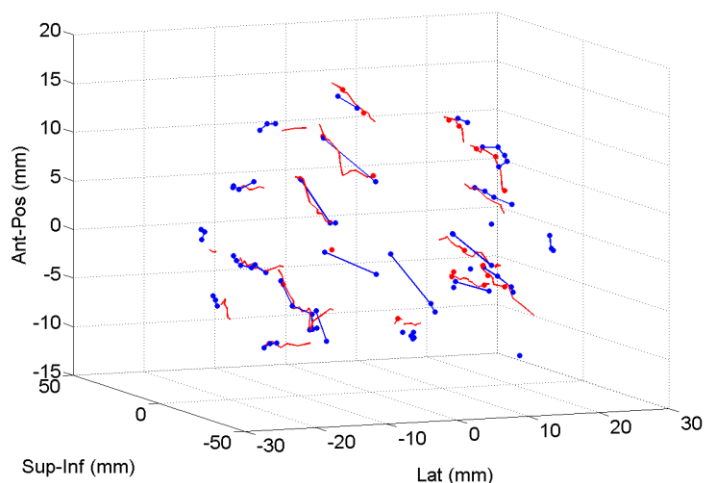


Figure 7.1: Optimized registration of ultrasound-based seed locations and needle track segments (red) to fluoroscopy-based seed locations (blue).

The prostate contour was registered to the probe-in fluoroscopy seed distribution using a subset of seeds and needle track segments visible on US. Seeds were manually localized on transverse images and matched to the treatment plan. Despite the availability of high resolution para-sagittal US views, individual seeds along a track were often difficult to distinguish. In such cases, entire tracks were localized and represented by a chain of line segments. Rigid registration, similar to that performed for the fluoroscopy seed

distributions, minimized the least square distance between seed locations and needle tracks on US and the corresponding fluoroscopy-based seed locations, as shown in Figure 7.1. The average residual was 3 mm. The prostate contour was used to classify implanted seeds as either intra- or extra- prostatic.

7.2.4 Seed movement model

A heuristic model of probe-induced seed movement was developed, inspired by linear elasticity theory. The collective seed movement for each patient was modeled as a 3x3 tensor matrix, \tilde{C} , linearly correlating seed movement, \bar{v} , with probe-in position, \bar{u} (Eq. 7.1).

$$\tilde{C} \cdot \bar{u} + \bar{b}_{CoM} = \bar{v} \quad (7.1)$$

Each dimensionless tensor element was associated with a transformation, with diagonal elements reflecting scaling in each direction and off-diagonal elements reflecting shearing. The correlation tensor was solved by linear regression and represented the least square solution to the over-determined system of equations. The intercept \bar{b}_{CoM} reflected the center of mass (CoM) shift of the seed distributions. Regression fitting was restricted to intra-prostatic seeds.

In addition, an observed residual correlation between the anterior-posterior movement, $(\bar{v})_{AP}$, and the probe-in lateral position, $(\bar{u})_{Lat}$, was further modeled. Following the approximate bi-lateral symmetry in the prostate geometry, linear functions were separately fitted for intra-prostatic seeds in each of the left and right lateral halves of the prostate (Eq. 7.2).

$$\begin{aligned} a_R (\bar{u})_{Lat} + b_R &= (\bar{v})_{AP}, & (\bar{u})_{Lat} &\leq 0 \\ a_L (\bar{u})_{Lat} + b_L &= (\bar{v})_{AP}, & (\bar{u})_{Lat} &> 0 \end{aligned} \quad (7.2)$$

Slope coefficients a_R , a_L represented the fractional shearing for the two halves, similar to the off-diagonal tensor elements. The intercept coefficients are b_R , b_L .

7.2.5 Simulation of prostate contour upon probe removal

To estimate the prostate surface in the absence of probe compression, the seed movement was used to infer the underlying prostate deformation. Probe-out contours were generated

by adjusting the probe-in contours according to the seed movement model. Although a linear model was unlikely to completely capture the complexity of physical prostate deformation, this enabled a sensible estimate of the associated effects to be made.

7.2.6 Dosimetric effects

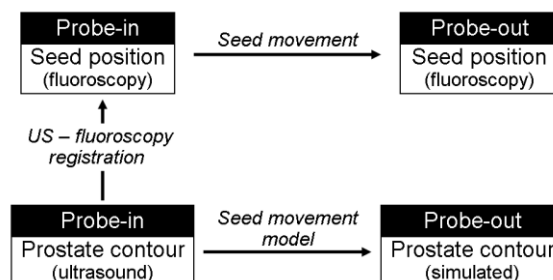


Figure 7.2: Relationship between seed distribution and prostate contour data.

Dosimetry was calculated for both probe-in and probe-out prostate volumes to determine the effects of probe removal. Figure 7.2 illustrates the relationship between the seed and contour data acquired for the study. Quadrant analysis was used to detect more localized effects on prostate dosimetry.¹³ Each probe-in and probe-out prostate volume was divided into four quadrants (posterior-left, posterior-right, anterior-left, and anterior-right) based on the CoM of the respective prostate. D_{90} and V_{100} metrics were calculated for the whole prostate and quadrant volumes. Larger contouring uncertainty has been reported for the post-implant prostate imaged on US¹⁴ relative to the pre-implant prostate. To account for this additional contouring uncertainty, prostate dosimetry results were also obtained using the preplan prostate contour, registered to the post-implant prostate CoM.

Dose distributions were calculated for each of the probe-in and probe-out seed distributions, using the TG-43 line source formalism.^{15,16} The calculation grid resolution was 1 mm in the axial plane with 2.5 mm spacing in the SI direction. Contours were resampled to match the dose calculation grid using a method similar to that described in Sloboda *et al.*⁵. Contour points were first converted to cylindrical coordinates oriented along the sup-inf direction. At each SI dose grid position, axial contours were resampled at 6 degrees angular intervals via bi-linear interpolation of the radial values.

7.3 Results

7.3.1 Seed movement

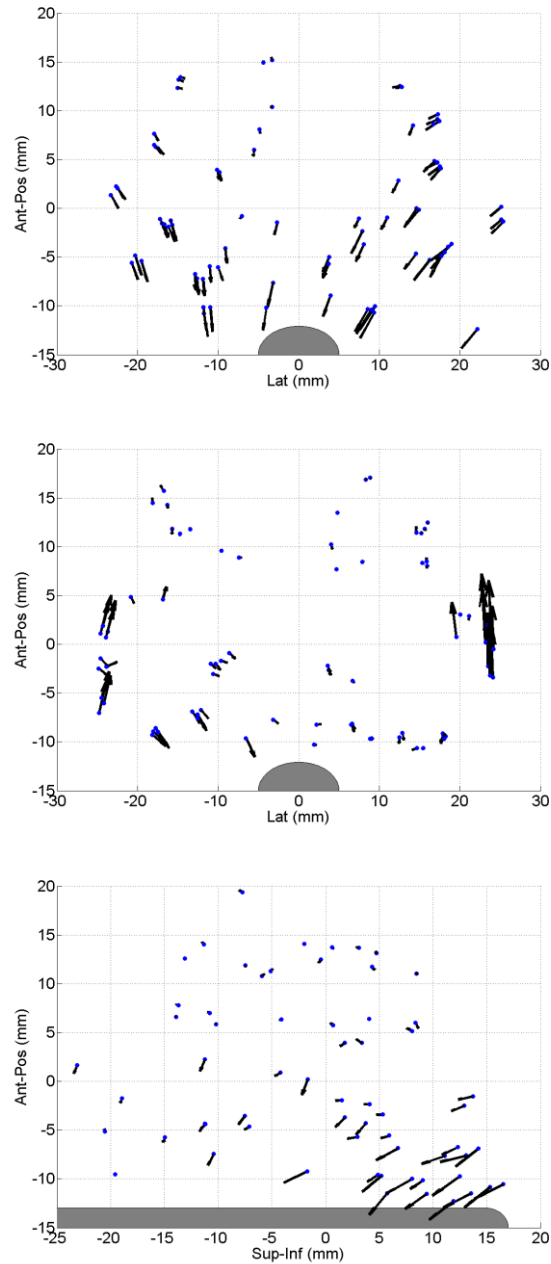


Figure 7.3: Implanted seed positions for the prostate under ultrasound probe pressure (points) and subsequent movements upon probe removal (arrows). Three movement patterns are shown along with the approximate location of the probe (shaded): elastic decompression in axial view (top), lateral shearing in axial view (middle), and rectal bending in sagittal view (bottom).

Figure 7.3 illustrates the three patterns of seed movement observed upon probe removal: elastic decompression, lateral shearing, and rectal bending. Patients exhibited a varying degree of all three movement patterns and each representative case above highlights a specific pattern.

The collective seed movement reflecting elastic decompression resulted in overall expansion along the AP direction and contractions along the lateral and SI directions. The increased AP span was 2 mm on average (max 4 mm) while the contractions were 1 mm on average (max 3 mm).

Lateral shearing was characterized by the anterior movement relative to the prostate CoM of seeds implanted in the lateral peripheral regions. The presence of lateral shearing was patient specific, with 6 of 10 cases exhibiting shearing movement on one or both sides. The movement pattern was generally the largest of the three modes, ranging from 3 to 6 mm (median 4 mm). Of the 47 seeds with anterior movement greater than 3 mm (from 5 patients with 412 seeds total), 81 % were extra-prostatic and an additional 13 % were within 1 mm from the prostate boundary, a distance that is well within the uncertainty associated with prostate contour delineation.

Rectal bending was inferred from the differential movement between superior and inferior seeds along the posterior prostate. The shearing appears non-uniform in that the movement was larger at the posterior prostate compared to the anterior prostate. The average movement of seeds implanted in the posterior base region was estimated as 3 mm.

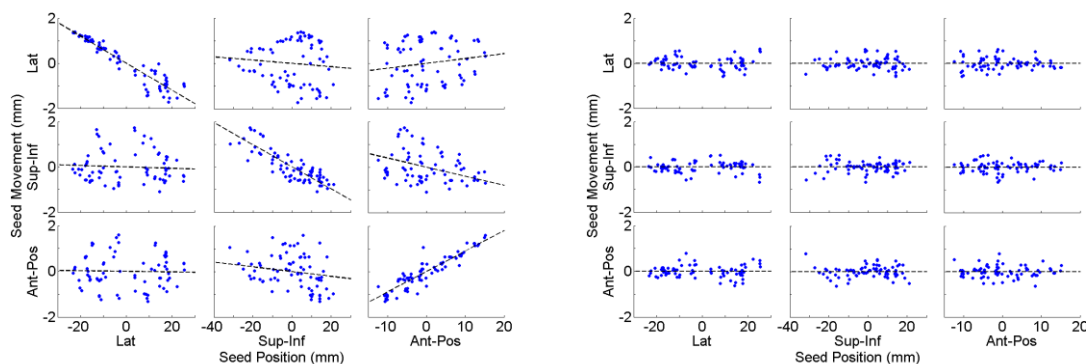


Figure 7.4: (left) Correlation plot between seed movement and position for a patient without lateral shearing movement. (right) Residual seed movement after tensor regression. Regression line is superimposed.

Figure 7.4 (left) plots the spatial correlation of seed movement corresponding to the elastic decompression pattern observed in Figure 7.3 (top). The 3x3 collection of plots is a visual representation of the correlation tensor in that the slope of each regression line fit to the data corresponds to a tensor element. Seed movement associated with elastic decompression manifested as linear correlation along the diagonal elements. Correlation between AP movement and SI position reflected rectal bending.

Figure 7.4 (right) plots the residual seed movements after tensor regression. The tensor model captured both elastic decompression and rectal bending movements. The reduction in the magnitudes of residuals in off-diagonal plots was mostly due to the regression along diagonal plots. For the plot corresponding to rectal bending (bottom center), residual seed movement suggesting a non-linear effect was observed at the sup-inf ends. Tensor regression did not adequately model the lateral shearing movement, which was not exhibited for the patient shown.

		Seed Position		
		Lateral	SI	AP
Seed Movement	Lateral	-0.029 (-0.005 to -0.072)	0.005 (-0.008 to 0.027)	0.008 (-0.022 to 0.034)
	SI	-0.001 (-0.007 to 0.010)	-0.029 (-0.009 to -0.049)	0.000 (-0.041 to 0.038)
	AP	0.003 (-0.024 to 0.025)	-0.040 (-0.077 to 0.060)	0.037 (-0.004 to 0.090)

Table 7.1: Regression values (mean and range) for the correlation tensor reflecting fractional expansion (diagonal) or shearing (off-diagonal) over 10 patients.

Table 7.1 lists the element values for the correlation tensor over all patients. Values associated with elastic decompression (diagonal) and rectal bending (AP movement and SI position) movement patterns were larger and statistically significant, with mean greater than twice the standard error. The tensor trace (sum of diagonal elements) was negative for 8 of the 10 patients, with the combined lat and SI contraction elements greater in magnitude than the AP expansion element. The apparent overall contraction of the seed distribution was confirmed by a measured decrease of 0.2 mm (range 0.0 to 0.6 mm) in the mean radius of intra-prostatic seeds with respect to the seed distribution CoM. Individual variations for the remaining off-diagonal elements were likely due to off-axis and rotational effects. The maximum rotation observed was 2 degrees and would manifest as anti-symmetric off-diagonal elements (values with opposite signs).

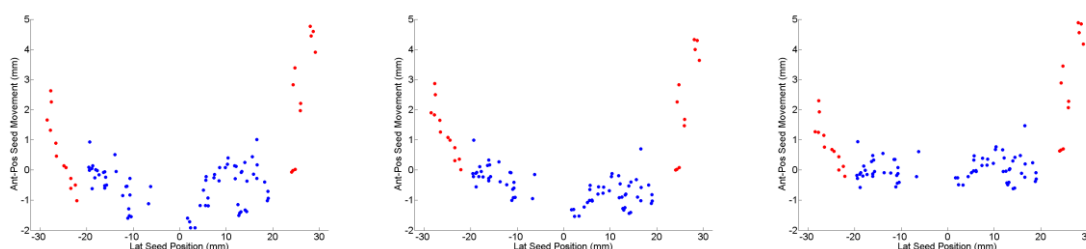


Figure 7.5: (left) Correlation plot exhibiting lateral shearing movement for intra-prostatic (blue) and extra-prostatic (red) seeds. (center) Residual movement after tensor regression. (right) Residual after additional lateral shearing regression for intra-prostatic seeds.

Seed movement due to lateral shearing was associated with AP movement as a function of lat position as shown in Figure 7.5 (left). Tensor regression alone did not adequately model the shearing movement, which was found to be isolated from the other movement patterns (Figure 7.5 center). A change in correlation pattern was observed between intra- and extra- prostatic seeds, with noticeably larger movement for extra-prostatic seeds. The shearing movement for intra-prostatic seeds was captured by an additional linear regression (Eq. 7.2), performed separately for each side of the prostate (Figure 7.5 right). Mean and range regression slope values for all patients were -0.038 (-0.156 to 0.012) and 0.028 (-0.030 to 0.123) for the left and right sides respectively. The magnitudes were comparable to the tensor elements associated with elastic decompression and rectal bending.

The full heuristic model, applying first tensor and then shearing linear regressions, captured most of the intra-prostatic seed movement, with average initial movement of 1.3 mm and residual of 0.6 mm (1.5 and 0.7 mm including extra-prostatic seeds).

7.3.2 Dosimetric effects

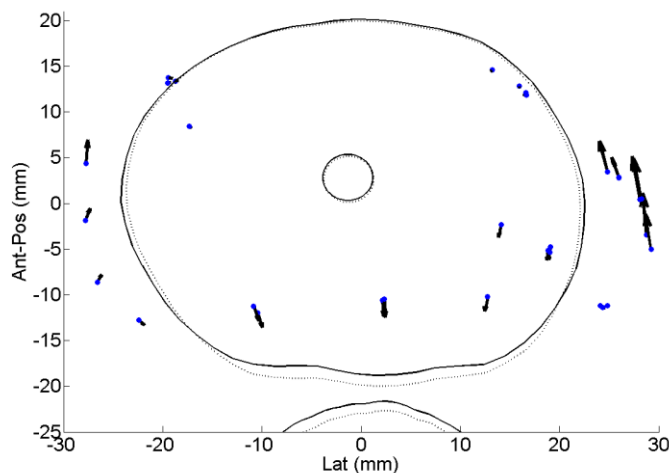


Figure 7.6: Mid-gland prostate, rectum, and urethra probe-in contours (solid) and estimated contours upon probe removal (dotted). Movement of seeds near mid-gland is superimposed.

Figure 7.6 shows the estimated prostate deformation at mid-gland superimposed on the movement pattern of nearby seeds. Extra-prostatic seeds in the lateral peripheral region moved in the anterior direction relative to the prostate CoM while the proximal sections of the prostate contour experienced small deformation. The posterior prostate contour moved posteriorly, following the movement of posterior seeds. Lateral contraction of the contour was also visible. The position of the urethra remained essentially unchanged.

Volume	Metric	Post-implant Contour		Preplan Contour	
		Dosimetry (probe-in)	Change upon probe removal	Dosimetry (probe-in)	Change upon probe removal
Whole Prostate	D ₉₀	135 Gy	4 Gy (0 to 8)	150 Gy	3 Gy (0 to 9)
	V ₁₀₀	86 %	2 % (0 to 4)	92 %	1 % (0 to 2)
Posterior Quadrants	D ₉₀	142 Gy	4 Gy (-2 to 9)	163 Gy	3 Gy (-5 to 12)
	V ₁₀₀	89 %	1 % (-1 to 3)	96 %	1 % (-1 to 3)
Anterior Quadrants	D ₉₀	135 Gy	4 Gy (-2 to 13)	145 Gy	4 Gy (-3 to 13)
	V ₁₀₀	83 %	3 % (0 to 6)	88 %	2 % (0 to 6)
Urethra	D ₁₀	178 Gy	2 Gy (-4 to 11)	207 Gy	2 Gy (-8 to 19)

Table 7.2: Effect on dose-volume metrics (mean and range) of US probe removal, calculated using post-implant and preplan prostate contours.

Table 7.2 lists the changes in dose-volume metrics that occurred upon probe removal. Results for the posterior quadrants include both posterior-left and posterior-right quadrants. The same applies for the anterior quadrants. For the post-implant contour, whole prostate D₉₀ and V₁₀₀ increased by 4 Gy and 2 % on average, with similar changes for the posterior (4 Gy) and anterior (4 Gy) quadrants. The V₁₀₀ increase was larger for the anterior quadrant (3 %) than the posterior quadrant (1 %) due to the lower anterior quadrant dose. The change in urethra D₁₀ exhibited larger individual variation, with an average increase of 2 Gy.

Average values of D₉₀ calculated for the (probe-in) post-implant and preplan prostate contours were 135 and 150 Gy, reflecting the post-implant US contouring uncertainty. Although absolute dose values varied between the pre- and post-implant contours, the differences between probe-in and probe-out dosimetry, reflecting the effects of probe removal, were similar.

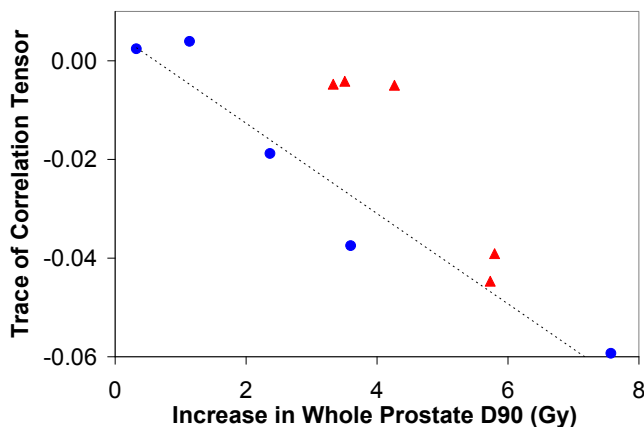


Figure 7.7: Relationship between whole prostate D_{90} and the trace of the correlation tensor. Red triangles represent patients with strong lateral shearing seed movements. The regression line for patients with minimal lateral shearing seed movements, represented by blue points, is shown for reference purposes.

Figure 7.7 shows the relationship between the correlation tensor trace and the change in whole prostate D_{90} . A negative trace value was associated with an increased D_{90} value up to 8 Gy. The dosimetric effects associated with lateral shearing seed movements were observable for patients with a trace value near zero. For the three patients with lateral shearing movements greater than 4 mm, the anterior dose increased while the posterior dose decreased or remained the same. For these selected patients, the differential change in D_{90} between the ant-pos quadrants was 7 Gy, and the whole prostate D_{90} increased by approximately 4 Gy.

7.4 Discussion

7.4.1 Image registration

Registration between probe-in and probe-out fluoroscopy-based seed distributions using the subset of anteriorly implanted seeds best illustrates the seed movement and improves the ability to visually discern movement patterns. The anterior prostate was a good reference region due to its relatively larger distance from the probe contact pressure and its proximity to the pelvic bone located further anterior of the prostate, which acts as a rigid and immovable structure. An alternate registration scheme based on the seed distribution CoM had the effect of averaging local movement patterns over the entire seed set. Nevertheless, the seed movement model was minimally affected by the choice

of registration method as the global prostate shift was captured by the regression intercept \bar{b}_{CoM} . Potential differences due to rotation between probe-in and probe-out seed distributions were small, with an observed maximum rotational difference of 3 degrees.

Registration uncertainty between US and fluoroscopy was larger in the SI direction due to US seed localization on transverse slices. In addition, registration of needle tracks was less sensitive to SI displacement. Nevertheless, the number of seeds that could be localized with confidence on US was sufficient for registration, and the average residual distance of 3 mm was comparable to similar implementations reported in the literature for both phantom and patient data.^{10,17-19}

It was observed that laterally scaling the US image by up to 10 % noticeably improved US-fluoroscopy registration for selected patients. No similar scaling benefit was observed in the AP and SI directions. This apparent discrepancy was not likely due to prostatic edema as US imaging took place immediately after fluoroscopy imaging of the probe-in seed distribution. Furthermore, based on serial magnetic resonance imaging, Sloboda *et al.* reported edema to be anisotropic and essentially absent in the lateral direction.⁵ Therefore other possible causes were considered. Seed localization from fluoroscopy reconstruction was accurate to within 0.5 mm in the lateral direction. It is unlikely that the retraction of the stabilizer needles used in the implant procedure was a factor, as the rotational motion of the probe during volume scanning should instead produce the opposite effect. Although the cause of the lateral scaling discrepancy is not known, the resulting contour shifts were within 2 mm and differences in probe-in and probe-out dosimetry were unaffected.

7.4.2 Seed movement

The anterior seed movement relative to the prostate CoM associated with lateral shearing was opposite to the posterior movement of the probe, reflecting translation of the prostate during probe removal. The movement was noticeably larger for extra-prostatic seeds implanted in the connective tissue surrounding the prostate. From the point of view of a stationary reference frame attached to the patient's pelvic anatomy, these seeds largely

remained in place while the prostate moved posteriorly. This behaviour was likely amplified due to the relaxation of the pelvic musculature induced by anesthesia. As the anesthesia wears off, it is possible that the lateral shearing effect is reduced.

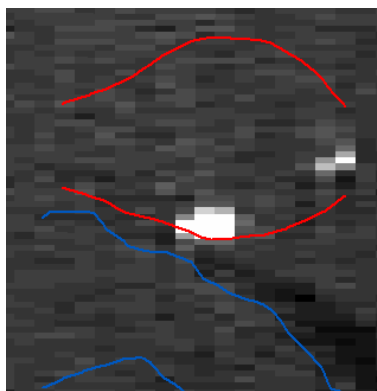


Figure 7.8: Post-implant sagittal CT slice showing the prostate (red) and the bending path of the rectum (blue). The patient superior direction is towards the right.

Rectal bending upon probe removal was observed as the posterior movement of seeds implanted near the superior portion of the rectum. The seed movement was consistent with the inferred causal rectum movement, from an initially straightened rectum on US (brought about by probe insertion) to a normally curved structure as seen on day 30 post-implant CT (Figure 7.8), and has potential consequences for rectal dosimetry. However, we were unable to determine with confidence the position of the rectum upon US probe removal. Although the bending-associated seed movement inside the prostate exhibits some linear correlation with seed position, the CT inferred movement at the rectum appears to be non-linear. Therefore, the rectal movement calculated by extrapolating the seed movement model to the distal rectal region would likely be underestimated.

7.4.3 Seed movement model

The residual seed movements observed were comparable in magnitude with the seed reconstruction accuracy, suggesting that the correlation tensor and shearing models sufficiently captured most of the intra-prostatic seed movement despite the underlying complexity of probe-induced prostate deformation. A physical model of prostate deformation would require at minimum knowledge of material properties, geometry, and boundary conditions. Higher-order deformations were not modeled but their effects are likely small as reflected in the residuals.

The prostate contour change associated with probe removal was estimated using the correlation tensor seed movement model. The use of this model to infer the underlying prostate deformation assumes that the intra-prostatic seeds move with the prostate. As non-stranded seeds were used in this study, this is a reasonable assumption. Movement of extra-prostatic seeds did not reflect internal prostate deformation and so was excluded from the regression fitting. The linear model represents a first order approximation of the prostate deformation, and enables a sensible estimate of the associated dosimetric effects to be made. Although extrapolation was required to estimate the probe-out contours, the distances involved were relatively small and contour movements were expected to be similar to those of the nearby seeds.

7.4.4 Dosimetric effects

The effect of TRUS probe-induced deformation on prostate dosimetry was primarily due to elastic decompression. The trace of the correlation tensor was predominately negative for all patients, reflecting greater contraction (lateral and SI) compared to the competing expansion (AP). Although individual seed movements were typically small, the systematic movement of the entire seed distribution resulted in a noticeable increase in whole prostate dose.

Due to the subset of peripheral seeds involved and their distance from the prostate, lateral shearing had a smaller effect on whole prostate dosimetry and was noticeable only when the elastic expansion and contraction effects were approximately equal. The relative anterior movement of the extra-prostatic seeds and the differential change in the prostate contour (Figure 7.6) resulted in increased dose in the anterior quadrants, sometimes at the expense of the posterior quadrants. The increase in whole prostate dosimetry reflected improved coverage in the anterior region, which had a lower dose on average than the posterior region. However, the magnitude of the seed movement was quite large in some cases, affecting the local dose distribution in the vicinity of the seeds. In particular, the reduced dose in the posterior-lateral region of the planning target volume can have potential negative consequences relating to the treatment of microscopic EPE.

The increase in urethra dosimetry reflected the overall dose increases inside the prostate. The larger variation reflected increased dosimetric sensitivity due to nearby seeds and the small volume of interest.

Although small on average, dosimetric effects were significant for selected cases, reflecting patient specific variations in seed movement. Elastic decompression resulted in a D_{90} increase of up to 8 Gy in our study group. The magnitude of the seed movement patterns observed for any given patient is likely related to the prostate stiffness and the applied probe pressure. Correlation with the prostate volume as measured by US was statistically insignificant.

For the lateral shearing seed movements, additional influencing factors include the spatial geometry of tissues surrounding the prostate and the seed loading pattern. In particular, seed distributions that emphasize implantation in the peripheral regions are likely more susceptible to larger lateral shearing effects.^{20,21} Although the movement of extra-prostatic seeds is difficult to anticipate, it can apparently be mitigated by implanting lateral seeds in closer proximity to the prostate. Such consideration should be taken into account to ensure adequate dose coverage in the posterior-lateral region, which is at higher risk of extra-prostatic extension.²² In addition, the impact of localized dosimetric effects associated with lateral shearing would be greater for emerging local treatments such as focal therapy.²³

This study demonstrates that there is seed movement after a brachytherapy implant that arises from the insertion and removal of the probe. Although this movement is small, it did result in measurable changes to the post-operative dosimetry. This highlights the probability that there are other movements of seeds that occur after an implant, due to prostate deformation occurring from normal physiological processes, such as rectal filling from flatus/stool or bladder filling from urine. Although all of these effects probably result in minor changes in dosimetry, it is important for clinicians and physicists to be

cognizant of these changes as the post-operative dosimetric values that they observe represent a snapshot of dose delivered to a patient.

7.4.5 Other uncertainties

Edema build-up was observed during seed implantation, similar to that reported in the literature.²⁴ Although edema was certainly present for the patients in our study at the time of imaging, seed and contour movements attributable to edema over the course of image acquisition should be minimal. Post-implant imaging on fluoroscopy and ultrasound was completed within 15 to 20 minutes. The mean radial distance of intra-prostatic seeds from the seed distribution CoM decreased by only 0.2 mm between the two fluoroscopy scans. Furthermore, the seed movements observed do not correspond to the anisotropic edema patterns reported.⁵ Thus, edema had likely built up to and remained near maximum during post implant image acquisition.

Post-implant whole prostate D_{90} was lower than the prescription dose, reflecting both seed placement inaccuracy and contouring uncertainty, particularly near the prostate base and apex. These two dosimetry influencing factors are well known to implant practitioners.^{4,10} Nevertheless, US probe-related dosimetric effects calculated using the corresponding preplan contour was found to be similar, and the overall conclusions remain the same. Whole prostate D_{90} for the preplan contour was similar to that reported for day 30 post-implant CT (150 Gy), the former being a more accurate contour although edema effects were not accounted for. Additional calculations were performed to determine the impact of US-fluoroscopy registration uncertainty, with similar null results. Therefore, the reported dosimetric effects due to US probe pressure are robust, and insensitive to contouring variability.

7.5 Conclusion

Seed movement due to removal of transrectal ultrasound-induced probe pressure after permanent prostate brachytherapy was characterized by distinctive movement patterns reflecting elastic decompression, lateral shearing, and rectal bending. Significant movement was observed for extra-prostatic seeds in the lateral peripheral regions. A heuristic model was developed that captured the linear correlation between intra-prostatic

seed movement and seed position. The model was used to infer the underlying prostate deformation, and to estimate the prostate contour in the absence of probe compression. Whole prostate dose coverage increased slightly upon US probe removal, mainly due to the small but systematic seed movement associated with elastic decompression. The D_{90} increase was 4 Gy on average with a maximum of 8 Gy. Lateral shearing seed movements increased dose coverage in the anterior-lateral region, sometimes at the expense of the posterior-lateral region. The effect on whole prostate D_{90} values was small (4 Gy max) compared to elastic decompression, due to the small subset of peripheral seeds involved, but is expected to have greater consequences for local dose coverage.

7.6 References

- 1 L. Beaulieu, S. Aubin, R. Taschereau, J. Pouliot, E. Vigneault, "Dosimetric impact of the variation of the prostate volume and shape between pretreatment planning and treatment procedure." *Int. J. Radiat. Oncol. Biol. Phys.* **53**, 215-221 (2002).
- 2 P.L. Roberson, V. Narayana, D.L. McShan, R.J. Winfield, P.W. McLaughlin, "Source placement error for permanent implant of the prostate." *Med. Phys.* **24**, 251-257 (1997).
- 3 E.M. Tapen, J.C. Blasko, P.D. Grimm, H. Ragde, R. Luse, S. Clifford, J. Sylvester, T.W. Griffin, "Reduction of radioactive seed embolization to the lung following prostate brachytherapy." *Int. J. Radiat. Oncol. Biol. Phys.* **42**, 1063-1067 (1998).
- 4 P.W. McLaughlin, C. Evans, M. Feng, V. Narayana, "Radiographic and anatomic basis for prostate contouring errors and methods to improve prostate contouring accuracy." *Int. J. Radiat. Oncol. Biol. Phys.* **76**, 369-378 (2010).
- 5 R.S. Sloboda, N. Usmani, J. Pedersen, A. Murtha, N. Pervez, D. Yee, "Time course of prostatic edema post permanent seed implant determined by magnetic resonance imaging." *Brachytherapy* **9**, 354-361 (2010).

- 6 R. Nath, W.S. Bice, W.M. Butler, Z. Chen, A.S. Meigooni, V. Narayana, M.J. Rivard, Y. Yu, American Association of Physicists in Medicine, "AAPM recommendations on dose prescription and reporting methods for permanent interstitial brachytherapy for prostate cancer: report of Task Group 137." *Med. Phys.* **36**, 5310-5322 (2009).
- 7 B. Al-Qaisieh, T. Witteveen, B. Carey, A. Henry, D. Bottomley, J. Smith, K. Franks, P. Bownes, "Correlation between pre- and postimplant dosimetry for iodine-125 seed implants for localized prostate cancer." *Int. J. Radiat. Oncol. Biol. Phys.* **75**, 626-630 (2009).
- 8 D. Liu, N. Usmani, S. Ghosh, W. Kamal, J. Pedersen, N. Pervez, D. Yee, B. Danielson, A. Murtha, J. Amanie, R.S. Sloboda, "Comparison of prostate volume, shape, and contouring variability determined from preimplant magnetic resonance and transrectal ultrasound images." *Brachytherapy* **11**, 284-291 (2012).
- 9 W.L. Smith, C. Lewis, G. Bauman, G. Rodrigues, D. D'Souza, R. Ash, D. Ho, V. Venkatesan, D. Downey, A. Fenster, "Prostate volume contouring: a 3D analysis of segmentation using 3DTRUS, CT, and MR." *Int. J. Radiat. Oncol. Biol. Phys.* **67**, 1238-1247 (2007).
- 10 M. Moradi, S.S. Mahdavi, E. Dehghan, J.R. Lobo, S. Deshmukh, W.J. Morris, G. Fichtinger, S.T.E. Salcudean, "Seed localization in ultrasound and registration to C-arm fluoroscopy using matched needle tracks for prostate brachytherapy." *IEEE Trans. Biomed. Eng.* **59**, 2558-2567 (2012).
- 11 D.R. Evans, T. Meyer, S. Angyalfi, S. Husain, I. Kay, P. Dunscombe, "Enhanced efficiency and ergonomics of an intraoperative automated prostate brachytherapy delivery technique." *Brachytherapy* **6**, 254-257 (2007).
- 12 T. Meyer and I. Kay, "Forward projection of variable angle imaging geometry to reduce reconstruction uncertainty and simplify seed matching in a backprojection algorithm." *Phys. Med. Biol.* **54**, 4595-4604 (2009).

- 13 I. Spadinger, W.J. Morris, M. Keyes, M. Liu, R. Shaffer, A. Thompson, N. Chng, R. Woods, "Quadrant dosimetry as a predictor of biochemical relapse in 125I prostate brachytherapy." *Brachytherapy* **10**, 87-97 (2011).
- 14 S. Smith, K. Wallner, G. Merrick, W. Butler, S. Sutlief, P. Grimm, "Interpretation of pre- versus postimplant TRUS images." *Med. Phys.* **30**, 920-924 (2003).
- 15 M.J. Rivard, B.M. Coursey, L.A. DeWerd, W.F. Hanson, M.S. Huq, G.S. Ibbott, M.G. Mitch, R. Nath, J.F. Williamson, "Update of AAPM Task Group No. 43 Report: A revised AAPM protocol for brachytherapy dose calculations." *Med. Phys.* **31**, 633-674 (2004).
- 16 R. Nath, L.L. Anderson, G. Luxton, K.A. Weaver, J.F. Williamson, A.S. Meigooni, "Dosimetry of interstitial brachytherapy sources: recommendations of the AAPM Radiation Therapy Committee Task Group No. 43. American Association of Physicists in Medicine." *Med. Phys.* **22**, 209-234 (1995).
- 17 P. Fallavollita, Z.K. Aghaloo, E.C. Burdette, D.Y. Song, P. Abolmaesumi, G. Fichtinger, "Registration between ultrasound and fluoroscopy or CT in prostate brachytherapy." *Med. Phys.* **37**, 2749-2760 (2010).
- 18 I.B. Tutar, L. Gong, S. Narayanan, S.D. Pathak, P.S. Cho, K. Wallner, Y. Kim, "Seed-based transrectal ultrasound-fluoroscopy registration method for intraoperative dosimetry analysis of prostate brachytherapy." *Med. Phys.* **35**, 840-848 (2008).
- 19 Y. Su, B.J. Davis, K.M. Furutani, M.G. Herman, R.A. Robb, "Seed localization and TRUS-fluoroscopy fusion for intraoperative prostate brachytherapy dosimetry." *Comput. Aided Surg.* **12**, 25-34 (2007).
- 20 W.M. Butler, G.S. Merrick, J.H. Lief, A.T. Dorsey, "Comparison of seed loading approaches in prostate brachytherapy." *Med. Phys.* **27**, 381-392 (2000).
- 21 L. Beaulieu, L. Archambault, S. Aubin, E. Oral, R. Taschereau, J. Pouliot, "The robustness of dose distributions to displacement and migration of 125I permanent seed

- implants over a wide range of seed number, activity, and designs." *Int. J. Radiat. Oncol. Biol. Phys.* **58**, 1298-1308 (2004).
- 22 B.J. Davis, E.M. Horwitz, W.R. Lee, J.M. Crook, R.G. Stock, G.S. Merrick, W.M. Butler, P.D. Grimm, N.N. Stone, L. Potters, A.L. Zietman, M.J. Zelefsky, A.B. Society, "American Brachytherapy Society consensus guidelines for transrectal ultrasound-guided permanent prostate brachytherapy." *Brachytherapy* **11**, 6-19 (2012).
- 23 J. Cosset, X. Cathelineau, G. Wakil, N. Pierrat, O. Quenzer, D. Prapotnich, E. Barret, F. Rozet, M. Galiano, G. Vallancien, "Focal brachytherapy for selected low-risk prostate cancers: a pilot study." *Brachytherapy* **12**, 331-337 (2013).
- 24 C. Chira, G. Delouya, S. Larrivée, J. Carrier, D. Taussky, "Prostate volume changes during permanent seed brachytherapy: an analysis of intra-operative variations, predictive factors and clinical implication." *Radiat Oncol* **8** (2013).

Chapter 8 Summary and future directions

8.1 Summary

The dosimetric goal of a PPB treatment is to deliver a dose distribution tailored to the patient, ideally giving the full prescription dose to the entire ETV while minimizing dose to neighbouring OARs. Dose to the target is correlated with cancer control^{1,2} while dose to an OAR is a risk factor for treatment toxicity.^{3,4} The dissertation critically assessed and, where possible, introduced novel advancements in various aspects of PPB, with the expectation of improving dosimetry. Chapters 3 and 4 identified means to evaluate and improve target definition during treatment planning by assessing US based prostate delineation accuracy with respect to MR imaging (the gold standard) and investigating the volume reconstruction on a commercial treatment planning system. Chapters 5 and 6 described novel methods that can improve the numerical accuracy of dose calculation by quantifying the dosimetric impact of prostatic edema and proposing a fast and accurate dose calculation method that incorporates edema. Chapter 7 established the groundwork for improving implant delivery by characterizing the previously unstudied seed movement and prostate deformation induced by the TRUS probe.

The accuracy of prostate delineation directly affects the conformity of the planned dose distribution to the target volume, which consists of the delineated prostate plus a margin to account for extra-prostatic extension of disease and uncertainties associated with contouring and seed placement. Chapter 3 investigated whether the superior soft tissue contrast provided by MR imaging can improve prostate delineation compared to the current procedure using US. The study found that overall prostate volume and inter-variability were similar between the prostate contoured on MR and US, suggesting confidence in delineation on US for a skilled observer. MR offered the potential for improved delineation at the prostate base and apex, regions known to be difficult to contour on US. Intra-observer variability at the base and apex was significantly lower for MRI. However, no difference was observed for the inter-observer variability, reflecting interpretation differences on MR delineation. Nevertheless, it is important to note that the

observers were much more experienced in prostate delineation on US, and the benefits of MR can likely be realized with a similar level of experience.

During the above mentioned investigation, it was observed that the MR and US prostate volumes reported on the VariSeed TPS were calculated using different algorithms, resulting in systematic differences up to 10 %. The dependence of the algorithm on modality (planimetry for MR and frustum for US) raised a potential concern as systematic volume differences due to the algorithm could be mistaken for contouring bias between the imaging modalities. Chapter 4 investigated the algorithm-related error for prostate volume calculations in the context of TRUS imaging. The study found that the planimetry volume was systematically larger than the frustum volume, due to extension beyond the first and last contour slices by half the inter-slice distance. US imaging acquisition is characterized by a large inter-slice gap (normally 5 mm) and non-random positioning of the first imaging slice (i.e. offset) at the prostate base. For US images, the planimetry algorithm overestimated by half the superior-most slice volume while the frustum algorithm underestimated by half the inferior-most slice volume. For MR images, the planimetry algorithm was unbiased for a random offset. MR and US prostate planimetry volumes reported in Chapter 3 were similar, with an average US/MR volume ratio of 0.99 ± 0.08 . Adjusting for the algorithm-related error, the average volume ratio is estimated at 0.96, suggesting only a slight underestimation of the prostate volume on US.

Prostatic edema results in movement of the prostate and implanted seeds, resulting in deviation from the reported planning and post-implant dosimetry. Accounting for edema-related dose effects requires modeling the movement of the prostate tissue relative to each implanted seed. An anisotropic, linearly time-resolving model of the edema was proposed by Monajemi *et al*, based on the edema time course observed on sequential MR imaging.⁵ Chapter 5 assessed the edema-related effects on planning and post-implant dosimetry for clinical dose calculations. For patient-average values of edema magnitude (20 % peak volume expansion) and resolution time (28 days to complete resolution), the I-125 implant dose distribution incorporating edema was approximately 2 % lower compared to conventional calculations absent of edema. Accounting for edema reduced

the prostate D_{90} by 3~4 Gy and was similar between patients, and between planning and post-implant distributions. The effect of prostatic edema was therefore largely determined by the patient-specific edema response. It was also determined that the effects of edema on dosimetry would be substantially greater for Pd-103 and Cs-137 seeds because of their shorter radioactive half-lives relative to I-125.

In general, clinical TG-43 dose calculation incorporating prostatic edema requires numerical integration of the dose-rate equation. The calculation of the dose from each seed to each calculation point is computationally intensive relative to that absent of edema, where the integral simplifies to a multiplication factor. Because the edema model is spatially invariant, the single seed dose distribution incorporating edema remains invariant and calculation methods based on kernel superposition can significantly improve computation efficiency. Boyer and Mok proposed such a method employing the FT but the seed placement was limited to the calculation grid points, greatly reducing calculation accuracy due to the steep gradients in PPB dose distributions.⁶ Chapter 6 expanded upon Boyer's method and proposed a FT-based interpolation method optimized for PPB, enabling unrestricted seed placement. The method is based on piece-wise 3rd order polynomial (i.e. cubic) interpolation implemented as a FIR filter with negligible additional computation cost. Direct application of the filter resulted in unacceptably high interpolation error near the seed due to the steep dose fall-off. Kernel values were modified to suppress the high spatial frequency component, improving interpolation accuracy for the clinically relevant dose range at the expense of higher doses above 300 Gy. The method substantially improved the clinically relevant dose accuracy, with negligible error in DVH and reporting parameters, while preserving the efficiency of the original method. The proposed FT-interpolation method accurately calculates the implant dose incorporating edema within a few minutes on a single core Pentium-4 3 GHz processor.

The global compression and deformation of the prostate due to probe pressure associated with TRUS imaging is relatively small, as observed in Chapter 3. The discrepancy, where seeds are planned for and implanted into a compressed prostate while post-implant

dosimetry is evaluated for an uncompressed prostate, is not currently accounted for in the treatment planning process. The scale of the probe-induced deformation is similar to the magnitude of contouring uncertainty, and hence the expected impact on dose-volume metrics is assumed to be negligible with respect to other factors affecting PPB dosimetry. Chapter 7 investigated the probe-induced prostate deformation using a novel approach based on the movement of implanted seeds, which can be localized with high accuracy. Distinctive seed movement patterns (primarily elastic decompression and shearing) were observed following removal of the probe, providing insight into the underlying prostate deformation. Seed movements associated with elastic decompression were small (mostly < 2 mm) but the collective movement resulted in the overall contraction of the implant distribution, resulting in a noticeable prostate D_{90} increase of 4 Gy (range 0 to 8 Gy). In addition, the observed movement of extra-prostatic seeds by up to 5 mm in the lateral peripheral regions is expected to have significant consequences for local PTV dose coverage, in particular the posterior-lateral margin accounting for EPE. Failure in PPB cancer control commonly relates to microscopic disease beyond the treatment volume. Thus, any reduction in dose coverage at the margins would likely impact the ability to account for EPE. Rectal doses calculated for treatment planning and post-implant evaluation purposes are also expected to differ because of US probe-induced deformation. The study demonstrated that probe-induced deformation of the prostate is non-negligible in many circumstances, contrary to common expectation.

Within a population of PPB patients, post-implant dosimetry exhibits a relatively large variation in reported values. At the CCI, the post-implant prostate D_{90} is typically between 150 and 200 Gy. In contrast, the treatment planning D_{90} is higher and has smaller variation, ranging from 180 to 200 Gy. The reported dosimetric impacts of edema (-4 to -3 Gy) and probe-induced prostate deformation (0 to 8 Gy) thus represent comparatively small shifts in dosimetry in opposing directions. The combined variance of the two effects only partially accounts for the range in reported post-implant dosimetry. The systematic reduction in D_{90} from planning to post-implant dosimetry is therefore likely due to other factors affecting PPB dosimetry, such as those mentioned in section 2.7.

Although the edema study demonstrated a systematic over-calculation of post-implant prostate dosimetry based on day 30 CT imaging, the results do not immediately warrant an adjustment in dose prescription or planning. The prescription dose for PPB is based on dose response studies performed on day 30 CT, which incorporate similar edema bias in reported dose values. It should be noted that consistency in methodology is equally important in PPB dosimetry, and hence any adjustment to clinical procedure requires careful consideration in the context of the entire treatment process.

8.2 Future directions

During the prostate delineation study in chapter 3, each patient was imaged on MR and US separately (i.e. MR patient in supine position and US patient in lithotomy position with probe pressure). Because the resulting prostate shape and orientation were different, direct comparison between MR and US contours was limited to the prostate volume. Contouring variability results only reflect the delineation consistency within each imaging modality. The results from chapter 4 suggest a slight but systematic underestimation of the prostate imaged on US. Identification of regional systematic delineation differences, such as that reported between CT and MR by McLaughlin *et al.*,⁷ would better inform delineation on US, in particular the apex and base. Direct comparison would require simultaneous imaging on MR and US with the patient in lithotomy position and the prostate under probe compression. Such imaging acquisition is difficult given the equipment currently available and is likely only possible for an MR machine that can image the patient in the lithotomy position (i.e. large bore) in combination with a MR-compatible US unit.

The current approach to target volume definition is to identify the whole prostate as the CTV, in order to account for possible additional disease foci not detected during diagnosis. As such, the reporting dosimetry emphasizes global prostate metrics (i.e. D_{90} , V_{100}). As reported in chapter 3, any local dosimetric advantages offered by MR imaging will likely be obscured by global metrics. Regional metrics such as D_{90} for each prostate quadrant have been proposed but their clinical significance has not yet been established. Emerging diagnostic methods such as MR spectroscopic imaging and US elastography

have the potential to localize disease within the prostate, generating interest in more localized therapy such as focal therapy or sub-volume boosts.^{8,9} It is with more localized therapy that precise localization of the tumour and surrounding anatomy assumes more importance and the advantages of MR imaging are expected to be realized.

The anisotropic edema model detailed in Chapter 5 was derived from prostate contours delineated on MR. The model assumes the edema is homogeneous and that implanted seeds move with the surrounding tissue. A follow-up clinical study to validate the two assumptions is underway, employing serial CT and MR imaging. The study will allow for comparison between the edema-related seed movement inferred from MR and the observed movement localized on CT. Systematic deviations between the implants would reflect regional variations in edema magnitude. Particular attention should be focused on seeds implanted outside the prostate, as these could exhibit differential behaviour from intra-prostatic seeds as highlighted by the probe-induced prostate deformation study (Chapter 7). Care should be taken to distinguish movement related to edema from that due to migration. In addition, the study will attempt to divide patients into two cohorts, one implanted with stranded seeds and another with loose seeds. Comparison between the two groups could determine the possible influence of seed stranding on edema-related seed movement, particularly in the SI direction.

The results of Chapter 7 brought to attention the effects of prostate deformation due to the TRUS probe, and demonstrated the potential to improve PPB dosimetry. However, to account for such effects in the clinic, additional investigation would be necessary to establish the reproducibility of seed movement and its dependence on probe placement (i.e. strength of the contract pressure and probe insertion technique). In particular, it would be informative to determine whether the relative importance of the three seed movement patterns identified is patient specific or operator dependent. Additionally, the prostate deformation was inferred from the movement of implanted seeds. In order to account for this movement during the planning stage, it would be necessary to correlate the movement patterns and magnitudes with prostate physical properties (i.e. mechanical stiffness, surrounding geometry, prostate volume). The movement of extra-prostatic seeds

is likely related to the absolute displacement of the prostate and the proximity of nearby pelvic bony structure.

The reported dosimetric values were based on isolating the probe-induced seed movement and represent the potential effects due to US probe pressure alone. Determining differences in dose-volume metrics in a comprehensive manner would require accounting for additional seed movement and prostate deformation over time due to effects such as edema, seed migration, and recovery of the pelvic musculature after anesthesia.

8.3 Conclusion

The dissertation explores potential improvements in the current approach to PPB dosimetry by assessing limitations and assumptions inherent in various stages of the clinical procedure. Novel insights and practical improvements are proposed, which aim to enhance the accuracy of radiation dose delivery during treatment. The thesis assessed prostate delineation accuracy on US during treatment planning, sought to improve dose calculation accuracy by accounting for edema, and investigated the previously unstudied effects due to probe-induced prostate deformation. With further research and development, these refinements can be implemented in the clinic, thereby potentially improving patient treatment outcomes.

8.4 References

- 1 R.G. Stock, N.N. Stone, A. Tabert, C. Iannuzzi, J.K. DeWyngaert, "A dose-response study for I-125 prostate implants." *Int. J. Radiat. Oncol. Biol. Phys.* **41**, 101-108 (1998).
- 2 M.J. Zelefsky and W.F. Whitmore, "Long-term results of retropubic permanent 125iodine implantation of the prostate for clinically localized prostatic cancer." *J. Urol.* **158** (1997).

- 3 M.J. Zelefsky, T. Hollister, A. Raben, S. Matthews, K.E. Wallner, "Five-year biochemical outcome and toxicity with transperineal CT-planned permanent I-125 prostate implantation for patients with localized prostate cancer." *Int. J. Radiat. Oncol. Biol. Phys.* **47**, 1261-1266 (2000).
- 4 S.H. Stokes, J.D. Real, P.W. Adams, J.C. Clements, S. Wuertzer, W. Kan, "Transperineal ultrasound-guided radioactive seed implantation for organ-confined carcinoma of the prostate." *Int. J. Radiat. Oncol. Biol. Phys.* **37**, 337-341 (1997).
- 5 T.T. Monajemi, C.M. Clements, R.S. Sloboda, "Dose calculation for permanent prostate implants incorporating spatially anisotropic linearly time-resolving edema." *Med. Phys.* **38**, 2289-2298 (2011).
- 6 A.L. Boyer and E.C. Mok, "Brachytherapy seed dose distribution calculation employing the fast Fourier transform." *Med. Phys.* **13**, 525-529 (1986).
- 7 P.W. McLaughlin, C. Evans, M. Feng, V. Narayana, "Radiographic and anatomic basis for prostate contouring errors and methods to improve prostate contouring accuracy." *Int. J. Radiat. Oncol. Biol. Phys.* **76**, 369-378 (2010).
- 8 B.G. Muller, W. van den Bos, P.A. Pinto, J.J. de la Rosette, "Imaging modalities in focal therapy: patient selection, treatment guidance, and follow-up." *Curr. Opin. Urol.* **24**, 218-224 (2014).
- 9 S.R. Mousavi, A. Sadeghi-Naini, G.J. Czarnota, A. Samani, "Towards clinical prostate ultrasound elastography using full inversion approach." *Med. Phys.* **41** (2014).

Bibliography

- 1 R.G. Aarnink, R.J. Giesen, de la Rosette, J. J., A.L. Huynen, F.M. Debruyne, H. Wijkstra, "Planimetric volumetry of the prostate: how accurate is it?" *Physiol. Meas.* **16**, 141-150 (1995).
- 2 N. Abolhassani, R. Patel, M. Moallem, "Needle insertion into soft tissue: a survey." *Med. Eng. Phys.* **29**, 413-431 (2007).
- 3 H. Afsharpour, G. Landry, M. D'Amours, S. Enger, B. Reniers, E. Poon, J. Carrier, F. Verhaegen, L. Beaulieu, "ALGEBRA: ALgorithm for the heterogeneous dosimetry based on GEANT4 for BRACHytherapy." *Phys. Med. Biol.* **57**, 3273-3280 (2012).
- 4 N.M. Alpert, J.F. Bradshaw, D. Kennedy, J.A. Correia, "The principal axes transformation--a method for image registration." *J. Nucl. Med.* **31**, 1717-1722 (1990).
- 5 B. Al-Qaisieh, B. Carey, D. Ash, D. Bottomley, "The use of linked seeds eliminates lung embolization following permanent seed implantation for prostate cancer." *Int. J. Radiat. Oncol. Biol. Phys.* **59**, 397-399 (2004).
- 6 J.N. Aronowitz and M.J. Rivard, "The phylogeny of permanent prostate brachytherapy." *J Contemp Brachytherapy* **5**, 89-92 (2013).
- 7 C.H. Bangma, A.Q. Niemer, D.E. Grobbee, F.H. Schröder, "Transrectal ultrasonic volumetry of the prostate: in vivo comparison of different methods." *Prostate* **28**, 107-110 (1996).
- 8 M. Barkati, S.V. Dyk, F. Foroudi, K. Narayan, "The use of magnetic resonance imaging for image-guided brachytherapy." *J Med Imaging Radiat Oncol* **54**, 137-141 (2010).
- 9 L. Beaulieu, L. Archambault, S. Aubin, E. Oral, R. Taschereau, J. Pouliot, "The robustness of dose distributions to displacement and migration of 125I permanent seed

- implants over a wide range of seed number, activity, and designs." *Int. J. Radiat. Oncol. Biol. Phys.* **58**, 1298-1308 (2004).
- 10 L. Beaulieu, S. Aubin, R. Taschereau, J. Pouliot, E. Vigneault, "Dosimetric impact of the variation of the prostate volume and shape between pretreatment planning and treatment procedure." *Int. J. Radiat. Oncol. Biol. Phys.* **53**, 215-221 (2002).
- 11 L. Beaulieu, D.R. Evans, S. Aubin, S. Angyalfi, S. Husain, I. Kay, A. Martin, N. Varfalvy, E. Vigneault, P. Dunscombe, "Bypassing the learning curve in permanent seed implants using state-of-the-art technology." *Int. J. Radiat. Oncol. Biol. Phys.* **67**, 71-77 (2007).
- 12 C.C. Blake, T.L. Elliot, P.J. Slomka, D.B. Downey, A. Fenster, "Variability and accuracy of measurements of prostate brachytherapy seed position in vitro using three-dimensional ultrasound: an intra- and inter-observer study." *Med. Phys.* **27**, 2788-2795 (2000).
- 13 J.C. Blasko, "Low-dose-rate brachytherapy for prostate cancer: preplanning vs. intraoperative planning-preplanning is best." *Brachytherapy* **5**, 139-42 (2006).
- 14 A.L. Boyer and E.C. Mok, "Brachytherapy seed dose distribution calculation employing the fast Fourier transform." *Med. Phys.* **13**, 525-529 (1986).
- 15 J. Bucci, I. Spadinger, M. Hilts, S. Sidhu, C. Smith, M. Keyes, W.J. Morris, "Urethral and periurethral dosimetry in prostate brachytherapy: is there a convenient surrogate?" *Int. J. Radiat. Oncol. Biol. Phys.* **54**, 1235-1242 (2002).
- 16 W.M. Butler, G.S. Merrick, J.H. Lief, A.T. Dorsey, "Comparison of seed loading approaches in prostate brachytherapy." *Med. Phys.* **27**, 381-392 (2000).
- 17 Canadian Cancer Society's Advisory Committee on Cancer Statistics, *Canadian Cancer Statistics* (Canadian Cancer Society, Toronto, 2013).

- 18 J. Carrier, L. Beaulieu, F. Therriault-Proulx, R. Roy, "Impact of interseed attenuation and tissue composition for permanent prostate implants." *Med. Phys.* **33**, 595-604 (2006).
- 19 Z. Chen, N. Yue, X. Wang, K.B. Roberts, R. Peschel, R. Nath, "Dosimetric effects of edema in permanent prostate seed implants: a rigorous solution." *Int. J. Radiat. Oncol. Biol. Phys.* **47**, 1405-1419 (2000).
- 20 O. Chibani and J.F. Williamson, "MCPI: a sub-minute Monte Carlo dose calculation engine for prostate implants." *Med. Phys.* **32**, 3688-3698 (2005).
- 21 C. Chira, G. Delouya, S. Larrivée, J. Carrier, D. Taussky, "Prostate volume changes during permanent seed brachytherapy: an analysis of intra-operative variations, predictive factors and clinical implication." *Radiat Oncol* **8** (2013).
- 22 N. Chng, I. Spadinger, W.J. Morris, N. Usmani, S. Salcudean, "Prostate brachytherapy postimplant dosimetry: automatic plan reconstruction of stranded implants." *Med. Phys.* **38**, 327-342 (2011).
- 23 N. Chng, I. Spadinger, R. Rasoda, W.J. Morris, S. Salcudean, "Prostate brachytherapy postimplant dosimetry: seed orientation and the impact of dosimetric anisotropy in stranded implants." *Med. Phys.* **39**, 721-731 (2012).
- 24 J. Corbett, J. Jezioranski, J. Crook, I. Yeung, "The effect of voxel size on the accuracy of dose-volume histograms of prostate 125I seed implants." *Med. Phys.* **29**, 1003-1006 (2002).
- 25 J. Cosset, X. Cathelineau, G. Wakil, N. Pierrat, O. Quenzer, D. Prapotnich, E. Barret, F. Rozet, M. Galiano, G. Vallancien, "Focal brachytherapy for selected low-risk prostate cancers: a pilot study." *Brachytherapy* **12**, 331-337 (2013).
- 26 J. Crook, J. Borg, A. Evans, A. Toi, E.P. Saibishkumar, S. Fung, C. Ma, "10-year experience with I-125 prostate brachytherapy at the Princess Margaret Hospital: results for 1,100 patients." *Int. J. Radiat. Oncol. Biol. Phys.* **80**, 1323-1329 (2011).

- 27 J. Crook, M. Milosevic, P. Catton, I. Yeung, T. Haycocks, T. Tran, C. Catton, M. McLean, T. Panzarella, M.A. Haider, "Interobserver variation in postimplant computed tomography contouring affects quality assessment of prostate brachytherapy." *Brachytherapy* **1**, 66-73 (2002).
- 28 J. Crook, "Commentary on "a comparison of the precision of seeds deposited as loose seeds vs. suture-embedded seeds: a randomized trial" and "prostate brachytherapy seed migration and dosimetry: analysis of stranded sources and other potential predictive factors": to strand or not to strand--is this really the question?" *Brachytherapy* **3**, 20-21 (2004).
- 29 A.V. D'Amico, R. Cormack, C.M. Tempany, S. Kumar, G. Topulos, H.M. Kooy, C.N. Coleman, "Real-time magnetic resonance image-guided interstitial brachytherapy in the treatment of select patients with clinically localized prostate cancer." *Int. J. Radiat. Oncol. Biol. Phys.* **42**, 507-515 (1998).
- 30 A.V. D'Amico, R. Whittington, S.B. Malkowicz, D. Schultz, K. Blank, G.A. Broderick, J.E. Tomaszewski, A.A. Renshaw, I. Kaplan, C.J. Beard, A. Wein, "Biochemical outcome after radical prostatectomy, external beam radiation therapy, or interstitial radiation therapy for clinically localized prostate cancer." *JAMA* **280**, 969-974 (1998).
- 31 B.J. Davis, T.M. Pisansky, T.M. Wilson, H.J. Rothenberg, A. Pacelli, D.W. Hillman, D.J. Sargent, D.G. Bostwick, "The radial distance of extraprostatic extension of prostate carcinoma: implications for prostate brachytherapy." *Cancer* **85**, 2630-2637 (1999).
- 32 B.J. Davis, E.M. Horwitz, W.R. Lee, J.M. Crook, R.G. Stock, G.S. Merrick, W.M. Butler, P.D. Grimm, N.N. Stone, L. Potters, A.L. Zietman, M.J. Zelefsky, A.B. Society, "American Brachytherapy Society consensus guidelines for transrectal ultrasound-guided permanent prostate brachytherapy." *Brachytherapy* **11**, 6-19 (2012).

- 33 J.E. Dawson, T. Wu, T. Roy, J.Y. Gu, H. Kim, "Dose effects of seeds placement deviations from pre-planned positions in ultrasound guided prostate implants." *Radiother. Oncol.* **32**, 268-270 (1994).
- 34 J.O. Deasy, A.I. Blanco, V.H. Clark, "CERR: a computational environment for radiotherapy research." *Med. Phys.* **30**, 979-985 (2003).
- 35 E. Dehghan, J. Lee, P. Fallavollita, N. Kuo, A. Deguet, Y. Le, E.C. Burdette, D.Y. Song, J.L. Prince, G. Fichtinger, "Ultrasound-fluoroscopy registration for prostate brachytherapy dosimetry." *Med. Image Anal.* **16**, 1347-1358 (2012).
- 36 L. Eapen, C. Kayser, Y. Deshaies, G. Perry, C. E, C. Morash, J.E. Cygler, D. Wilkins, S. Dahrouge, "Correlating the degree of needle trauma during prostate brachytherapy and the development of acute urinary toxicity." *Int. J. Radiat. Oncol. Biol. Phys.* **59**, 1392-1394 (2004).
- 37 W.F. Eddy, M. Fitzgerald, D.C. Noll, "Improved image registration by using Fourier interpolation." *Magn. Reson. Med.* **36**, 923-931 (1996).
- 38 S.B. Edge, D.R. Byrd, C.C. Compton, A.G. Fritz, F.L. Greene, A. Trotti, *American Joint Committee on Cancer Cancer Staging Manual*, 7th ed. (Springer, New York, 2010).
- 39 S.E. Eggener, P.T. Scardino, P.R. Carroll, M.J. Zelefsky, O. Sartor, H. Hricak, T.M. Wheeler, S.W. Fine, J. Trachtenberg, M.A. Rubin, M. Ohori, K. Kuroiwa, M. Rossignol, L. Abenhaim, on Prostate Cancer, International Task Force, the Focal Lesion Paradigm, "Focal therapy for localized prostate cancer: a critical appraisal of rationale and modalities." *J. Urol.* **178**, 2260-2267 (2007).
- 40 M. Eliasziw, S.L. Young, M.G. Woodbury, K. Fryday-Field, "Statistical methodology for the concurrent assessment of interrater and intrarater reliability: using goniometric measurements as an example." *Phys. Ther.* **74**, 777-788 (1994).

- 41 D.R. Evans, T. Meyer, S. Angyalfi, S. Husain, I. Kay, P. Dunscombe, "Enhanced efficiency and ergonomics of an intraoperative automated prostate brachytherapy delivery technique." *Brachytherapy* **6**, 254-257 (2007).
- 42 T.L. Faber and E.M. Stokely, "Orientation of 3-D structures in medical images," *IEEE Trans. Pattern Anal. Mach. Intell.* **10**, 626-633 (1988).
- 43 P. Fallavollita, Z.K. Aghaloo, E.C. Burdette, D.Y. Song, P. Abolmaesumi, G. Fichtinger, "Registration between ultrasound and fluoroscopy or CT in prostate brachytherapy." *Med. Phys.* **37**, 2749-2760 (2010).
- 44 Z. Gao, D. Wilkins, L. Eapen, C. Morash, Y. Wassef, L. Gerig, "A study of prostate delineation referenced against a gold standard created from the visible human data." *Radiother. Oncol.* **85**, 239-246 (2007).
- 45 M.P.R. Van Gellekom, M.A. Moerland, J.J. Battermann, J.J.W. Lagendijk, "MRI-guided prostate brachytherapy with single needle method--a planning study." *Radiother. Oncol.* **71**, 327-332 (2004).
- 46 K.A. Gifford, J.L. Horton, T.A. Wareing, G. Failla, F. Mourtada, "Comparison of a finite-element multigroup discrete-ordinates code with Monte Carlo for radiotherapy calculations." *Phys. Med. Biol.* **51**, 2253-2265 (2006).
- 47 K.A. Gifford, M.J. Price, J.L. Horton, T.A. Wareing, F. Mourtada, "Optimization of deterministic transport parameters for the calculation of the dose distribution around a high dose-rate ^{192}Ir brachytherapy source." *Med. Phys.* **35**, 2279-2285 (2008).
- 48 P. Grimm, I. Billiet, D. Bostwick, A.P. Dicker, S. Frank, J. Immerzeel, M. Keyes, P. Kupelian, W.R. Lee, S. Machtens, J. Mayadev, B.J. Moran, G. Merrick, J. Millar, M. Roach, R. Stock, K. Shinohara, M. Scholz, E. Weber, A. Zietman, M. Zelefsky, J. Wong, S. Wentworth, R. Vera, S. Langley, "Comparative analysis of prostate-specific antigen free survival outcomes for patients with low, intermediate and high risk

- prostate cancer treatment by radical therapy. Results from the Prostate Cancer Results Study Group." *BJU Int.* **109 Suppl 1**, 22-29 (2012).
- 49 B.H. Han, K. Wallner, G. Merrick, W. Butler, S. Sutlief, J. Sylvester, "Prostate brachytherapy seed identification on post-implant TRUS images." *Med. Phys.* **30**, 898-900 (2003).
- 50 H. Ishiyama, M. Kitano, T. Satoh, Y. Niibe, M. Uemae, T. Fujita, S. Baba, K. Hayakawa, "Difference in rectal dosimetry between pre-plan and post-implant analysis in transperineal interstitial brachytherapy for prostate cancer." *Radiother. Oncol.* **78**, 194-198 (2006).
- 51 C.W. Jeong, H.K. Park, S.K. Hong, S. Byun, H.J. Lee, S.E. Lee, "Comparison of prostate volume measured by transrectal ultrasonography and MRI with the actual prostate volume measured after radical prostatectomy." *Urol. Int.* **81**, 179-185 (2008).
- 52 I. Kawrakow, "Accurate condensed history Monte Carlo simulation of electron transport. I. EGSnrc, the new EGS4 version." *Med. Phys.* **27**, 485-498 (2000).
- 53 T. Kemmerer, M. Lahanas, D. Baltas, N. Zamboglou, "Dose-volume histograms computation comparisons using conventional methods and optimized fast Fourier transforms algorithms for brachytherapy." *Med. Phys.* **27**, 2343-2356 (2000).
- 54 M. Keyes, J. Crook, W.J. Morris, G. Morton, T. Pickles, N. Usmani, E. Vigneault, "Canadian prostate brachytherapy in 2012." *Can Urol Assoc J* **7**, 51-58 (2013).
- 55 C. Kirisits, F. Siebert, D. Baltas, M.D. Brabandere, T.P. Hellebust, D. Berger, J. Venselaar, "Accuracy of volume and DVH parameters determined with different brachytherapy treatment planning systems." *Radiother. Oncol.* **84**, 290-297 (2007).
- 56 A.P.S. Kirkham, M. Emberton, C. Allen, "How good is MRI at detecting and characterising cancer within the prostate?" *Eur. Urol.* **50**, 1163-74 (2006).

- 57 P.A. Kupelian, J.C. Buchsbaum, M.A. Elshaikh, C.A. Reddy, E.A. Klein, "Improvement in relapse-free survival throughout the PSA era in patients with localized prostate cancer treated with definitive radiotherapy: year of treatment an independent predictor of outcome." *Int. J. Radiat. Oncol. Biol. Phys.* **57**, 629-634 (2003).
- 58 T.I. Laakso, V. Valimaki, M. Karjalainen, U.K. Laine, "Splitting the unit delay," *IEEE Signal Process. Mag.* **13**, 30-60 (1996).
- 59 G. Leclerc, M. Lavallée, R. Roy, E. Vigneault, L. Beaulieu, "Prostatic edema in 125I permanent prostate implants: dynamical dosimetry taking volume changes into account." *Med. Phys.* **33**, 574-583 (2006).
- 60 H.K. Lee, W.D. D'Souza, J.J. Yamal, A. Pollack, A.K. Lee, M.B. Palmer, D.A. Kuban, "Dosimetric consequences of using a surrogate urethra to estimate urethral dose after brachytherapy for prostate cancer." *Int. J. Radiat. Oncol. Biol. Phys.* **57**, 355-361 (2003).
- 61 W.R. Lee, M. Roach, J. Michalski, B. Moran, D. Beyer, "Interobserver variability leads to significant differences in quantifiers of prostate implant adequacy." *Int. J. Radiat. Oncol. Biol. Phys.* **54**, 457-461 (2002).
- 62 P. Lindsay, J. Battista, J.V. Dyk, "The effect of seed anisotropy on brachytherapy dose distributions using 125I and 103Pd." *Med. Phys.* **28**, 336-345 (2001).
- 63 P.E. Lindsay, J.V. Dyk, J.J. Battista, "A systematic study of imaging uncertainties and their impact on 125I prostate brachytherapy dose evaluation." *Med. Phys.* **30**, 1897-1908 (2003).
- 64 P.J. Littrup, C.R. Williams, T.K. Egglin, R.A. Kane, "Determination of prostate volume with transrectal US for cancer screening. Part II. Accuracy of in vitro and in vivo techniques." *Radiology* **179**, 49-53 (1991).

- 65 D. Liu and R.S. Sloboda, "Fast dose kernel interpolation using Fourier transform with application to permanent prostate brachytherapy dosimetry." *Med. Phys.* **41** (2014).
- 66 D. Liu, N. Usmani, S. Ghosh, W. Kamal, J. Pedersen, N. Pervez, D. Yee, B. Danielson, A. Murtha, J. Amanie, R.S. Sloboda, "Comparison of prostate volume, shape, and contouring variability determined from preimplant magnetic resonance and transrectal ultrasound images." *Brachytherapy* **11**, 284-291 (2012).
- 67 D. Liu, N. Usmani, R.S. Sloboda, "Transrectal ultrasound based prostate volume determination: is the frustum algorithm more accurate than planimetry?" *Med. Phys.* **40** (2013).
- 68 H. Liu, G. Cheng, Y. Yu, R. Brasacchio, D. Rubens, J. Strang, L. Liao, E. Messing, "Automatic localization of implanted seeds from post-implant CT images." *Phys. Med. Biol.* **48**, 1191-1203 (2003).
- 69 P.J. MacMahon, A. Kennedy, D.T. Murphy, M. Maher, M.M. McNicholas, "Modified prostate volume algorithm improves transrectal US volume estimation in men presenting for prostate brachytherapy." *Radiology* **250**, 273-280 (2009).
- 70 P.W. McLaughlin, V. Narayana, D.G. Drake, B.M. Miller, L. Marsh, J. Chan, R. Gonda, R.J. Winfield, P.L. Roberson, "Comparison of MRI pulse sequences in defining prostate volume after permanent implantation." *Int. J. Radiat. Oncol. Biol. Phys.* **54**, 703-711 (2002).
- 71 P.W. McLaughlin, C. Evans, M. Feng, V. Narayana, "Radiographic and anatomic basis for prostate contouring errors and methods to improve prostate contouring accuracy." *Int. J. Radiat. Oncol. Biol. Phys.* **76**, 369-378 (2010).
- 72 P. McLaughlin, V. Narayana, C. Pan, S. Berri, S. Troyer, J. Herman, V. Evans, P. Roberson, "Comparison of day 0 and day 14 dosimetry for permanent prostate implants using stranded seeds." *Int. J. Radiat. Oncol. Biol. Phys.* **64**, 144-150 (2006).

- 73 G.S. Merrick, W.M. Butler, A.T. Dorsey, J.H. Lief, M.L. Benson, "Seed fixity in the prostate/periprostatic region following brachytherapy." *Int. J. Radiat. Oncol. Biol. Phys.* **46**, 215-220 (2000).
- 74 G.S. Merrick, W.M. Butler, K.E. Wallner, J.C. Blasko, J. Michalski, J. Aronowitz, P. Grimm, B.J. Moran, P.W. McLaughlin, J. Usher, J.H. Lief, Z.A. Allen, "Variability of prostate brachytherapy pre-implant dosimetry: a multi-institutional analysis." *Brachytherapy* **4**, 241-251 (2005).
- 75 E.M. Messing, J.B. Zhang, D.J. Rubens, R.A. Brasacchio, J.G. Strang, A. Soni, M.C. Schell, P.G. Okunieff, Y. Yu, "Intraoperative optimized inverse planning for prostate brachytherapy: early experience." *Int. J. Radiat. Oncol. Biol. Phys.* **44**, 801-808 (1999).
- 76 T. Meyer and I. Kay, "Forward projection of variable angle imaging geometry to reduce reconstruction uncertainty and simplify seed matching in a backprojection algorithm." *Phys. Med. Biol.* **54**, 4595-4604 (2009).
- 77 T. Meyer, *Dosimetric Impact of Implant Uncertainties in Prostate Brachytherapy* (Doctoral thesis, University of Calgary, 2010).
- 78 M.A. Moerland, H.K. Wijrdeman, R. Beersma, C.J. Bakker, J.J. Battermann, "Evaluation of permanent I-125 prostate implants using radiography and magnetic resonance imaging." *Int. J. Radiat. Oncol. Biol. Phys.* **37**, 927-933 (1997).
- 79 T.T. Monajemi, C.M. Clements, R.S. Sloboda, "Dose calculation for permanent prostate implants incorporating spatially anisotropic linearly time-resolving edema." *Med. Phys.* **38**, 2289-2298 (2011).
- 80 M. Moradi, S.S. Mahdavi, E. Dehghan, J.R. Lobo, S. Deshmukh, W.J. Morris, G. Fichtinger, S.T.E. Salcudean, "Seed localization in ultrasound and registration to C-arm fluoroscopy using matched needle tracks for prostate brachytherapy." *IEEE Trans. Biomed. Eng.* **59**, 2558-2567 (2012).

- 81 W.J. Morris, M. Keyes, I. Spadinger, W. Kwan, M. Liu, M. McKenzie, H. Pai, T. Pickles, S. Tyldesley, "Population-based 10-year oncologic outcomes after low-dose-rate brachytherapy for low-risk and intermediate-risk prostate cancer." *Cancer* **119**, 1537-1546 (2013).
- 82 S.R. Mousavi, A. Sadeghi-Naini, G.J. Czarnota, A. Samani, "Towards clinical prostate ultrasound elastography using full inversion approach." *Med. Phys.* **41** (2014).
- 83 B.G. Muller, W. van den Bos, P.A. Pinto, J.J. de la Rosette, "Imaging modalities in focal therapy: patient selection, treatment guidance, and follow-up." *Curr. Opin. Urol.* **24**, 218-224 (2014).
- 84 S. Nag, D. Beyer, J. Friedland, P. Grimm, R. Nath, "American Brachytherapy Society (ABS) recommendations for transperineal permanent brachytherapy of prostate cancer." *Int. J. Radiat. Oncol. Biol. Phys.* **44**, 789-799 (1999).
- 85 S. Nag, J.P. Ciezki, R. Cormack, S. Doggett, K. DeWynngaert, G.K. Edmundson, R.G. Stock, N.N. Stone, Y. Yu, M.J. Zelefsky, Clinical Research Committee, American Brachytherapy Society, "Intraoperative planning and evaluation of permanent prostate brachytherapy: report of the American Brachytherapy Society." *Int. J. Radiat. Oncol. Biol. Phys.* **51**, 1422-1430 (2001).
- 86 V. Narayana, P.L. Roberson, R.J. Winfield, P.W. McLaughlin, "Impact of ultrasound and computed tomography prostate volume registration on evaluation of permanent prostate implants." *Int. J. Radiat. Oncol. Biol. Phys.* **39**, 341-346 (1997).
- 87 R. Nath, L.L. Anderson, G. Luxton, K.A. Weaver, J.F. Williamson, A.S. Meigooni, "Dosimetry of interstitial brachytherapy sources: recommendations of the AAPM Radiation Therapy Committee Task Group No. 43. American Association of Physicists in Medicine." *Med. Phys.* **22**, 209-234 (1995).
- 88 R. Nath, L.L. Anderson, J.A. Meli, A.J. Olch, J.A. Stitt, J.F. Williamson, "Code of practice for brachytherapy physics: report of the AAPM Radiation Therapy Committee

- Task Group No. 56. American Association of Physicists in Medicine." *Med. Phys.* **24**, 1557-1598 (1997).
- 89 R. Nath, W.S. Bice, W.M. Butler, Z. Chen, A.S. Meigooni, V. Narayana, M.J. Rivard, Y. Yu, American Association of Physicists in Medicine, "AAPM recommendations on dose prescription and reporting methods for permanent interstitial brachytherapy for prostate cancer: report of Task Group 137." *Med. Phys.* **36**, 5310-5322 (2009).
- 90 S. Nath, Z. Chen, N. Yue, S. Trumpore, R. Peschel, "Dosimetric effects of needle divergence in prostate seed implant using 125I and 103Pd radioactive seeds." *Med. Phys.* **27**, 1058-1066 (2000).
- 91 M.S. Nathan, K. Seenivasagam, Q. Mei, J.E. Wickham, R.A. Miller, "Transrectal ultrasonography: why are estimates of prostate volume and dimension so inaccurate?" *Br. J. Urol.* **77**, 401-407 (1996).
- 92 S. Oguro, J. Tokuda, H. Elhawary, S. Haker, R. Kikinis, C.M.C. Tempany, N. Hata, "MRI signal intensity based B-spline nonrigid registration for pre- and intraoperative imaging during prostate brachytherapy." *J. Magn. Reson. Imaging* **30**, 1052-1058 (2009).
- 93 J.T. Olkkonen and H. Olkkonen, "Fractional Time-Shift B-Spline Filter," *IEEE Signal Process. Lett.* **14**, 688-691 (2007).
- 94 J.T. Olkkonen and H. Olkkonen, "Fractional Delay Filter Based on the B-Spline Transform," *IEEE Signal Process. Lett.* **14**, 97-100 (2007).
- 95 E.B. Podgorsak, *Radiation Oncology Physics: A Handbook for Teachers and Students*, 1st ed. (International Atomic Energy Agency, Vienna, 2005).
- 96 T.J. Polascik and V. Mouraviev, "Focal therapy for prostate cancer." *Curr. Opin. Urol.* **18**, 269-274 (2008).

- 97 A. Polo, F. Cattani, A. Vavassori, D. Origgi, G. Villa, H. Marsiglia, M. Bellomi, G. Tosi, O.D. Cobelli, R. Orecchia, "MR and CT image fusion for postimplant analysis in permanent prostate seed implants." *Int. J. Radiat. Oncol. Biol. Phys.* **60**, 1572-1579 (2004).
- 98 A.D. Polyanin and A.I. Chernoutsan, *A Concise Handbook of Mathematics, Physics, and Engineering Sciences* (Chapman & Hall/CRC, Boca Raton, Fl., 2011).
- 99 E. Poon, Y. Le, J.F. Williamson, F. Verhaegen, "BrachyGUI: an adjunct to an accelerated Monte Carlo photon transport code for patient-specific brachytherapy dose calculations and analysis," *J Phys: Conf Ser* **102** (2008).
- 100 L. Potters, Y. Cao, E. Calugaru, T. Torre, P. Fearn, X.H. Wang, "A comprehensive review of CT-based dosimetry parameters and biochemical control in patients treated with permanent prostate brachytherapy." *Int. J. Radiat. Oncol. Biol. Phys.* **50**, 605-614 (2001).
- 101 L. Potters, "Permanent prostate brachytherapy in men with clinically localised prostate cancer." *Clin. Oncol.* **15**, 301-315 (2003).
- 102 J. Pouliot, D. Tremblay, J. Roy, S. Filice, "Optimization of permanent 125I prostate implants using fast simulated annealing." *Int. J. Radiat. Oncol. Biol. Phys.* **36**, 711-720 (1996).
- 103 J.J. Prete, B.R. Prestidge, W.S. Bice, D.F. Dubois, L.A. Hotchkiss, "Comparison of MRI- and CT-based post-implant dosimetric analysis of transperineal interstitial permanent prostate brachytherapy." *Radiat. Oncol. Investig.* **6**, 90-96 (1998).
- 104 A. Rahmouni, A. Yang, C.M. Tempany, T. Frenkel, J. Epstein, P. Walsh, P.K. Leichner, C. Ricci, E. Zerhouni, "Accuracy of in-vivo assessment of prostatic volume by MRI and transrectal ultrasonography." *J. Comput. Assist. Tomogr.* **16**, 935-940 (1992).

- 105 C. Rasch, I. Barillot, P. Remeijer, A. Touw, M. van Herk, J.V. Lebesque, "Definition of the prostate in CT and MRI: a multi-observer study." *Int. J. Radiat. Oncol. Biol. Phys.* **43**, 57-66 (1999).
- 106 M.J. Rivard, B.M. Coursey, L.A. DeWerd, W.F. Hanson, M.S. Huq, G.S. Ibbott, M.G. Mitch, R. Nath, J.F. Williamson, "Update of AAPM Task Group No. 43 Report: A revised AAPM protocol for brachytherapy dose calculations." *Med. Phys.* **31**, 633-674 (2004).
- 107 M.J. Rivard, J.L.M. Venselaar, L. Beaulieu, "The evolution of brachytherapy treatment planning." *Med. Phys.* **36**, 2136-2153 (2009).
- 108 M. Roach, G. Hanks, H. Thames, P. Schellhammer, W.U. Shipley, G.H. Sokol, H. Sandler, "Defining biochemical failure following radiotherapy with or without hormonal therapy in men with clinically localized prostate cancer: recommendations of the RTOG-ASTRO Phoenix Consensus Conference." *Int. J. Radiat. Oncol. Biol. Phys.* **65**, 965-974 (2006).
- 109 P.L. Roberson, V. Narayana, D.L. McShan, R.J. Winfield, P.W. McLaughlin, "Source placement error for permanent implant of the prostate." *Med. Phys.* **24**, 251-257 (1997).
- 110 A.K.H. Robertson, P.S. Basran, S.D. Thomas, D. Wells, "CT, MR, and ultrasound image artifacts from prostate brachytherapy seed implants: the impact of seed size." *Med. Phys.* **39**, 2061-2068 (2012).
- 111 C. Salembier, P. Lavagnini, P. Nickers, P. Mangili, A. Rijnders, A. Polo, J. Venselaar, P. Hoskin, G.E.C.E.P. Group, "Tumour and target volumes in permanent prostate brachytherapy: a supplement to the ESTRO/EAU/EORTC recommendations on prostate brachytherapy." *Radiother. Oncol.* **83**, 3-10 (2007).

- 112 R.S. Sloboda, J.E. Pedersen, J. Hanson, R.M. Halperin, "Dosimetric consequences of increased seed strength for I-125 prostate implants." *Radiother. Oncol.* **68**, 295-297 (2003).
- 113 R.S. Sloboda, N. Usmani, J. Pedersen, A. Murtha, N. Pervez, D. Yee, "Time course of prostatic edema post permanent seed implant determined by magnetic resonance imaging." *Brachytherapy* **9**, 354-361 (2010).
- 114 S. Smith, K. Wallner, G. Merrick, W. Butler, S. Sutlief, P. Grimm, "Interpretation of pre- versus postimplant TRUS images." *Med. Phys.* **30**, 920-924 (2003).
- 115 W.L. Smith, C. Lewis, G. Bauman, G. Rodrigues, D. D'Souza, R. Ash, D. Ho, V. Venkatesan, D. Downey, A. Fenster, "Prostate volume contouring: a 3D analysis of segmentation using 3DTRUS, CT, and MR." *Int. J. Radiat. Oncol. Biol. Phys.* **67**, 1238-1247 (2007).
- 116 M.C. Solhjem, B.J. Davis, T.M. Pisansky, T.M. Wilson, L.A. Mynderse, M.G. Herman, B.F. King, S.M. Geyer, "Prostate volume measurement by transrectal ultrasound and computed tomography before and after permanent prostate brachytherapy." *Int. J. Radiat. Oncol. Biol. Phys.* **60**, 767-776 (2004).
- 117 D.M. Somford, J.J. Fütterer, T. Hambrock, J.O. Barentsz, "Diffusion and perfusion MR imaging of the prostate." *Magn. Reson. Imaging Clin. N. Am.* **16**, 685-95 (2008).
- 118 I. Spadinger, W.J. Morris, M. Keyes, M. Liu, R. Shaffer, A. Thompson, N. Chng, R. Woods, "Quadrant dosimetry as a predictor of biochemical relapse in 125I prostate brachytherapy." *Brachytherapy* **10**, 87-97 (2011).
- 119 T.A. Stamey, J.N. Kabalin, J.E. McNeal, I.M. Johnstone, F. Freiha, E.A. Redwine, N. Yang, "Prostate specific antigen in the diagnosis and treatment of adenocarcinoma of the prostate. II. Radical prostatectomy treated patients." *J. Urol.* **141**, 1076-1083 (1989).

- 120 T.A. Stamey, J.N. Kabalin, M. Ferrari, "Prostate specific antigen in the diagnosis and treatment of adenocarcinoma of the prostate. III. Radiation treated patients." *J. Urol.* **141**, 1084-1087 (1989).
- 121 T.A. Stamey, N. Yang, A.R. Hay, J.E. McNeal, F.S. Freiha, E. Redwine, "Prostate-specific antigen as a serum marker for adenocarcinoma of the prostate." *N. Engl. J. Med.* **317**, 909-916 (1987).
- 122 T.A. Stamey, M. Caldwell, J.E. McNeal, R. Nolley, M. Hemenez, J. Downs, "The prostate specific antigen era in the United States is over for prostate cancer: what happened in the last 20 years?" *J. Urol.* **172**, 1297-1301 (2004).
- 123 S. Standring, N.R. Borley, P. Collins, A.R. Crossman, M.A. Gatzoulis, J.C. Healy, D. Johnson, V. Mahadevan, R.L. Newell, C.B. Wigley, *Gray's Anatomy*, 40th ed. (Churchill Livingstone/Elsevier, Edinburgh, 2008).
- 124 R.G. Stock, N.N. Stone, A. Tabert, C. Iannuzzi, J.K. DeWyngaert, "A dose-response study for I-125 prostate implants." *Int. J. Radiat. Oncol. Biol. Phys.* **41**, 101-108 (1998).
- 125 S.H. Stokes, J.D. Real, P.W. Adams, J.C. Clements, S. Wuertzer, W. Kan, "Transperineal ultrasound-guided radioactive seed implantation for organ-confined carcinoma of the prostate." *Int. J. Radiat. Oncol. Biol. Phys.* **37**, 337-341 (1997).
- 126 N.N. Stone and R.G. Stock, "Reduction of pulmonary migration of permanent interstitial sources in patients undergoing prostate brachytherapy." *Urology* **66**, 119-123 (2005).
- 127 Y. Su, B.J. Davis, K.M. Furutani, M.G. Herman, R.A. Robb, "Seed localization and TRUS-fluoroscopy fusion for intraoperative prostate brachytherapy dosimetry." *Comput. Aided Surg.* **12**, 25-34 (2007).
- 128 A. Sugawara, J. Nakashima, E. Kunieda, H. Nagata, R. Mizuno, S. Seki, Y. Shiraishi, R. Kouta, M. Oya, N. Shigematsu, "Incidence of seed migration to the chest, abdomen,

- and pelvis after transperineal interstitial prostate brachytherapy with loose (125)I seeds." *Radiat Oncol* **6** (2011).
- 129 O. Tanaka, S. Hayashi, M. Matsuo, M. Nakano, Y. Kubota, S. Maeda, K. Ohtakara, T. Deguchi, H. Hoshi, "MRI-based preplanning in low-dose-rate prostate brachytherapy." *Radiother. Oncol.* **88**, 115-120 (2008).
- 130 O. Tanaka, S. Hayashi, M. Matsuo, K. Sakurai, M. Nakano, S. Maeda, K. Kajita, T. Deguchi, H. Hoshi, "Comparison of MRI-based and CT/MRI fusion-based postimplant dosimetric analysis of prostate brachytherapy." *Int. J. Radiat. Oncol. Biol. Phys.* **66**, 597-602 (2006).
- 131 E.M. Tapen, J.C. Blasko, P.D. Grimm, H. Ragde, R. Luse, S. Clifford, J. Sylvester, T.W. Griffin, "Reduction of radioactive seed embolization to the lung following prostate brachytherapy." *Int. J. Radiat. Oncol. Biol. Phys.* **42**, 1063-1067 (1998).
- 132 R. Taschereau, J. Pouliot, J. Roy, D. Tremblay, "Seed misplacement and stabilizing needles in transperineal permanent prostate implants." *Radiother. Oncol.* **55**, 59-63 (2000).
- 133 D. Taussky, L. Austen, A. Toi, I. Yeung, T. Williams, S. Pearson, M. McLean, G. Pond, J. Crook, "Sequential evaluation of prostate edema after permanent seed prostate brachytherapy using CT-MRI fusion." *Int. J. Radiat. Oncol. Biol. Phys.* **62**, 974-980 (2005).
- 134 D. Taussky, C. Mouldjian, R. Larouche, D. Béliveau-Nadeau, C. Boudreau, Y. Hervieux, D. Donath, "Seed migration in prostate brachytherapy depends on experience and technique." *Brachytherapy* **11**, 452-456 (2012).
- 135 R.E.P. Taylor and D.W.O. Rogers, "An EGSnrc Monte Carlo-calculated database of TG-43 parameters." *Med. Phys.* **35**, 4228-4241 (2008).

- 136 R.E.P. Taylor, G. Yegin, D.W.O. Rogers, "Benchmarking brachydose: Voxel based EGSnrc Monte Carlo calculations of TG-43 dosimetry parameters." *Med. Phys.* **34**, 445-457 (2007).
- 137 A. Tewari, *Prostate Cancer: A Comprehensive Perspective*, 1st ed. (Springer, London, 2013).
- 138 B. Thomadsen, M. Rivard, W. Butler, *Brachytherapy Physics*, 2nd ed. (Medical Physics Publishing, Madison, WI, 2005).
- 139 S. Tong, H.N. Cardinal, R.F. McLoughlin, D.B. Downey, A. Fenster, "Intra- and inter-observer variability and reliability of prostate volume measurement via two-dimensional and three-dimensional ultrasound imaging." *Ultrasound Med. Biol.* **24**, 673-681 (1998).
- 140 D. Tubic and L. Beaulieu, "Sliding slice: a novel approach for high accuracy and automatic 3D localization of seeds from CT scans." *Med. Phys.* **32**, 163-174 (2005).
- 141 I.B. Tutar, L. Gong, S. Narayanan, S.D. Pathak, P.S. Cho, K. Wallner, Y. Kim, "Seed-based transrectal ultrasound-fluoroscopy registration method for intraoperative dosimetry analysis of prostate brachytherapy." *Med. Phys.* **35**, 840-848 (2008).
- 142 M. Unser, P. Thevenaz, L. Yaroslavsky, "Convolution-based interpolation for fast, high-quality rotation of images," *IEEE Trans. Image Process.* **4**, 1371-1381 (1995).
- 143 N. Usmani, N. Chng, I. Spadinger, W.J. Morris, "Lack of significant intraprostatic migration of stranded iodine-125 sources in prostate brachytherapy implants." *Brachytherapy* **10**, 275-285 (2011).
- 144 N. Usmani, K. Martell, S. Ghosh, H. Moore, N. Pervez, J. Pedersen, D. Yee, A. Murtha, J. Amanie, R. Sloboda, "Comparison of low and intermediate source strengths for (125)I prostate brachytherapy implants." *Brachytherapy* **12**, 442-448 (2013).

- 145 N. Usmani, R. Sloboda, W. Kamal, S. Ghosh, N. Pervez, J. Pedersen, D. Yee, B. Danielson, A. Murtha, J. Amanie, T. Monajemi, "Can images obtained with high field strength magnetic resonance imaging reduce contouring variability of the prostate?" *Int. J. Radiat. Oncol. Biol. Phys.* **80**, 728-734 (2011).
- 146 K. Wachowicz, S.D. Thomas, B.G. Fallone, "Characterization of the susceptibility artifact around a prostate brachytherapy seed in MRI." *Med. Phys.* **33**, 4459-4467 (2006).
- 147 G. Wan, Z. Wei, L. Gardi, D.B. Downey, A. Fenster, "Brachytherapy needle deflection evaluation and correction." *Med. Phys.* **32**, 902-909 (2005).
- 148 F.M. Waterman, N. Yue, B.W. Corn, A.P. Dicker, "Edema associated with I-125 or Pd-103 prostate brachytherapy and its impact on post-implant dosimetry: an analysis based on serial CT acquisition." *Int. J. Radiat. Oncol. Biol. Phys.* **41**, 1069-1077 (1998).
- 149 D.A. Wilkinson, E.J. Lee, J.P. Ciezki, D.S. Mohan, C. Zippe, K. Angermeier, J. Ulchaker, E.A. Klein, D. Mohan, "Dosimetric comparison of pre-planned and OR-planned prostate seed brachytherapy." *Int. J. Radiat. Oncol. Biol. Phys.* **48**, 1241-1244 (2000).
- 150 J. Xue, F. Waterman, J. Handler, E. Gressen, "The effect of interobserver variability on transrectal ultrasonography-based postimplant dosimetry." *Brachytherapy* **5**, 174-182 (2006).
- 151 C. Yang, S. Wang, A.T. Lin, C. Lin, "Factors affecting prostate volume estimation in computed tomography images." *Med. Dosim.* **36**, 85-90 (2011).
- 152 Y. Yu, L.L. Anderson, Z. Li, D.E. Mellenberg, R. Nath, M.C. Schell, F.M. Waterman, A. Wu, J.C. Blasko, "Permanent prostate seed implant brachytherapy: report of the American Association of Physicists in Medicine Task Group No. 64." *Med. Phys.* **26**, 2054-2076 (1999).

- 153 N. Yue, Z. Chen, R. Peschel, A.P. Dicker, F.M. Waterman, R. Nath, "Optimum timing for image-based dose evaluation of 125I and 103PD prostate seed implants." *Int. J. Radiat. Oncol. Biol. Phys.* **45**, 1063-1072 (1999).
- 154 M.J. Zelefsky, T. Hollister, A. Raben, S. Matthews, K.E. Wallner, "Five-year biochemical outcome and toxicity with transperineal CT-planned permanent I-125 prostate implantation for patients with localized prostate cancer." *Int. J. Radiat. Oncol. Biol. Phys.* **47**, 1261-1266 (2000).
- 155 M.J. Zelefsky and W.F. Whitmore, "Long-term results of retropubic permanent 125iodine implantation of the prostate for clinically localized prostatic cancer." *J. Urol.* **158** (1997).
- 156 M.J. Zelefsky, Y. Yamada, G.N. Cohen, A. Shippy, H. Chan, D. Fridman, M. Zaider, "Five-year outcome of intraoperative conformal permanent I-125 interstitial implantation for patients with clinically localized prostate cancer." *Int. J. Radiat. Oncol. Biol. Phys.* **67**, 65-70 (2007).
- 157 M.J. Zelefsky and M. Zaider, "Low-dose-rate brachytherapy for prostate cancer: preplanning vs. intraoperative planning-intraoperative planning is best." *Brachytherapy* **5**, 143-4; discussion 146 (2006).